FLOW IN RADIALLY ACQUIRED MAGNETIC RESONANCE IMAGING: METHODS AND APPLICATIONS IN ATHEROSCLEROTIC DISEASE

By

Andrew L. Wentland

A DISSERTATION SUBMITTED IN PARTIAL FULFILLMENT

OF THE REQUIREMENTS FOR THE DEGREE OF

Doctor of Philosophy

(Medical Physics)

at the

UNIVERSITY OF WISCONSIN – MADISON

2013

Date of final oral examination: November 15, 2012

The dissertation is approved by the following members of the Final Oral Committee:

Oliver Wieben, Associate Professor, Medical Physics
Thomas M. Grist, Professor, Radiology
Deane F. Mosher, Professor, Biomolecular Chemistry
Frank R. Korosec, Professor, Radiology
Tomy Varghese, Professor, Medical Physics
Charles A. Mistretta, Professor, Medical Physics

Abstract

Flow in Radially Acquired Magnetic Resonance Imaging: Methods and Applications in Atherosclerotic Disease

Andrew L. Wentland

Under the supervision of Drs. Oliver Wieben and Thomas Grist

at the University of Wisconsin – Madison

Atherosclerosis is a recognized cause of cardiovascular disease (CVD) and stroke. Typically, a substantial degree of atherosclerotic disease burden is needed for a patient to be symptomatic. Therefore, the prevention and early detection of atherosclerosis are vital means of decreasing the incidence of cardiovascular events and to decreasing the costs associated with CVD.

A number of flow-related atherosclerotic biomarkers have been derived from phase contrast magnetic resonance imaging (PC MRI) techniques. Pulse wave velocity (PWV) is one such biomarker related to vascular stiffening. As arteries are stiffened by the growth of atherosclerotic plaques, the systolic wave of blood down the aorta is accelerated because of the loss of elastic recoil in the vessel, leading to an elevated PWV. Wall shear stress (WSS) is another biomarker linked to atherosclerosis that represents the drag forces on vessel walls. It is hypothesized that abnormal blood flow patterns, and in turn insufficient stress, lead to dysfunction of the endothelium. Endothelial dysfunction leads to vascular remodeling, such as adaptive intimal thickening, and may progress to advanced atherosclerotic lesions. However,

measurements of PWV require high temporal resolution and measurements of WSS require high spatial resolution. Such resolution requirements are challenging to achieve with PC MRI due to the lengthy scan times needed for velocity and reference encoding. In clinical practice, scan times are often reduced for PC MR imaging through the sacrifice of spatial and/or temporal resolution, which would compromise the utility and accuracy of PWV and WSS measurements.

The work in this dissertation aims to accelerate phase contrast imaging for the sake of acquiring and measuring PWV and WSS. Two-dimensional PC MRI with radial undersampling is investigated to determine the degree of undersampling that permits accurate flow measurements. Experiments in both flow phantoms and healthy volunteers demonstrate that accurate flow measurements can be obtained even with high undersampling factors. To measure WSS and PWV, a four-dimensional PC imaging technique with radial undersampling was employed. The repeatability and internal consistency of flow measurements from the four-dimensional PC imaging technique were evaluated in the abdominal vasculature. A PWV tool was developed and a WSS tool was utilized to handle the unique 4D data sets, which provide velocity vector fields throughout the cardiac cycle with volumetric coverage. PWV and WSS were evaluated in a swine model of atherosclerosis. A McKinnon-Bates sparsification algorithm was developed and implemented to further accelerate the acquisition of PC data. It is demonstrated that this algorithm reduces artifacts in PC images and allows for greater undersampling factors.

Acknowledgements

My journey into magnetic resonance imaging began on February 12, 2003. I was an undergraduate sophomore in biomedical engineering with the intention of entering industry upon graduation with my bachelor's degree. A single evening completely changed those plans. That fateful February evening I attended a talk by Beth Meyerand, PhD given to the biomedical Engineering Society. I was immediately captivated by the field of MRI. Within a matter of days I met with Robert Radwin, PhD, the then-chairman of the UW Department of Biomedical Engineering. He happened to know a professor in the UW Department of Radiology who was looking for an undergraduate to hire. His name was Thomas Grist, MD, the then-chief of cardiovascular imaging. Dr. Grist hired me despite my complete naiveté of anything related to medical imaging.

That summer, on May 27, 2003, I began working for Dr. Grist. Dr. Grist put me on a starter project under Sean Fain, PhD. While this initial project was unrelated to MRI and was for the purpose of measuring emphysema index from CT images, it was a great introduction to image processing. I am indebted to Dr. Fain, for upon completion of this project, he recommended to Dr. Grist that I be given my own project. Dr. Grist immediately assigned me a project detailed in one of the specific aims of his R01 renal grant. Over the subsequent three years of my undergraduate career I worked on this project. In addition to Dr. Grist, I am grateful to many people during my three years of undergraduate research. For this period of my research career, I would like especially to thank Frank Korosec, PhD. Dr. Korosec spent a great deal of time explaining MR concepts to me, in addition to helping me troubleshoot my phantom

experiments. I also credit Dr. Korosec with introducing and teaching me about scientific writing. Dr. Korosec worked tirelessly with me on my first abstract and manuscript submissions—going through each document line by line to clarify the manner in which scientific information should be written. I'd also like to thank Karl Vigen, PhD and Oliver Wieben, PhD, who also aided in my undergraduate experiments. Additionally during my undergraduate career I worked with Victor Haughton, MD to explore the use of 2D phase contrast imaging for measuring cerebrospinal fluid flow. I'm very grateful to Dr. Haughton for showing me how to have such enthusiasm for research and allowing me to interact with patients at such an early stage in my career.

Upon graduating with my bachelor's degree, I have Dr. Grist to thank for hiring me into a research specialist position. It was a pleasure to have the opportunity to work with Liz Sadowski, MD, Arjang Djamali, MD, and again with Sean Fain, PhD. During my year as a research specialist and the subsequent two years of medical school, Drs. Sadowski, Djamali, and Fain gave me great opportunities to expand my experiences through working on perfusion and oxygen bioavailability measurements in both pigs and humans. They also allowed me great freedom to design the animal studies that we performed together; the experience of designing such studies has been extremely valuable to my research career to date. Additionally, they were very kind to accommodate my schedule so that I could operate the animal studies and attend medical school concomitantly. Also during my time in medical school I had the privilege of working with Howard Rowley, MD, Aaron Field, MD, PhD, and Karl Vigen, PhD on anomalous asymmetry in MR perfusion studies. I appreciate their willingness to adapt to the brief time I had in medical school to perform such a study. While the research I performed with Drs. Haughton, Sadowski, Djamali, Fain, Rowley, Field, and Vigen are not detailed in this dissertation, I do not mean to

give it any less importance. I wish to thank all of them for the plethora of wonderful experiences I had with them and to express my gratitude for how greatly these experiences have contributed to my education.

Upon entering graduate school I was pleased to begin working with Oliver Wieben, PhD again. I thank Dr. Wieben for his willingness to work with Dr. Grist in co-advising me through my graduate school years. Dr. Wieben is a pleasure to work with and has a lovely and jovial demeanor. Dr. Wieben has given me a great amount of freedom to explore my research interests, whether it was in my attempts at phase contrast HYPR processing or submitting an F30 grant and devising a completely new study in an animal model. I have benefited much from Dr. Wieben's advising over the years in both family- and research-related matters. Also during my graduate school years I would like to thank Alex Frydrychowicz, MD, whose excitement for new ideas has consistently invigorated my own interests and research efforts. The work I performed with Dr. Frydrychowicz, particularly regarding pulse wave velocity measurements, led to a substantial portion of this dissertation and was the inspiration for the majority of the research I proposed for my NIH F30 fellowship. If it weren't for Dr. Frydrychowicz, I would be writing about something very different for my dissertation. I'd also like to thank Chris François, MD, who has kept me in touch with clinical imaging research. My work with Dr. François, particularly regarding wall shear stress, was also vital to this dissertation.

In my graduate years I have called on Kevin Johnson, PhD several times for his expertise. I have Dr. Johnson to thank for advice on programming the PWV tool and the development of the McKinnon-Bates sparsification algorithm. Dr. Johnson has a noteworthy ability to quickly and adeptly help others in need. This dissertation would not be the same without his aid.

Additionally, I've worked with a number of students over the years. For their help and collaboration, I'd like to thank David Niles, MS, Nathan Artz, PhD, Shilpa Panth, MS, Sara Alford, MD, PhD, Michael Loecher, MS, Liz Nett, PhD, Ashley Anderson, MS, Erik Bieging, MS, MD, Larry Hernandez, MS, Warren Chang, MD, and Christina Boncyk, MD. I'd like to especially thank Dr. Alford, who was a student under Dr. Grist when I was an undergraduate. She was the first person to introduce me to the concept of doing an MD/PhD program; I have to consider the possibility that I would not be in an MD/PhD program if it were not for her.

Through the years I have conducted a number of human and animal studies. Such studies would not be possible without the aid of Kelli Hellenbrand and Dan Consigny. In all likelihood I spent more time with Kelli and Dan in my research career than with any other individual. Both of them were absolutely essential in getting my studies completed. And above the research itself, it has been a pleasure to work with them. Beth Danielak has also been generous with her time over the years—fulfilling my requests and questions with a smile. Beth, Dan, and Kelli have truly enhanced my time in the MRI research group.

Our collaborators in the UW Department of Animal Sciences have been very generous and useful to my dissertation. Christian Krueger, Jen Meudt, MS, Dhanu Shanmuganayagam, PhD, and Jess Reed, PhD have been instrumental in designing the animal studies and providing the resources to make these studies possible.

I'd like to thank my defense and prelim committee, which includes Oliver Wieben, PhD, Thomas Grist, MD, Tomy Varghese, PhD, Frank Korosec, PhD, Deane Mosher, MD, and Charles Mistretta, PhD.

Although mentioned multiple times in this acknowledgement section, I want to emphasize that Dr. Grist has been the backbone of my research experiences that span over a decade. Dr. Grist has been my ardent supporter since those fateful days in 2003. He has supported me in every one of my endeavors, from my undergraduate work, to my time as a research specialist, to my admission to the MD/PhD program, and to the research during my medical and graduate school years. Additionally, Dr. Grist's charismatic personality and enthusiastic attitude have been my source of inspiration for many years.

Finally, I'd like to thank my parents and grandparents, in particular my mother and maternal grandparents. They gave me every resource I ever needed to excel and they instilled in me from youth the importance of education above all else. I'd be nowhere without them. Most of all I am extremely grateful for the support of my wife, Najia. Najia and I met on the first day of our undergraduate career. Ever since that day she has consistently encouraged me to challenge myself, whether in obtaining a research position in my undergraduate years or in applying to an MD/PhD program. She has been my constant and unwavering companion through all my hardships. I'd also like to thank my son, Zaafir, who has truly enriched my life in ways I could never imagine. He never fails to brighten my day. I'd also like to thank Najia's parents, who have generously taken care of Zaafir virtually whenever I needed. A balanced life in an MD/PhD program and with a child on top of it all would not have been possible without their help. For them I say 'thank you.'

Table of Contents

List of Figures

List of Tables

Chapter 1 Introduction

In recent years phase contrast (PC) magnetic resonance imaging (MRI) has become more common as a tool to investigate anatomy, angiography, and flow and velocity information. A number of studies have investigated the derivation of hemodynamic parameters from PC MRI exams. These parameters have the potential to provide valuable information on a variety of vascular disease states, including aneurysms and atherosclerosis. However, the influence of PC MRI has been hampered by the long scan times required for velocity encoding; spatiotemporal resolution is often compromised to compensate for long scan times. Such limitations affect the derivation of various hemodynamic parameters that require high spatial or temporal resolution.

The work in this dissertation investigates the use of radially undersampled PC MR acquisitions for the evaluation of atherosclerosis. Radially undersampled PC acquisitions provide greater spatiotemporal resolution and reduced scan times in trade for undersampling artifacts. While such undersampling artifacts are generally considered acceptable, part of this dissertation explores the effects of these artifacts on flow measurements and derived hemodynamic parameters. Furthermore, the use of a so-called "4D" radially undersampled PC MR technique with three-directional velocity encoding is explored for the evaluation of atherosclerosis. The outline of this dissertation is as follows:

Chapter 2: Cardiovascular Disease and Atherosclerosis reviews the pathophysiology of cardiovascular disease and atherosclerosis and discusses the epidemiology of these diseases. Current diagnostic tests for cardiovascular disease are discussed, including the Framingham risk

score as well as imaging-based tests. The chapter concludes with a description of familial hypercholesterolemia, which is pertinent for the animal studies included in this dissertation.

Chapter 3: Magnetic Resonance Imaging outlines the essentials of MRI physics, beginning with a description of MR signal generation and detection. While several contrast mechanisms and sequence designs exist in MRI, including spin echoes, free induction decays, and gradient echoes, only gradient echoes are discussed given that they are used in phase contrast imaging—the focus of this dissertation. Next, signal localization and gradients are discussed, including a description of slice selection, spatial encoding, and k-space sampling.

Chapter 4: Phase Contrast Magnetic Resonance Imaging discusses the basic physics of velocity-sensitive PC magnetic resonance imaging. This chapter includes a discussion on both uni- (2D PC) and three-directional velocity encoding (3D/4D PC). Additionally, hemodynamic parameters derived from PC imaging are discussed, including a description of wall shear stress, pulse wave velocity, and other PC-derived hemodynamic parameters.

Chapter 5: Rapid Magnetic Resonance Imaging reviews a number of techniques that have been developed to accelerate the acquisition of MRI data. The use of radial undersampling is discussed in detail, as it underlies the acquisition methods utilized throughout this dissertation.

Chapter 6: Validation of Radial Undersampled 2D Phase Contrast Flow Measurements discusses the evaluation of a radially undersampled 2D PC acquisition in flow phantoms and in healthy human volunteers. The chapter describes a systematic comparison of 2D PC-derived flow measurements versus the known flow rates of a flow phantom pump. Flow measurements are evaluated from 1 – 10 ml/s with both constant and sinusoidal flow waveforms.

Furthermore, in- and out-flow is compared in the aorta and iliac bifurcation in five healthy human volunteers to evaluate the radially undersampled 2D PC acquisition in vivo.

Chapter 7: Aortic Pulse Wave Velocity Measurements with 4D Radial Undersampled Phase Contrast MRI describes the development of a tool for measuring pulse wave velocity (PWV) from both 2D PC data as well as a radially undersampled 4D PC acquisition. Four PWV algorithms for evaluating flow waveforms are integrated into the analysis tool. 2D and 4D PC-derived PWV measurements are computed and compared in twenty healthy human volunteers.

Chapter 8: Wall Shear Stress Downstream of an Aneurysm details the use of a radially undersampled 4D PC acquisition to derive wall shear stress (WSS) measurements in patients with an ascending aortic aneurysm. More specifically, the downstream effects of the aneurysm are evaluated via the computation of WSS in the descending aortic of these patients. WSS results in patients are compared to WSS values in the descending aorta of age-matched healthy human volunteers.

Chapter 9: Repeatability and Internal Consistency of Flow Measurements entails the evaluation of flow measurements in the abdominal vasculature with the use of a radially undersampled 4D PC acquisition. 4D PC flow measurements are assessed via the repeatability of flow measurements in the renal arteries and pararenal aorta, as well as the internal consistency (in- versus out-flow) in these vessels. Repeatability and internal consistency of 4D PC flow measurements are evaluated and compared to 2D PC flow measurements in ten healthy human volunteers.

Chapter 10: Evaluation of Atherosclerosis in Swine describes the MRI-derived evaluation of atherosclerosis in swine with familial hypercholesterolemia. 2D and 4D PC flow measurements are acquired in the descending aorta of eleven swine. Five of those swine sustained substantial plaque development in a four-week time period secondary to a balloon catheter induced injury in the pararenal aorta with a concomitant high cholesterol/fat diet. WSS and PWV measurements are evaluated in the eleven swine and compared between the injured and uninjured swine groups.

Chapter 11: Phase Contrast with Highly Constrained Backprojection and McKinnon-Bates Sparsification describes the development of image sparsification algorithms as well as PC HYPR and McKinnon-Bates-based approaches to reconstructing radially acquired PC data. These approaches are used to improve image quality from highly undersampled radial PC data.

Chapter 12: Summary and Recommendations recapitulates the contributions of this dissertation. Future work and potential derivatives of this work are discussed.

Chapter 2 Cardiovascular Disease and Atherosclerosis

This chapter consists of background information on atherosclerosis, cardiovascular disease, and familial hypercholesterolemia to provide a clinical point of reference for the techniques developed and explored in this dissertation. The pathophysiology, as well as the current diagnostic tests used for the evaluation of these diseases, is discussed.

2.1 Background

Atherosclerosis is defined as thickening of the arterial vessel wall due to the accumulation of various fatty materials, especially cholesterol. These atherosclerotic lesions, also known as atheromas, eventually protrude into the vessel. Such an encroachment may lead to stenosis and therefore a reduction in blood flow through the vessel. A number of other complications may arise from atherosclerotic plaques; for example, rupture of a plaque may lead to thrombosis, total vessel occlusion, and embolisms. Furthermore, plaques weaken the underlying vessel wall media and may lead to the development of an aneurysm. Due to these complications, atherosclerosis is the leading cause of cardiovascular disease (CVD) in the Western world.

Arterial thickening is typically considered a reaction-to-injury and therefore is the result of a chronic inflammatory process that leads to the accumulations of macrophages and low-density lipoprotein (LDL) cholesterol. There are numerous factors that contribute to the accumulation of these materials (1), including endothelial dysfunction, dyslipidemia, inflammation, and smoking (2). These factors lead to endothelial injury, which causes an increase in vascular permeability and leukocyte adhesion. Subsequently, macrophages within the

atheroma are activated and smooth muscle proliferates within the intima. The macrophages and smooth muscle cells within the atheroma engulf lipids, such as LDL, which leads to the development of a fatty streak and a significant increase in size of the atherosclerotic plaque. The deposition of extracellular matrix (ECM) within the plaque turns the fatty streak into a mature atheroma, which has a greater potential for rupture.

In terms of epidemiology, atherosclerosis begins in childhood and remains subclinical for decades. Studies have demonstrated that all individuals between the ages of 15 and 34 years have some degree of aortic fatty streaks (3). Atherosclerotic-induced CVD is typically not clinically manifest until middle age. Aside from age and gender, family history is the most important risk factor for atherosclerosis (2); such risk is often considered multifactorial in nature, given not only genetic polymorphisms but also the familial tendency to develop hypertension and diabetes—two major contributors to atherosclerosis (4).

2.2 Current Diagnostic Tests

Currently the standard method of assessing a patient's risk of a cardiovascular event is with the computation of a Framingham Risk Score (FRS) (5), which considers a subject's age, gender, total and high density lipoprotein cholesterol, smoking status, systolic blood pressure, and the use of blood pressure medications. However, the FRS is limited, as a number of individuals who suffer a myocardial infarction are categorized as low-risk and therefore are not placed on preventative medical therapy (6). The FRS is an insensitive test because it was developed from a predominantly Caucasian population (7) and fails to account for some major risk factors, such as diabetes, obesity, and (sedentary) lifestyles (8). Furthermore, via the FRS 85% of healthy adults are classified as low risk and 2% are classified as high risk; however, 33%

of these people die from CVD (8). Part of the problem with risk assessments, including the FRS, is that sensitivity decreases as risk factors become more prevalent. While there is undoubtedly a causal relationship between obesity and CVD, obesity is no longer a strong predictor of a cardiovascular event since obesity is highly prevalent in society. More sensitive methods would be useful for evaluating CVD, especially if such methods are capable of detecting disease not yet clinically apparent.

Imaging-based strategies for assessing CVD may be more sensitive than risk assessments, such as the FRS. Digital subtraction angiography (DSA) allows for the visualization of the vasculature and atherosclerotic plaques; however, DSA is limited by the pathophysiological mechanism by which atherosclerotic plaques develop. More specifically, most vessels remodel themselves outwardly to compensate for the development of a plaque (9); this process, known as the Glagov phenomenon, serves to preserve the vessel lumen until at least ≥40% of the vessel area is covered with plaque (10). As a result, x-ray angiography is not particularly sensitive to atherosclerotic plaques in the early stages of development.

Computed tomography (CT) has also been used for evaluating atherosclerosis via the radiopacity of calcium within many advanced plaques. However, several problems exist in the evaluation of calcium with CT, including the use of ionizing radiation, the absence of calcium in less well-developed plaques and in some advanced plaques, and the lack of any association between the presence of calcium and the stability of a plaque (11, 12). However, calcium scoring with CT is considered a mature technology and has been well-established in the literature (13) as being a strong predictor of CVD, especially in combination with the FRS (14, 15).

B-mode ultrasound imaging for the measurement of carotid intima-medial thickness (CIMT) was developed and validated (16) to represent the stage of atherosclerosis indicative of proliferating smooth muscle cells. CIMT measurements with ultrasound have a number of benefits, including ease of use, low cost, its noninvasive nature, and lack of ionizing radiation. However, intimal thickening can occur in the absence of atherosclerosis (17). Furthermore and contrary to the use of CT-based coronary calcium scoring (14, 15), ultrasound-based CIMT measurements have not demonstrated any predictive benefits to the FRS (18). CIMT measurements may also be user dependent.

2.3 Familial Hypercholesterolemia

Familial hypercholesterolemias (FH) are a group of genetic defects that affect the metabolism of LDL cholesterol (19). LDL levels in heterozygous FH patients are typically 325-450 mg/dl (normal: <70-100 mg/dl). Patients with such high levels of LDL cholesterol are at very high risk of developing atherosclerosis and CVD. Heterozygous FH is fairly common, with a prevalence of 1 in 500 in the United States and United Kingdom, with greater prevalence in many other nations. The homozygous form of FH is fairly rare with a prevalence of 1 in a million (20).

The primary mutation associated with FH is on the LDL receptor gene. This mutation can reduce the number of LDL receptors found in the liver and/or may affect receptor/ligand binding (21). The diagnosis of FH is made clinically and is multifaceted, with elevated LDL cholesterol being essential. The diagnosis is strengthened if a subject also has a family history of hypercholesterolemia in childhood, a family history of premature CVD, and tendon xanthomas (20). FH can be confirmed with genetic testing, but such testing is rarely performed given the

large number of mutations associated with this disease and that genetic testing does not affect treatment planning.

In **Chapter 10 Evaluation of Atherosclerosis in Swine**, FH pigs are used as a model for elevated LDL cholesterol levels and the development of atherosclerosis. FH serves as an excellent model to evaluate techniques for the early detection of atherosclerosis.

Chapter 3 Magnetic Resonance Imaging

This chapter discusses the underlying principles of magnetic resonance imaging (MRI), including the magnetic resonance phenomenon, excitation, relaxation, signal characteristics, spatial encoding, and k-space. While the MR phenomenon is most accurately described via quantum mechanics, predominantly classical descriptions are used for both clarity and brevity.

3.1 MR Signal Generation and Detection

3.1.1 Spins, Electromagnetism, and Magnetic Moments

Angular momentum, $\vec{J}$, is a property of nuclei with an odd atomic weight or number. Nuclei with an angular momentum are often referred to as spins. A set of atoms of the same kind are referred to as a nuclear spin system. Hydrogen is the most abundant atom in the human body that possesses an angular momentum and therefore is the most commonly used nuclear spin system in MRI.

Spin is typically thought of as the movement of a nucleus around an axis of rotation. Given the odd atomic numbers of nuclear spins, spins hold an electrical charge. The rotation of a charged particle about an axis creates a magnetic field. Such a magnetic field is created perpendicular to the plane of rotation and is thus known as a magnetic moment, $\vec{\mu}$. The spin angular momentum and magnetic moment are related by

$$\vec{\mu} = \gamma \vec{J} \qquad \text{Eq. 3.1}$$

where γ is the gyromagnetic ratio, which is a nucleus-dependent quantity. A commonly reported variant of the gyromagnetic ratio, $\bar{\gamma}$, equals $\gamma/2\pi$. For example, the gyromagnetic ratio ($\bar{\gamma}$) of hydrogen is 42.58 MHz/T.

The orientation of the vector quantity, $\vec{\mu}$, is random when no external magnetic field is acting on a spin or a nuclear spin system. Such randomness is attributed to thermal random motion present in a system in thermal equilibrium. For a nuclear spin system, the random orientations of these vector quantities will cancel upon summation. As a result, objects, including humans, do not normally have a net magnetic field. However, in the presence of an external magnetic field, as is used in MRI, spins will align with this strong magnetic field.

In MRI, we assume a convention that a strong magnetic field, B_0, is applied in the z-direction of the laboratory frame,

$$\vec{B}_0 = B_0\vec{k} \qquad \text{Eq. 3.2}$$

The interaction between a proton's spin and the B_0 magnetic field creates a torque that leads to the precession, or rotation, of the spin around the fixed axis of the magnetic field, $\vec{B}_0$. This torque is represented by the rate of change in angular momentum,

$$\frac{d\vec{J}}{dt} = \vec{\mu} \times B_0\vec{k} \qquad \text{Eq. 3.3}$$

Substituting Eq. 3.1 into Eq. 3.3 yields the equation of motion for spins due to the effect of torque created by the strong magnetic field, B_0,

$$\frac{d\vec{\mu}}{dt} = \gamma\vec{\mu} \times B_0\vec{k} \qquad \text{Eq. 3.4}$$

The elementary quantum model of the hydrogen atom predicts the orientation of the magnetic moment vector in the presence of the B_0 magnetic field. These orientations are computed by

$$\mu_z = \gamma m_I \hbar \qquad \text{Eq. 3.5}$$

where $\hbar$ is Planck's constant ($6.6 \times 10^{-34}/2\pi$ J·s) and m_I is the magnetic quantum number. m_I, for an atom with a nonzero spin, has 2I + 1 values, in which I is the nuclear spin quantum number. For the ^{1}H nucleus, I = ½. As a result, m_I has two possible values, -I and +I, or -½ and +½. These two values of m_I correspond to either a parallel or anti-parallel orientation of the magnetic moment vector in the presence of the B_0 magnetic field.

The average thermal energy, kT, where k is the Boltzmann's constant (1.38×10^{-23} $m^2 \cdot kg \cdot s^{-2} \cdot K^{-1}$) and T is temperature, can be used to demonstrate that less energy is required for the parallel alignment than for the anti-parallel alignment. While there is extensive cancellation of the parallel and anti-parallel vectors quantities, there is a net parallel vector that provides enough of a vector sum to be usable for magnetic resonance imaging. This usable vector sum is not readily apparent. The spin excess, or the difference between the number of spins that are parallel and the number that are anti-parallel, is computed as

$$spin\ excess\ \cong N \frac{\hbar \omega_0}{2kT} \qquad \text{Eq. 3.6}$$

where ω_0 is the precession angular frequency and N is the total number of spins present. For a 1.5 T main magnetic field, this works out to only 5 in a million spins that are in the parallel orientation above the number of spins in the antiparallel orientation. However, this is compensated for via the sheer number of spins that are present in an object of interest. A few

grams of biological tissue contain an Avogadro number of protons (6.022 x 10^{23}). Given this, the equilibrium magnetization, M_0, in the longitudinal, or z-, direction is given by

$$M_0 = \frac{\rho_0 \gamma^2 \hbar^2}{4kT} B_0 \qquad \text{Eq. 3.7}$$

where ρ_0 is the number of protons per unit volume (spin density).

The magnetic moment vector is not directly aligned along the B_0 field due to thermal energy from the absolute temperature, T; rather, the angle between $\vec{\mu}$ and $\vec{B}_0$ is computed as

$$\theta = \cos^{-1} \frac{m_I}{\sqrt{I(I+1)}} \qquad \text{Eq. 3.8}$$

It can be shown that for protons, the angle, θ, is ±54°44'. Despite this angle, θ, the transverse component of the magnetic moment vector, $\vec{\mu}_{xy}$, is non-zero because of the random distribution of spins in respect to their alignment in the transverse plane.

The magnetic moment vector precesses at an angle, θ, around the main magnetic field, B_0. This precession occurs at a rate proportionate to the strength of the magnetic field, B_0, at a rate referred to as the Larmor frequency, ω_0. The Larmor frequency is defined as,

$$\overrightarrow{\omega_0} = \gamma \overrightarrow{B_0} \qquad \text{Eq. 3.9}$$

This precession occurs in a clockwise fashion.

3.1.2 Excitation

The net magnetization, $\vec{M}$, can be tipped away from the z-direction with the use of a weak oscillating magnetic field, $\vec{B}_1(t)$. The process of tipping $\vec{M}$ into the transverse plane is referred to as radiofrequency (RF) excitation. The $\vec{B}_1(t)$ field, also known as an RF pulse, oscillates at the

resonant frequency of the nuclear spin system of interest. $\vec{B}_1(t)$ is applied perpendicular to the z-direction such that it creates a torque on the net magnetization, $\vec{M}$. This behavior is described by the simplified Bloch equation:

$$\frac{d\vec{M}}{dt} = \gamma\vec{M} \times \vec{B} \qquad \text{Eq. 3.10}$$

The application of an RF pulse at the resonance frequency of the nuclear spin system allows for $\vec{B}_1(t)$ to be orders of magnitude weaker than the main magnetic field, B_0 (e.g. B_1 = 50 mT vs. B_0 = 1.5 T).

Given that $\vec{M}$ is still precessing at the Larmor frequency around the main magnetic field, B_0, during the process of excitation, the movement of $\vec{M}$ from the longitudinal direction to the transverse plane is a very complex motion. For graphical purposes, this motion is often simplified by considering the entire system in the context of a rotating reference frame. In the rotating reference frame, the transverse plane rotates around the longitudinal, or z-, direction at the Larmor frequency. Given this rotation, excitation of $\vec{M}$ no longer appears to precess and instead undergoes a simple geometric movement from the longitudinal direction to the transverse plane in the presence of a $\vec{B}_1(t)$ field. The degree by which $\vec{M}$ is excitated away from the longitudinal direction is referred to as the flip angle, α, and is determined by the strength of the $\vec{B}_1(t)$ field and the duration of the excitation pulse, τ_p, described as

$$\alpha = \int_0^{\tau_p} \gamma\vec{B}_1(t)dt \qquad \text{Eq. 3.11}$$

3.1.3 Relaxation

Following the excitation of $\vec{M}$, the laws of thermodynamics dictate that the magnetization spin system will return to thermal equilibrium. Given that the main magnetic field, B_0, is still present after the application of the RF pulse, $\vec{M}$ will tend to return to the longitudinal direction following excitation. Two simultaneous processes occur during this return to thermal equilibrium, including the recovery of longitudinal magnetization, M_z, and the decay of transverse magnetization, M_{xy}. The relaxation of the longitudinal and transverse magnetizations can be described as

$$M_{x'y'}(t) = M_{x'y'}(0_+)e^{-t/T_2} \quad \text{Eq. 3.12}$$

$$M_{z'}(t) = M_z^0\left(1 - e^{-t/T_1}\right) + M_{z'}(0_+)e^{-t/T_1} \quad \text{Eq. 3.13}$$

where $\boldsymbol{M_{x'y'}(0_+)}$ and $\boldsymbol{M_{z'}(0_+)}$ are the magnetizations immediately after an RF pulse and $\boldsymbol{M_z^0}$ is the longitudinal magnetization at thermal equilibrium. It can be shown that the longitudinal relaxation time, T_1, is defined as the time required to recover 63% of the longitudinal magnetization and that the transverse relaxation time, T_2, is defined as the time required for 63% of the transverse magnetization to decay.

3.1.4 Signal Detection

The detection of signal in MRI depends on the Faraday law of electromagnetic induction. When transverse magnetization is created through the excitation of $\vec{M}$, $\vec{M}$ precesses around the longitudinal direction (main magnetic field, B_0). This precession creates a time-varying magnetic field in a receiver coil situated perpendicular to the plane of precession. In turn, this time-varying

magnetic flux induces an electromagnetic force in the receiver coil proportional to the rate of change of the magnetic flux.

3.2 Signal Characteristics

There are three types of signals in MRI: free induction decays, RF (spin) echoes, and gradient echoes. The focus of this dissertation is on velocity-sensitive imaging, which employs gradient echoes. For the sake of brevity, only gradient echoes, as used in PC MRI, will be described in detail.

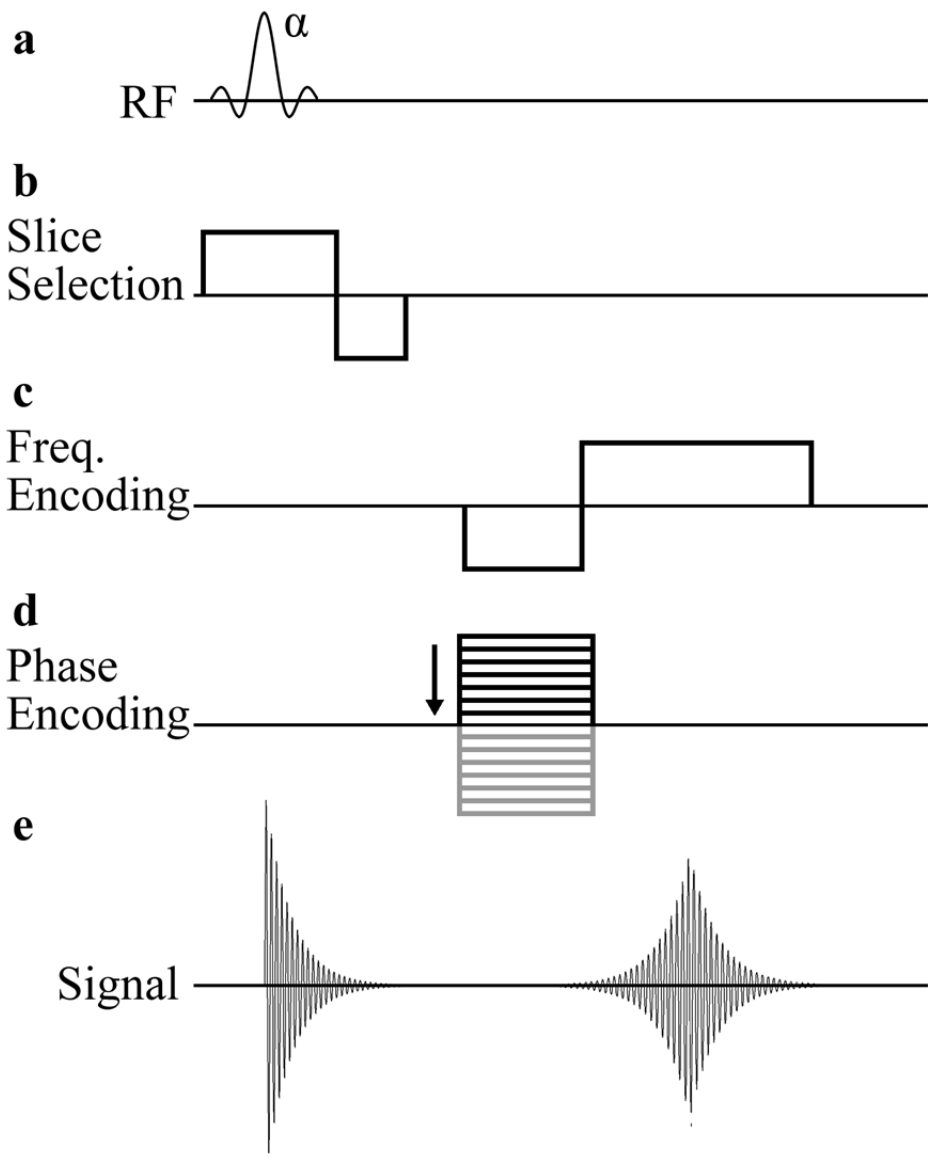

Figure 3.1 Gradient-echo pulse sequence with RF excitation (**a**). A slice-selection gradient (**b**) modulates precessional frequency linearly across an object; this linear variation in precessional frequency determines the bandwidth used in the RF pulse (**a**). Spatial encoding is performed both with frequency-encoding (**c**) and phase-encoding (**d**) gradients, the latter of which is incremented for each repetition time throughout the duration of the acquisition. The application of the negative lobe of the frequency encoding gradient causes dephasing and signal decay. An equal and opposite gradient causes refocusing and the regrowth of signal (**c**). A signal is generated and detected (**e**) when the area of the frequency encoding gradient is equal in magnitude to the prewinding gradient. The magnitude of the refocused signal is reduced after excitation due to T_2* decay (**e**). Figure adapted from Bernstein's *Handbook of MRI Pulse Sequences* (22).

Unlike spin echoes that employ a 180° refocusing pulse to obtain an echo, gradient echoes use gradient reversal in the frequency-encoding direction (see below in section **3.3.2 Spatial Encoding**) to obtain an echo (Figure 3.1c). This process is initiated first via an RF excitation pulse (Figure 3.1a), followed by a gradient lobe that serves to dephase spins in the transverse plane (Figure 3.1c). The spins are then rephased with a gradient lobe of equal and opposite polarity to the initial gradient. A gradient echo occurs when the magnitude of the two gradient lobes are equal (Figure 3.1c,e).

The GRE pulse sequence and the application of an RF excitation pulse is repeated until an object is adequately sampled (see below in section **3.3.3 k-Space Sampling**). The time between each repetition of the pulse sequence is known as the repetition time, TR. GRE is a fast imaging technique because the α RF pulse typically employed in the pulse sequence is less than 90°. The steady state condition necessary for the imaging experiment is achieved with gradient spoiling to delete any remaining transverse magnetization at the end of each TR. Depending on the implementation, additional radiofrequency spoiling might be applied. As a result, the pulse sequence does not require the recovery of longitudinal magnetization. Since the T_1 recovery time is reduced in this manner, TRs can be shortened, typically to within 2-50 ms. During the echo time phase continues to accumulate in the transverse plane; as a result GRE images have a contrast weighting related to $e^{-TE/T2^*}$, in which T_2^* is defined as

$$\frac{1}{T_2^*} = \frac{1}{T_2} + \frac{1}{T_2'} \qquad \text{Eq. 3.14}$$

where T_2' is inversely proportional to ΔB, the magnetic field inhomogeneity in a given voxel.

3.3 Signal Localization and Gradients

3.3.1 Slice Selection

Individual slices are imaged in MR with the use of a slice-selection gradient (Figure 3.1b). Slice-selection gradients are typically constant and are employed simultaneously with RF excitation. Since the magnetic field strength is modulated by the slice selection gradient, and because the strength of the magnetic field directly affects a spin's rate of precession (Eq. 3.9), spin precession rates will vary linearly along the direction of the slice-selection gradient. Slice selection is thus directly performed via RF excitation, because the RF pulse has a frequency bandwidth, Δf (in Hertz). The band of frequencies defined by Δf determines the spatial band, or slice, that is excited for the subsequent pulse sequence. In MR, slice selection can be performed in any orientation via the linear combination of slice-selection gradients on any of the three main axes.

3.3.2 Spatial Encoding

Following RF excitation and slice selection, spatial encoding within a slice is performed. Spatial encoding begins with a frequency-encoding gradient (Figure 3.1c), G_x, which linearly applies a gradient along one direction of a 2D slice, causing precessional rates to vary linearly across the object of interest (Eq. 3.9). This variation in magnetic field strength, based on Eq. 3.2, is represented by

$$\vec{B}_0 = (B_0 + G_x x)\vec{k} \qquad \text{Eq. 3.15}$$

Therefore, the object of interest will have a range of frequencies that correspond to spatial location. In traditional Fourier-encoded pulse sequences, the frequency-encoding direction is

constant. In radially-acquired pulse sequences, the frequency-encoding direction continually varies.

In addition to frequency-encoding, phase-encoding gradients are also used to spatially encode Fourier pulse sequences (Figure 3.1d). Phase-encoding is not employed in radial acquisitions. Unlike frequency-encoding, which creates a linear variation in space of the precessional frequency of spins, phase-encoding creates a linear spatial variation of phase. Phase-encoding is performed with the application of a gradient after transverse magnetization has been created with RF excitation. This gradient lobe is varied in size by modifying the area under the gradient in order to create a varied amount of phase accumulation. With each iteration in the strength of the phase-encoding gradient, a different horizontal line is sampled in k-space (Figure 3.2a).

3.3.3 k-Space Sampling

It can be shown that the frequency- and phase-encoding gradients allow one to actually sample the MR raw data in Fourier space, also referred to as k-space (Figure 3.2). A simple 2D Fourier transform is then used to reconstruct an image from the sampled k-space.

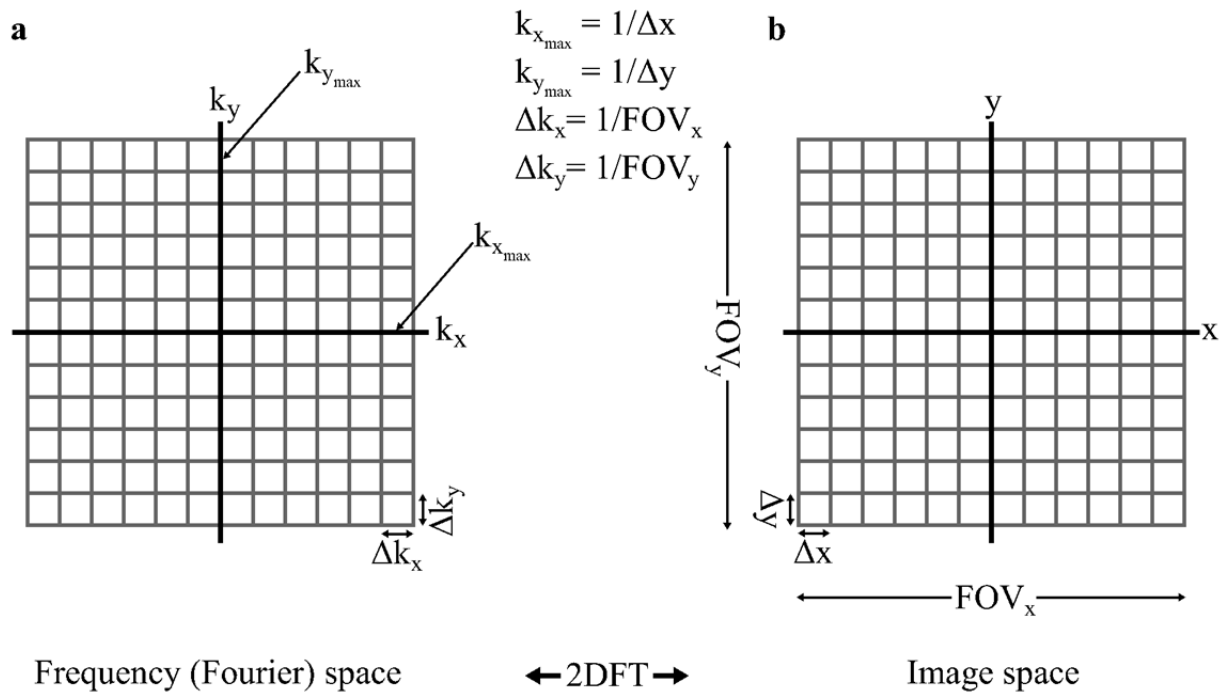

Figure 3.2 Frequency (Fourier) space is often referred to as k-space (**a**), with a horizontal axis defined as the readout direction, k_x, and a vertical axis defined as the phase encoding direction, k_y. In traditional Fourier-encoded imaging, the k_x direction is sampled with the use of frequency-encoding gradients. The k_y direction is sampled with the use of a phase encoding gradient, in which the same frequency-encoded gradient is employed but the signal is modulated with the phase-encoding gradient. The phase-encoding gradient is incremented, which directly corresponds to a different horizontal line sampled in k-space. A 2D FT (Fourier transform) is used to reconstruct an image from k-space.

There are a number of unique properties that correlate between the k-space (frequency) domain and the image space (spatial) domain. For example, the spacing between points sampled in k-space, Δk, is inversely related to the field of view (FOV) in the reconstructed image, $\Delta k = 1/FOV$ (Figure 3.2). The FOV is treated separately for each dimension of the image, such that

$$\Delta k_x = \frac{1}{FOV_x} \qquad \text{Eq. 3.16}$$

$$\Delta k_y = \frac{1}{FOV_y} \qquad \text{Eq. 3.17}$$

Additionally, the last point sampled (i.e. the highest spatial frequency) in each dimension of k-space determines the spacing, or spatial resolution, in image space (Figure 3.2). In other words,

$$k_{x_{max}} = \frac{1}{\Delta x} \quad \text{Eq. 3.18}$$

$$k_{y_{max}} = \frac{1}{\Delta y} \quad \text{Eq. 3.19}$$

where $k_{x_{max}}$ and $k_{y_{max}}$ are the highest spatial frequencies sampled in k-space in the k_x- and k_y-directions, respectively, and Δx and Δy represent the spatial resolution in the x- and y-directions in image space, respectively.

The central region of k-space corresponds to low spatial frequency information, whereas the outer regions of k-space correspond to high spatial frequency information. Note that high frequency information represents the edges of objects within an image. Additionally, there is substantial redundancy in k-space. Because of these properties, techniques have been developed to accelerate image acquisition and k-space sampling by either omitting k-space data points in return for artifacts that may or may not be acceptable, or omitting k-space data points and approximating them for a pseudo-complete sampled k-space. Such techniques are described in further detail in **Chapter 5 Rapid Magnetic Resonance Imaging**.

Chapter 4 Phase Contrast Magnetic Resonance Imaging

This chapter reviews the basic physics of velocity-sensitive encoding in magnetic resonance imaging. A number of hemodynamic parameters can be derived from such velocity-sensitive data sets, particularly biomarkers that reflect the disease state of atherosclerosis. Two such biomarkers—wall shear stress and pulse wave velocity—are discussed in detail here.

4.1 Theory

Phase contrast (PC) magnetic resonance imaging (MRI) employs flow-sensitizing (bipolar) gradients to encode flow into the phase component of MR signal (23-25). In general, each of the principal axes (frequency encoding, phase encoding, and slice selection) in MR are treated separately, and therefore, flow-sensitizing gradients are individually added to one or more of these axes to encode velocity in any arbitrary direction. Bipolar gradients are the most common flow-sensitizing gradients employed in PC MRI (Figure 4.1), coupled with a gradient-echo sequence.

Stationary spins (x_1 in Figure 4.1c) experience equal and opposite magnetic fields as a result of a bipolar flow-sensitizing gradient. As a result, no net phase is accumulated after the bipolar gradient is played out (Figure 4.1d). In comparison, a spin moving (x_0 in Figure 4.1c) in the direction of the bipolar gradient experiences a different magnetic field and consequently its precession frequency changes as it experiences a spatially varying magnetic field. After both gradient lobes of the bipolar gradient have been applied, the change in precessional frequency results in the accumulation of net phase (Figure 4.1d). Since the velocity of the moving spin affects the difference in gradient strength experienced at the time of each gradient lobe, the phase

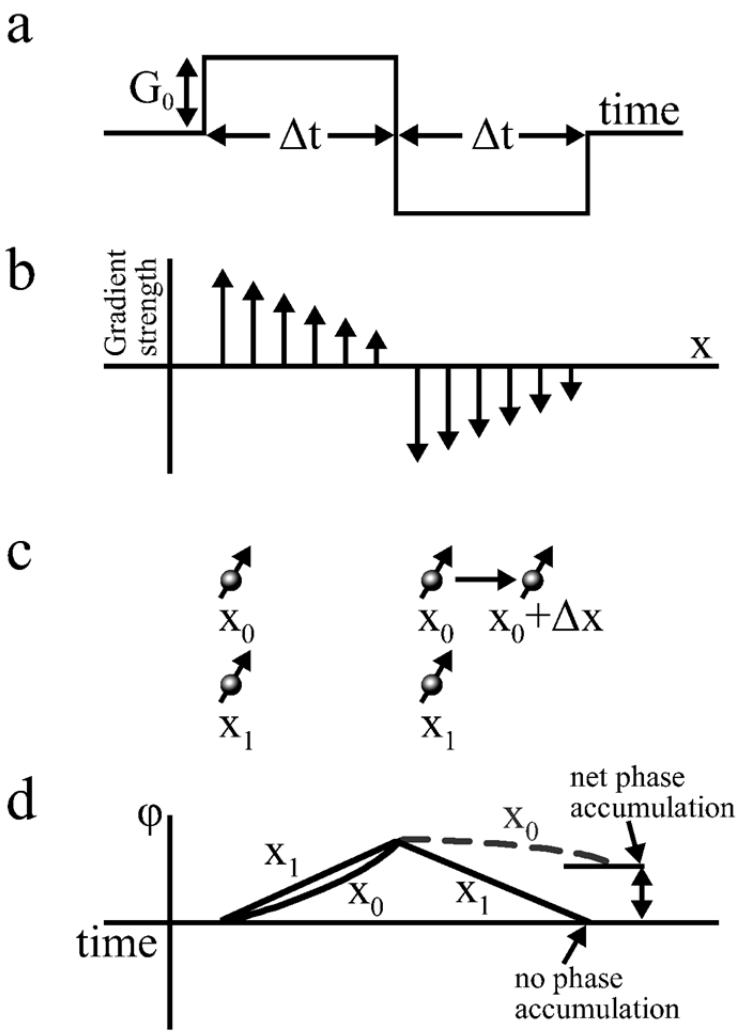

Figure 4.1 Bipolar—equal and opposite—velocity encoding gradients are employed in phase contrast magnetic resonance imaging (**a**). The gradients applied in (**a**) create a spatially varying magnetic field (**b**) that causes spins to precess at a rate proportional to the strength of the magnetic field (Eq. 3.9). Two spins are shown (**c**), x_0 and x_1. x_0 moves to a location of $x_0 + \Delta x$ by the time the negative lobe of the bipolar gradient is applied, whereas x_1 is stationary and therefore experiences an equal and opposite magnetic field between the two lobes of the bipolar gradient. x_1 therefore accumulates phase during the application of the positive lobe, but experiences an equal loss in phase as a result of the negative lobe (**d**). In the end x_1 accumulates no phase. In comparison, the movement of x_0 causes this spin to experience a weaker magnetic field during the application of the negative lobe. As a result, the phase accumulated during the positive gradient will not be completely lost during the negative lobe (**d**). x_0 will accrue a net phase by the end of the bipolar gradient. Note that x_0 moves during the application of the bipolar gradient, causing the phase accumulation to be quadratic in nature (**d**); in comparison, stationary spins, such as x_1, do not move during the application of the bipolar gradient and thus accumulate phase in a linear fashion. Figure adapted from Bernstein's *Handbook of MRI Pulse Sequences* (22) and Korosec's and Turski's review of phase contrast imaging (26).

accumulated is directly proportional to the velocity of the spin. Note that a spin moving in a direction perpendicular to this bipolar gradient will experience no net accumulation of phase.

Velocity encoding is based on the gradient first moment. The zeroth order moment, m_0, is nulled because the areas of the two lobes of the bipolar gradient cancel one another. We can compute the first moment of the gradient, based on Figure 4.1a, as the following:

$$m_1 = \int_0^{\Delta T} G_0 t dt + \int_{\Delta T}^{2\Delta T} -G_0 t dt \qquad \text{Eq. 4.1}$$

When Eq. 4.1 is integrated and simplified, m_1 equals,

$$m_1 = \frac{G_0}{2}(\Delta T^2 - 3\Delta T^2) = -G_0 \Delta T^2 \qquad \text{Eq. 4.2}$$

The area of one gradient lobe is equal to $A = G_0 \Delta T$. Therefore, **Eq. 4.2** simplifies to,

$$m_1 = -A\Delta T \qquad \text{Eq. 4.3}$$

Thus, the phase accumulated by the bipolar gradient as a function of a spin's velocity is given by,

$$\varphi = -\gamma A T v \qquad \text{Eq. 4.4}$$

The sign of m_1 matches the sign of the last gradient lobe, as seen in Figure 4.1a.

Aside from bipolar velocity-sensitizing gradients, a number of other factors lead to the accumulation of phase, such as susceptibility, chemical shift, field inhomogeneities, and electronic sources (26). To mitigate the effects of these factors, two phase-sensitive images are acquired, with one image acquired with the bipolar gradient oriented one direction, and the second image acquired with the bipolar gradient toggled to the opposite orientation (this toggling

approach is also known as balanced encoding; alternatively the second image is acquired with a reference scan, in which $m_0 = m_1 = 0$.) These two images are subtracted from one another and the result is thus known as a phase difference image. This toggling of the bipolar gradients is directly related to the velocity values to which an acquisition is sensitive. The velocity encoding (VENC) value is defined as the maximum velocity value that can be represented by a velocity-sensitive image. The VENC is a user-selected variable that is determined mathematically as,

$$VENC = \frac{\pi}{\gamma|\Delta m_1|} \qquad \text{Eq. 4.5}$$

The velocity, *v*, can be obtained from phase difference images, as

$$\Delta\varphi = \gamma \Delta m_1 v = \frac{v}{VENC}\pi \qquad \text{Eq. 4.6}$$

From Eq. 4.5 it is shown that the maximum phase that can be accumulated without error is ±π (±180°); this is the dynamic range of velocity-sensitive images. Phase angles are only allowed up to ±π rather than 0 - 2π so that the sign can be used to encode direction. If a spin is traveling at a sufficient velocity such that it accumulates a phase greater than ±π, for example a phase angle of +190° (+1.06π), it will be encoded as -170° (-0.94π). This is known as velocity aliasing (Figure 4.2). This problem can be prevented by the user via the selection of a greater VENC value. The VENC setting is inversely proportional to the area under the bipolar gradient and will directly determine the strength of the change in the first moment, m_1, in the toggling of the bipolar gradients. While setting the VENC too low causes aliasing, setting the VENC too high is problematic as well because the velocity-to-noise ratio is inversely proportional to the VENC. For example, setting the VENC to 100 cm/s when the greatest velocity in the vasculature is 50 cm/s, fails to utilize the dynamic range of velocity encoding values and significantly affects the

velocity-to-noise ratio in the images. Hence, the choice of the VENC setting is crucial for proper PC MR imaging.

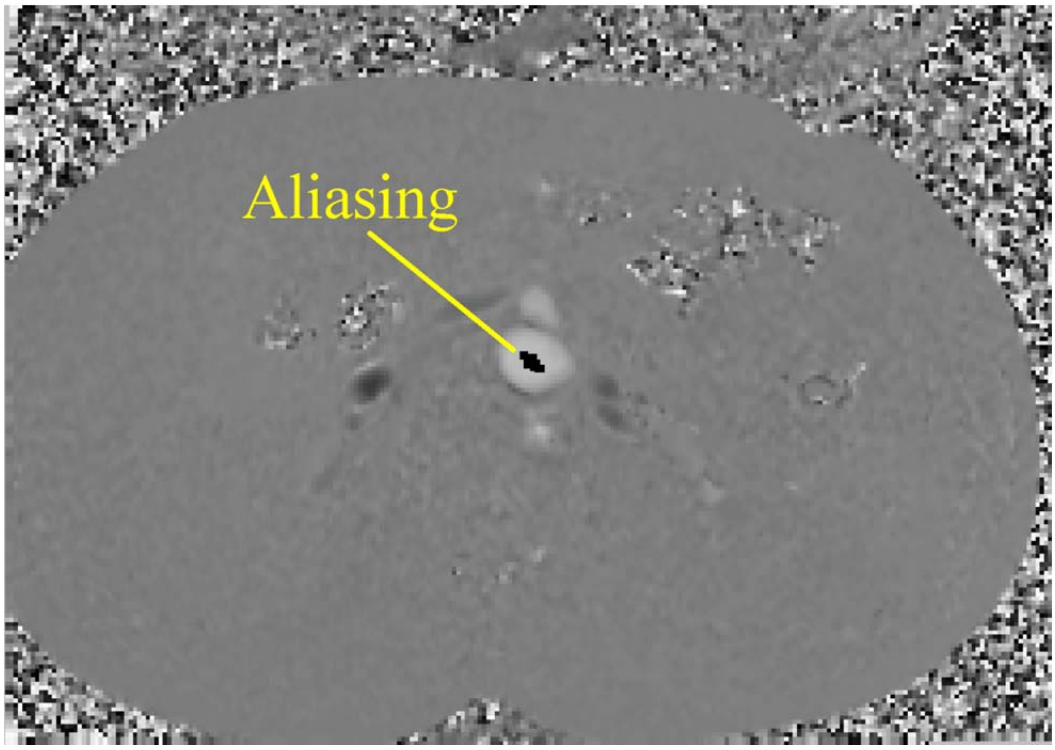

Figure 4.2 Phase difference image of the suprarenal aorta in a healthy human volunteer. When the velocity encoding (VENC) value is set lower than the maximum velocity in the vessel, the measured velocity appears reversed in direction. This error is known as velocity or phase aliasing. Aliasing leads to abrupt changes in the signal intensity values, as shown in the image above.

PC acquisitions are often time-resolved such that the temporal dynamics of flow/velocity can be determined throughout the cardiac cycle (27, 28). Temporally resolved PC data are acquired with the use of ECG (electrocardiogram) or pulse oximeter gating, such that multiple phases, or time frames, along the cardiac cycle are obtained. Each time frame corresponds to a separate image. From each time frame velocity and flow can be obtained from the voxel intensity values within a vessel lumen. Velocities may be obtained by manually or semi-automatically drawing a region of interest (ROI) on a phase difference image (Figure 4.3b,c). Mean velocity is

then obtained by averaging the signal intensity values from all of the voxels within the ROI (recall that voxel signal intensity is based on Eq. 4.6). ROI placement is often guided with magnitude images (Figure 4.3a) or with complex difference images (22), which are generated by a nonlinear combination of the magnitude and phase images from the very same PC MRI scan. ROIs can be drawn on each time frame along the cardiac cycle. A mean velocity or instantaneous

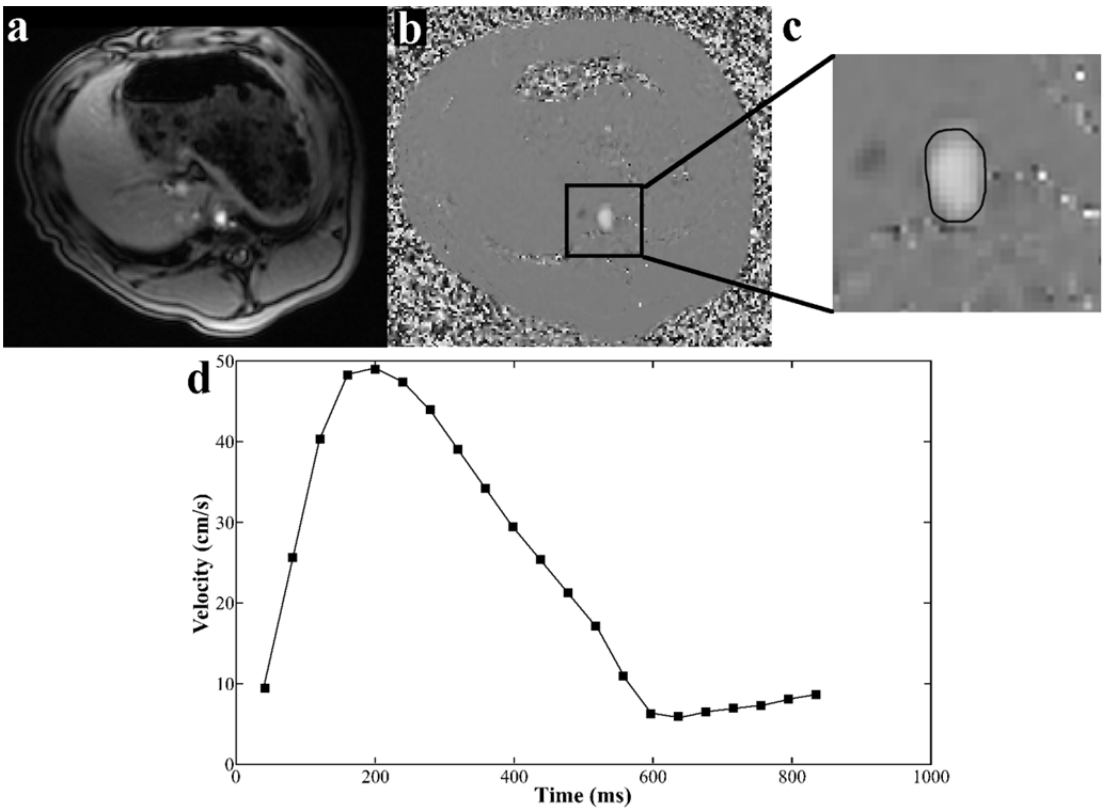

Figure 4.3 Magnitude (**a**) and phase difference (**b**) images from a radially undersampled phase contrast acquisition in the abdominal aorta of a swine with familial hypercholesterolemia. By drawing a region of interest around the vessel lumen of the aorta (**c**), mean velocity can be obtained. If a region of interest is drawn for each time frame from a series of phase difference images, mean velocity over the cardiac cycle can be obtained (**d**). This entity is easily translated into instantaneous flow by multiplication with the area of the ROI for each time frame. Net flow can be calculated by temporal integration.

flow (mean velocity x area) time curve can be created from this series of data and integrated to provide total flow volumes over the cardiac cycle (Figure 4.3d). A number of factors, especially

partial voluming, affect the measurement of velocity and flow from PC images. Although a discussion of these factors is outside of the scope of this review, the manuscripts by Wolf et al., Pelc et al., and Tang et al. provide a more detailed description of these concepts (29-31).

For PC imaging with three-directional velocity encoding, the simplest approach would be to acquire six data sets (a so-called six-point technique), with the bipolar gradients toggled for each of the three directions. However, this is time consuming. The acquisition may be accelerated with the use of a four-point technique. For example, a four-point reference acquisition employs a single reference point ($m_1 = 0$) for all three of the other main velocity encoding directions (32, 33). Alternatively, a balanced four-point, or Hadamard, velocity encoding strategy toggles the bipolar gradients on two axes at a time for all four points. Therefore, velocity encoding is not directly encoded on any of the three main axes. The balanced four-point strategy provides better VNR and less aliasing than the reference four-point method (33) and reduces artifact levels by derating the bipolar gradients. A balanced five-point acquisition has also been proposed, which utilizes a low-resolution fifth point for a scan time increase of ~1% instead of the expected 25% (34). The five-point technique provides further benefits to the VNR and also provides a more symmetric velocity encoded space compared to the balanced four-point method.

Phase contrast acquisitions are time-consuming, especially for three-directional velocity encoding. Since each velocity encode in PC imaging is a separate acquisition, scans times may be prohibitively long. For example, a four-point three-directional velocity-encoded acquisition requires 4x the scan time required of an anatomical scan without velocity encoding; additionally, the bipolar velocity-sensitizing gradients lengthen the TR, and therefore, the scan time, of

velocity-encoded acquisitions. Furthermore, the addition of the temporal axis with a series of three-directional velocity-encoded data sets along the cardiac cycle further lengthens the scan time. Therefore, PC imaging significantly benefits from accelerated imaging techniques, as discussed in **Chapter 5 Rapid Magnetic Resonance Imaging**.

4.2 Wall Shear Stress

Wall shear stress (WSS) is defined as the frictional force per unit area imparted on the vessel wall due to blood flow. The magnitude of wall shear stress is estimated via Poiseuille's law and is defined as

$$\tau = \frac{4\mu Q}{\pi R^3} \qquad \text{Eq. 4.7}$$

where μ is the blood viscosity, Q is the blood flow, and R is the radius (35). Since blood viscosity is normally constant, WSS is substantially affected by changes in blood vessel size and to a lesser extent affected by the rate of blood flow. WSS can be divided into two components—circumferential and axial (Figure 4.4).

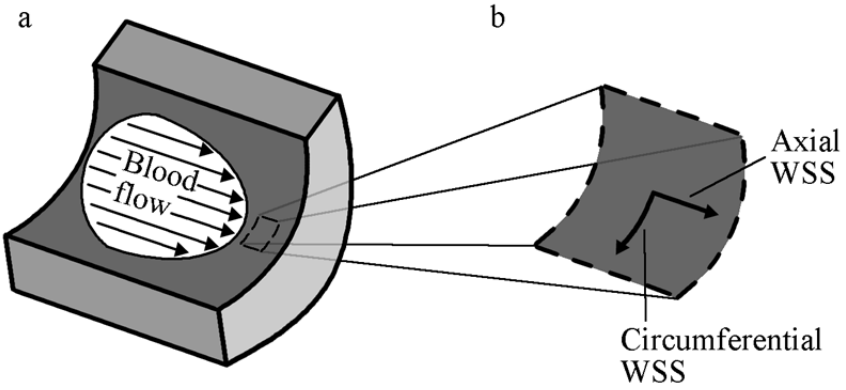

Figure 4.4 Cross-sectional schematic of blood flowing through a vessel. Blood flow imparts a force per unit area on the vessel wall, known as wall shear stress (**a**). The wall shear stress vector can be separated into axial and circumferential components (**b**).

Studies have demonstrated that areas susceptible to the development of atherosclerotic plaques have lower blood flow and therefore lower WSS (36-38). Decreased WSS leads to a compensatory decrease in vessel diameter (39). Areas of lower flow tend to occur around areas of branching points within the vasculature (Figure 4.5); these areas of lower flow are a function of both hemodynamics and anatomy. Areas of the vasculature in which atherosclerotic plaques are uncommon tend to have greater WSS values; therefore, elevated WSS is often considered atheroprotective (40).

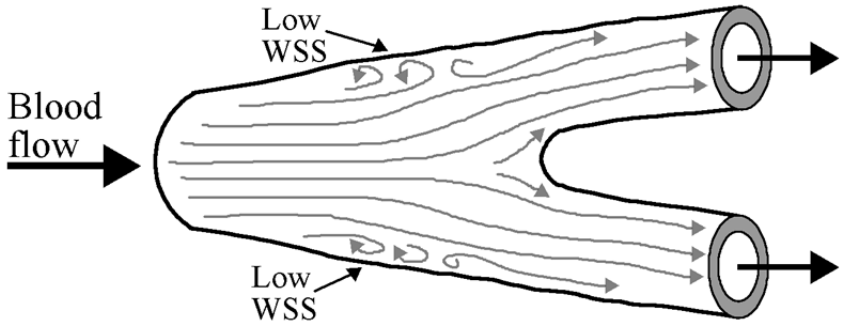

Figure 4.5 Approximate blood flow streamlines at a vessel bifurcation demonstrate recirculatory flow on the outer walls. Areas of low blood flow often lead to areas of low wall shear stress.

Vascular mediators and gene transcription are directly affected by WSS in the vascular endothelium. Animal studies with artificially created increases in WSS have led to an increase in nitric oxide release, which is a well-known vascular dilator (41). Therefore when WSS is elevated, the vessel reacts to dilate and lower the WSS via the relationship in Eq. 4.7. Conversely, experiments in which WSS was decreased have demonstrated the proliferation of endothelial cells (42), as well as endothelial desquamation, greater monocyte attachment (43), and increased expression of vascular cell adhesion molecule I (VCAM-I) (44). Given these early signs of atherosclerosis development, such experiments are demonstrative of the relationship between atherogenesis and WSS.

Given that WSS is derived from the rate of blood flow, PC MRI can be used to estimate WSS values (45, 46). Flow measurements from PC MRI can be used as the boundary conditions in a computational fluid dynamics (CFD) model of the vasculature, which can provide good estimates of WSS given the very high spatial resolution of CFD (47, 48). The drawback of this approach is the difficulty of creating realistic CFD simulations with time varying geometries and spatially varying parameters. WSS has also been estimated from PC MR images directly (49, 50). WSS measurements via PC MRI are computed typically by assuming a blood viscosity of 4.0 cP·s and computing the cross product of the velocity vector and the inward normal vector for a voxel on the vessel wall, given by

$$WSS = \mu \frac{\partial v}{\partial n} \qquad \text{Eq. 4.8}$$

where v is the velocity vector and n is the inward normal vector.

4.3 Pulse Wave Velocity

Pulse wave velocity (PWV) is defined as the rate at which the systolic bolus of blood, pumped from the heart, traverses the vasculature. Mathematically PWV is computed via the Moens-Korteweg equation,

$$PWV = \sqrt{\frac{E \cdot h}{2r\rho}} \qquad \text{Eq. 4.9}$$

where E is the elastic modulus of the vessel, h is vessel wall thickness, r is the vessel radius, and ρ is the blood density. PWV is a biomarker of arterial stiffness. As atherosclerosis progresses vessel wall thickness, h, increases and vessel radius, r, decreases. These changes in vessel wall thickness and radius both serve to increase the PWV as atherosclerosis develops (Eq. 4.9).

Furthermore, PWV increases independently with both age and blood pressure (51). PWV is potentially a very strong early biomarker of atherosclerosis, given that arterial stiffness first increases without changes in vascular geometry—via the Glagov phenomenon (10). Therefore, early changes in arterial stiffness are not reflected on angiographic imaging.

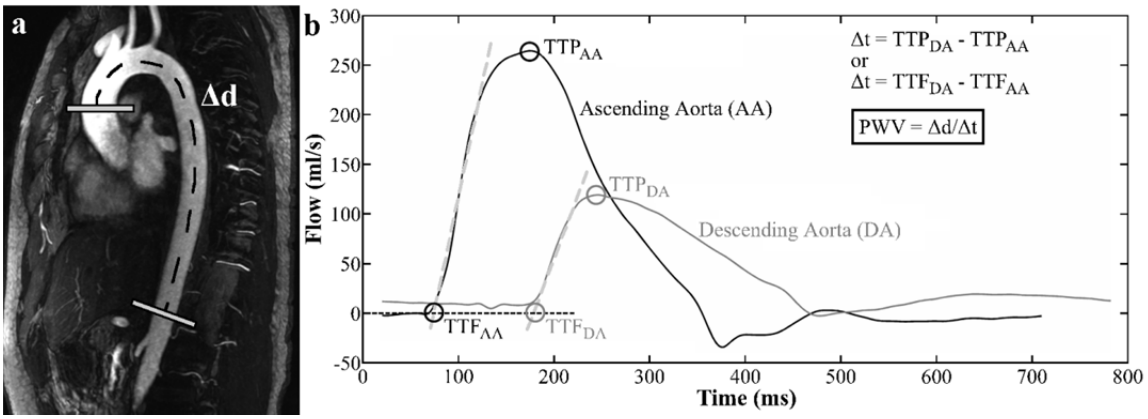

Figure 4.6 A contrast-enhanced angiogram (**a**) with representative planes in the ascending and descending aorta. Flow waveforms (**b**) from the two planes are shown with the time-to-foot (TTF) and time-to-peak (TTP) algorithms. The best fit linear lines along the upstroke were used to identify the foot of the waveforms. PWV is computed as $\Delta d/\Delta t$, where Δd is defined as the distance between the two planes along the vessel centerline, and Δt is defined as the temporal difference between two waveforms using, for example, the TTP or TTF algorithms.

PWV is measured clinically with applanation tonometry (52) and Doppler ultrasound (53) via the measurement of pressure waveforms in the carotid and femoral arteries. A number of studies have also employed PC MRI to measure PWV (54-57). Instead of measuring the elastic modulus, vessel wall thickness, vessel radius, and blood density to compute PWV (Eq. 4.9), PWV is often estimated by measuring the distance between two points and dividing this distance by the temporal difference between pressure or flow waveforms. Temporal differences between pressure or flow waveforms are computed with several algorithms, with time-to-foot (TTF) and time-to-peak (TTP) being the most common (Figure 4.6b). In applanation tonometry and Doppler ultrasound, distances are approximated by measuring the distances between the sternal

notch and the carotid and femoral arteries. A number of correction factors have been developed to improve this distance estimation (51). For PC MRI-based PWV measurements, distances are more accurately measured along vessel centerlines via angiographic MR images (Figure 4.6a). However, it should be noted that a recent ultrasound study was able to evaluate PWV regionally within the carotid artery alone (58), which was made feasible by the high temporal resolution of ultrasound and the ability to measure distance within the beam imaging width.

4.4 Other Hemodynamic Parameters

In addition to the quantification of PWV and WSS, PC MRI can be used to compute other hemodynamics parameters. For example oscillatory shear index (59, 60), pressure gradients (61-64), and turbulence (65-67) have been evaluated. While these parameters are promising, they are not explored further in this dissertation.

Chapter 5 Rapid Magnetic Resonance Imaging

This chapter discusses a number of algorithms and techniques for the acceleration of magnetic resonance imaging. This discussion includes an explanation of undersampling, which underlies all of the work proposed in this dissertation, as well as a number of other techniques, including parallel imaging, k-t BLAST/SENSE, HYPR, and McKinnon-Bates. In later chapters several of these approaches will be expounded in terms of phase contrast imaging.

5.1 Undersampling

In traditional Fourier-encoded imaging, scan time is directly proportional to the number of phase-encoding lines, N_y. One means of reducing imaging time is to reduce N_y; the act of omitting phase encoding lines is otherwise known as undersampling. However, this is problematic given that the spacing between lines, Δk_y, would double in the event that every other phase-encoding line is omitted. Doubling Δk_y will lead to a halving of the FOV in the y-direction, according to Eq. 3.17. Halving the FOV will lead to aliasing, or wrap-around, artifact (Figure 5.1). Wraparound artifacts often obscure essential regions of the image.

Undersampling in radial acquisitions is less problematic. Scan time is reduced in radial k-space sampling by reducing the number of acquired radial projections (Figure 5.2). The advantage of radial k-space sampling is that reducing the number of projections does not change the spacing, Δk, between points along any given direction. Therefore, via Eq. 3.16 and Eq. 3.17, the FOV does not change in a reconstructed image. Furthermore, $\Delta k_{x_{max}}$ and $\Delta k_{y_{max}}$ do not change as a result of undersampling, and therefore, the spatial resolution does not change in a

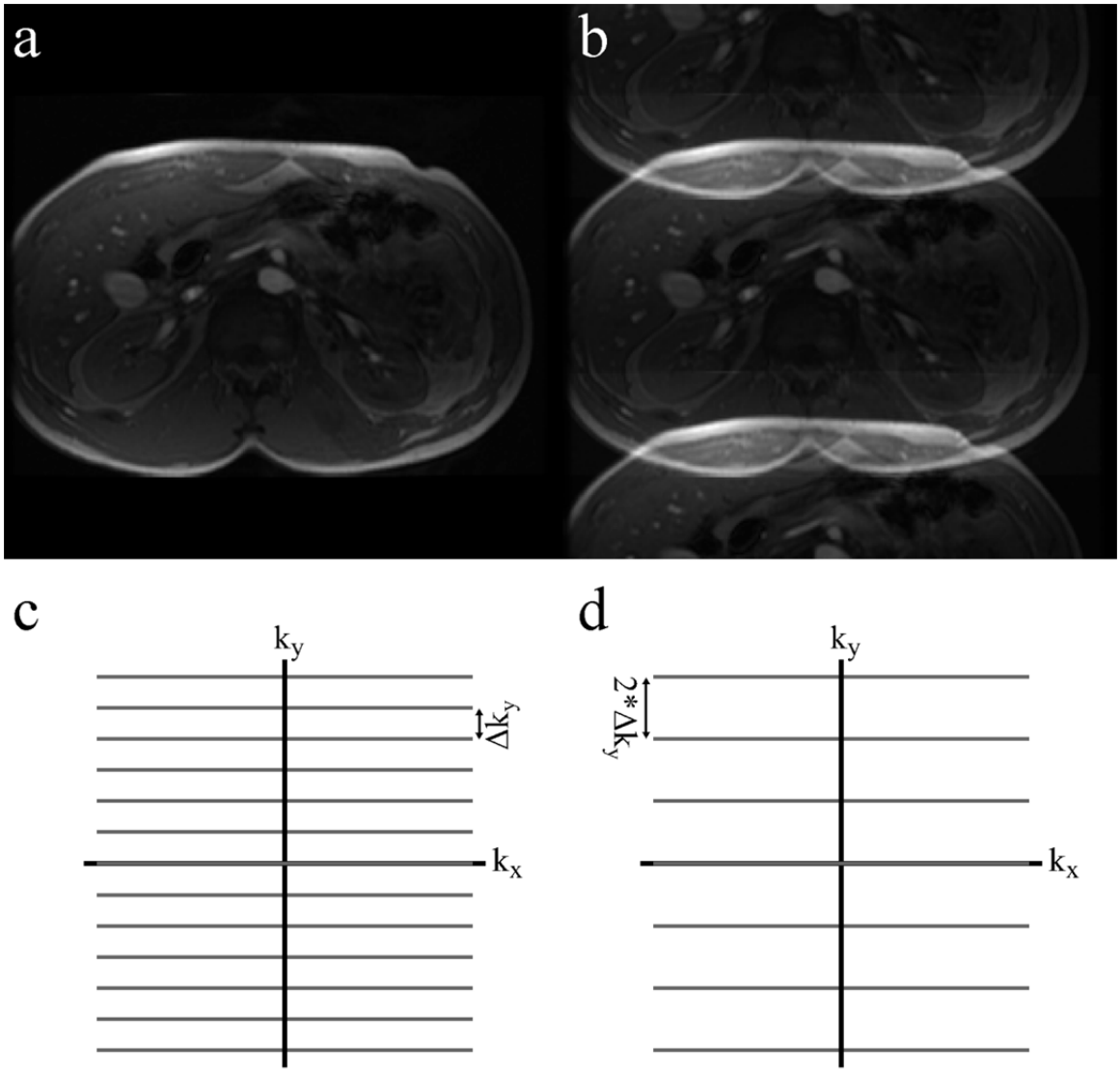

Figure 5.1 Image aliasing. When phase encoding lines are omitted in k-space, such as every other line as shown in **d**, the spacing between lines doubles, $2*\Delta k_y$, relative to a fully sampled k-space (**c**). Since $\Delta k_y = 1/FOV_y$, the FOV is halved in image space, leading to aliasing (wraparound artifact) (**b**) relative to a fully sampled image (**a**).

reconstructed image according to Eq. 3.18 and Eq. 3.19. However, the omission of radial projections leads to less sampling of the outer regions of k-space, which represent high spatial frequencies. This inadequate sampling leads to streak artifacts, which emanate from high signal voxels within an image because the edges of objects are not properly represented in the frequency (k-space) domain (Figure 5.2). However, such artifacts can be acceptable in high

contrast images, especially when the images are sparse and there are few objects/high signal areas from which streak artifacts can emanate. As a result, PC imaging is particularly well-suited to radial acquisitions due to the inherent sparsity in the (phase difference) images after the subtraction of signal from static tissues.

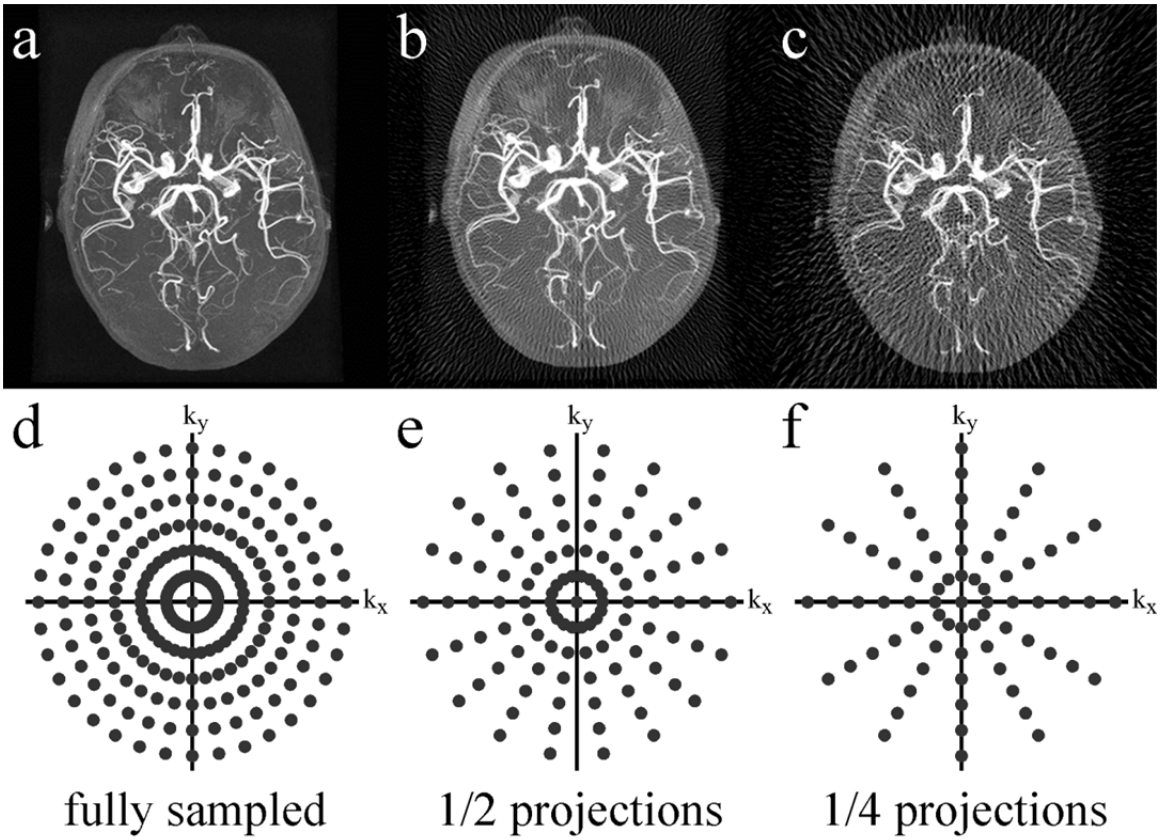

Figure 5.2 Radial undersampling. From a fully sampled k-space (**d**), a reconstructed image has no appreciable artifacts (**a**). As radial projections are omitted to reduce imaging time (**e**,**f**), streak artifacts appear in the images (**b**,**c**). The number of projections is inversely related to the number of streak artifacts. Images courtesy of Frank Korosec, PhD.

5.2 Parallel Imaging

Phased array coils are typically used to improve the signal-to-noise ratio via the use of multiple receiver coils that are smaller and closer to the imaged region than the traditional birdcage-type head and body coils. Decreasing the coil size results in a reduction in the spatial

sensitivity of each coil. Nevertheless, this is advantageous because the noise amplitude detected from smaller coils is also mitigated. When a number of these small coils are combined into a phased array, the overall signal is approximately equivalent to a single coil of equal size, but the noise is significantly reduced. Parallel imaging (PI) employs phased array coils to accelerate image acquisition by exploiting data redundancies among the coils.

PI omits phase-encoding lines in k-space to accelerate image acquisition. The factor by which phase-encoding lines are omitted in k-space is called the reduction/acceleration factor, *R*. To avoid image aliasing (Figure 5.1), the sensitivity of each phased array element is used to compensate for the aliasing. The two major methods for PI are k-space- or image-based approaches, originally introduced as SMASH (68) (simultaneous acquisition of spatial harmonics) and SENSE (69) (sensitivity encoding), respectively. In SMASH, spatial dependences of coil sensitivities are used to approximate missing phase-encoding lines in k-space. This k-space based approach has been largely replaced by GRAPPA-type processing (70). In SENSE, k-space data from each individual coil are reconstructed with a Fourier transform. These individual coil images are aliased; however, the individual coil images can be combined via matrix inversion by adding information on the coil sensitivities. PI techniques can significantly reduce scan time, but at the expense of a lower signal-to-noise ratio not only from the reduction in scan time but also by the mathematical process.

One PI method particularly well-suited for radial acquisition is known as PILS (71) (parallel imaging with localized sensitivities). PILS is similar to SENSE, in that reconstructed coil images are added together. Coil images are placed together based on both the coil sensitivity weighting as well as coil separation distances. PILS is optimally used when coil sensitivities do

not overlap, a condition that is difficult to achieve in practice without signal drops in the imaged object. However, PILS can be used to contain streak artifacts to the local coil regions instead of extending over the complete FOV.

5.3 k-t BLAST/SENSE

k-t BLAST (broad-use linear acquisition speed-up technique) and k-t SENSE make use of redundancy in k-space and in a time series of images (72). k-t BLAST is designed for a single receiver coil, whereas k-t SENSE is designed for use with phased-array coils, similar to SENSE in section **5.2 Parallel Imaging**.

There is substantial redundancy in most MR images, especially over time for dynamic image series. For a column of voxels through the heart in x-t space, there are noticeable but minimal changes over time (Figure 5.3b). An inverse Fourier transform of the x-t space provides a frequency representation of the data in x-f space (Figure 5.3c). x-f space is relatively sparse, which reflects the extent to which voxels change over the time series of data. Note that the example in Figure 5.3 is a "worst-case scenario," given the motion of the heart. Essentially all other portions of the body would have an even sparser x-f space.

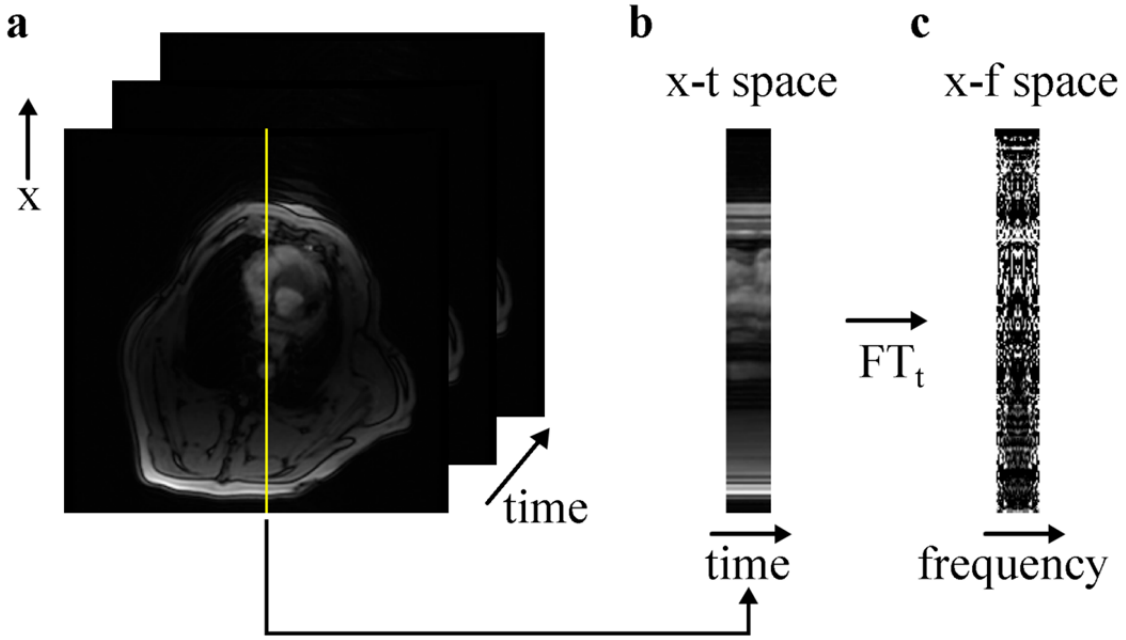

Figure 5.3 Signal over time and in frequency for a column of voxels. For the column defined by the yellow line (**a**), there is some degree of motion and signal change over time (**b**). The Fourier transform along the temporal dimension (FT_t) provides a frequency representation of the signal over time (**c**). Figure adapted from Kozerke's and Tsao's review of accelerated imaging techniques (73).

k-t BLAST and k-t SENSE undersample the phase encoding lines and increment which phase-encoding lines are omitted through the time series of data. This method of undersampling effectively undersamples in x-t space (Figure 5.4). Undersampling leads to aliasing (Figure 5.1). The aliasing is resolved with the use of a low-resolution training data set, which provides an estimate of the actual object (73). k-t SENSE specifically incorporates coil sensitivities as well to provide either better reconstructions from the aliased data or equivalent reconstructions—to k-t BLAST—with greater undersampling factors.

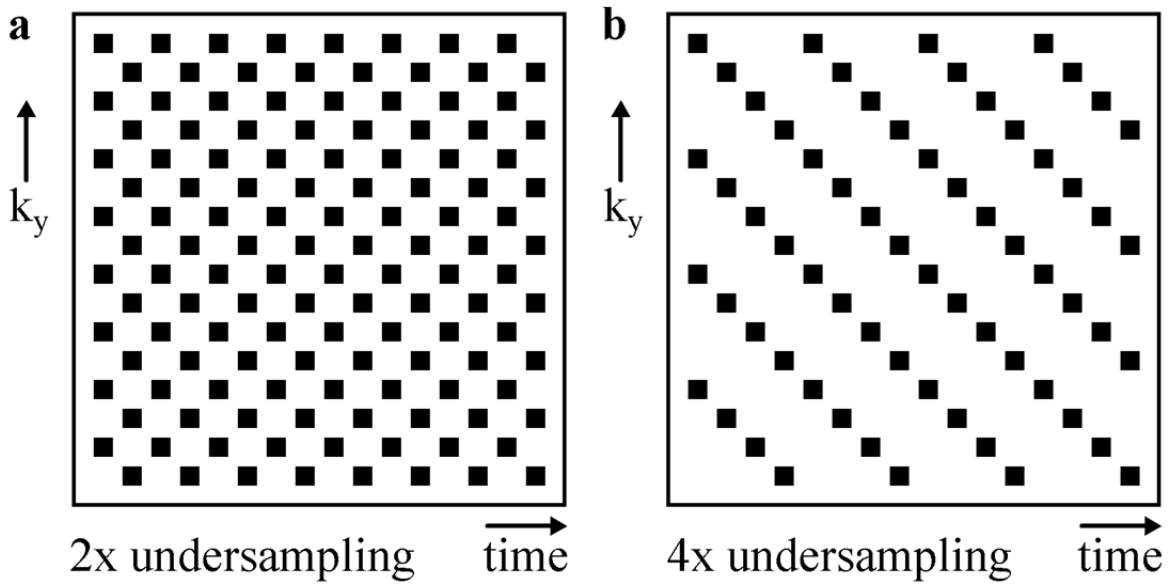

Figure 5.4 Undersampling in x-t space by factors of 2x and 4x. Figure adapted from Kozerke's and Tsao's review of accelerated imaging techniques (73).

5.4 HYPR

The HYPR (HighlY constrained back-Projection) algorithm (74) was developed for radial acquisitions in which high spatial and temporal resolution could be maintained without significant undersampling artifacts (Figure 5.2) and while maintaining high SNR. The basic HYPR algorithm (Figure 5.5) is employed on a time series of k-space data that is radially undersampled. Radial projections acquired in k-space are interleaved from one time frame to another. The projections from all time frames are added together to reconstruct a temporally averaged high resolution composite image. (Note that at this processing stage individual time frames are not reconstructed; reconstruction of these images is feasible, depending on the number of projections, but substantial streak artifacts would be present depending on the degree of undersampling.)

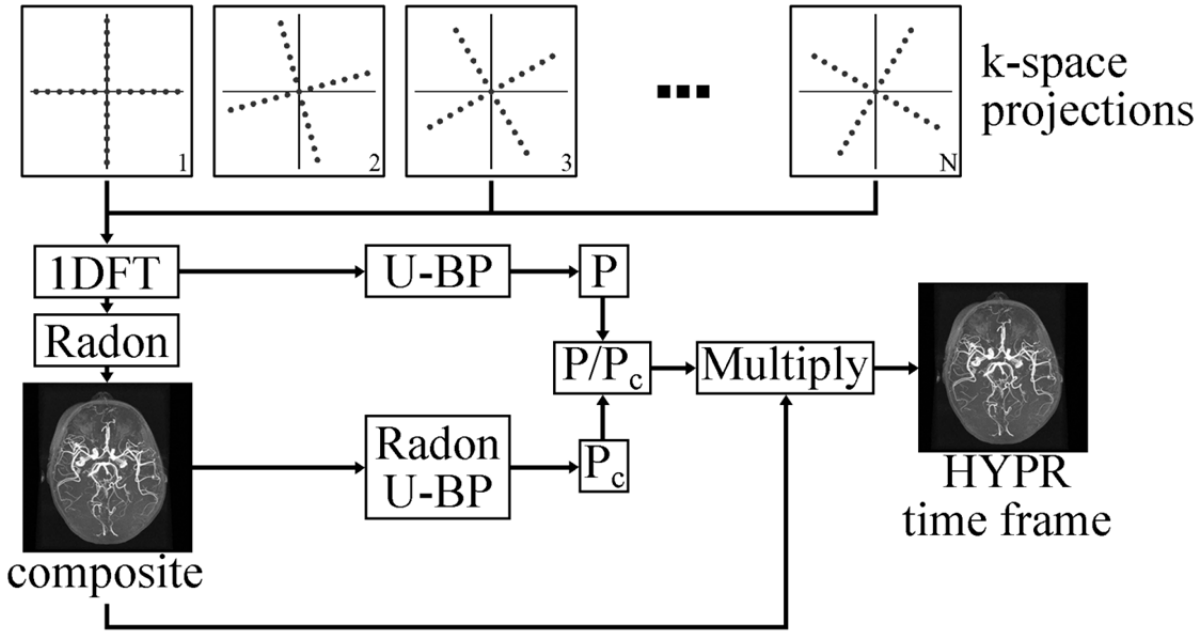

Figure 5.5 HYPR reconstruction algorithm. Highly undersampled images (in k-space) are acquired with a radial acquisition, in which few projections are acquired per time frame. The projections from all time frames are combined to form a temporally averaged high resolution composite image. The original k-space data for each time frame, along with the composite image, are backprojected (U-BP [unfiltered backprojection]) and divided (P/P_c). The result of this division is then multiplied by the composite image to produce HYPR time frames. 1DFT = one-dimensional Fourier transform

After the creation of a composite image, an image space profile (P_c [Figure 5.5]) is created from the composite image with the use of a Radon transform and unfiltered backprojection. Unfiltered backprojection is also performed on each of the original time frames in k-space to create an image space profile, P (Figure 5.5). For each time frame, P is divided by P_c, and then multiplied by the composite image. This operation leads to an individual HYPR time frame. The highly undersampled k-space time frames provide high temporal resolution, while the multiplication by the composite image provides high spatial resolution. The HYPR algorithm is not restricted to the creation of a single composite image. Depending on the temporal dynamics of the imaging series, as well as the degree of undersampling, a sliding window approach can be used to create a series of composite images with less temporal averaging.

The number of projections needed in the undersampled k-space time series is dependent on the sparsity of the imaging volume. Since angiography data tend to be sparse, HYPR is particularly well-suited for the reconstruction of an undersampled time series of angiographic data. However, the HYPR algorithm to date does not function with PC data, given that phase difference images have positive and negative values, which would tend to cancel in the formation of a composite image. The magnitude constraint present in the original HYPR algorithm is challenging to overcome with phase sensitive processing. While the HYPR algorithm is most directly applicable to radial acquisitions, any k-space trajectory can be used via the regridding of k-space data into projections.

A number of variations on the HYPR algorithm have been developed, including a local reconstruction approach (HYPR LR) (75), an iterative approach (I-HYPR) (76), a conjugate gradient approach (CG-HYPR) (77), and an approach based on Cartesian sampling (HYCR) (78). However, these methods are outside the scope of this dissertation.

5.5 McKinnon-Bates

The original McKinnon-Bates (M-B) algorithm (79) was developed for the evaluation of the heart in computed tomography (CT). The problem with CT imaging, at the time, was that very few x-ray projections could be acquired per phase of the cardiac cycle due to cardiac motion. Image quality was hampered by the high degree of undersampling inherent in the limited technology of the time.

The M-B algorithm estimates stationary regions of the image series by creating a temporally averaged composite image from all of the projections. From the composite image, the

static background is identified manually. The fully sampled projection representation of the background is then subtracted from the original undersampled data. This subtraction provides projection data that represent only the dynamically changing object of interest. Reconstruction of these data produces an image series with an object of interest, for example the heart, without the undersampling (streak) artifacts emanating from the static background. The M-B algorithm will be explored further in **Chapter 11 Phase Contrast** with Highly Constrained Backprojection and McKinnon-Bates Sparsification.

Chapter 6 Validation of Radial Undersampled 2D Phase Contrast Flow Measurements

PURPOSE: To assess the accuracy of flow measurements *in vitro* and *in vivo* during scan times shorter than a breath hold using a 2D cine phase contrast (PC) undersampled radial acquisition method, which may be useful for measuring flow, especially in vessels subject to motion during respiration.

MATERIALS AND METHODS: For *in vitro* assessment, a flow phantom was imaged at various flow rates and undersampling factors. For *in vivo* assessment, five normal subjects were imaged and the flow rate in the aorta was compared with the sum of the flow rates in the iliac arteries.

RESULTS: For results *in vitro*, the accuracy of flow measurements was maintained with scan times as low as 13 – 17 seconds. For results *in vivo*, scans acquired in less than 25 seconds provided flow measurements in the aorta that corresponded well to the sum of flow measurements in the iliac arteries.

CONCLUSION: The undersampled radial acquisition cine PC technique provided accurate flow measurements in a flow phantom and in healthy human volunteers in scan times less than a typical breath hold.

6.1 Introduction

Phase contrast (PC) methods permit the *in vivo* measurement of blood velocities (23, 32, 33). With a slice oriented orthogonal to a vessel of interest, volume flow rate can be computed for through-plane flow (31, 80). If the MR acquisition is synchronized with the heartbeat, volume flow rates can be determined throughout the cardiac cycle (27, 81). Such quantitative measures can assist in the diagnosis of vascular diseases.

For example, Schoenberg *et al*. showed that MR PC flow measurements and the shape of the flow waveform throughout the cardiac cycle could be used to identify the hemodynamic significance of vascular pathologies in the renal arteries (82). They concluded, however, that a higher temporal resolution than that achievable with commercially-available MR flow measurement methods was needed to provide a more accurate demonstration of the flow waveform. Prince *et al.* sought to use non-cine 3D phase contrast magnetic resonance angiography to assess the severity of stenoses and found a marked correlation between hemodynamic significance and signal dephasing (83). However, phase contrast used in this way provides a qualitative approach to assessing hemodynamic significance. Finally, segmented EPI has been used to increase temporal resolution, but this technique uses multi-echo readout trains, which lead to susceptibility-induced signal loss and distortions (84).

The accurate measurement of flow requires high spatial resolution for a true depiction of the cross-sectional area of the vessel of interest (29). In addition, a high temporal resolution is required for an accurate representation of the varying shape of a flow waveform throughout the cardiac cycle. Increased spatial resolution is typically obtained at the expense of lower temporal

resolution or longer scan time. Similarly, increased temporal resolution typically comes at the expense of decreased spatial resolution or longer scan time.

In scanning those regions of the body that are affected by respiratory motion, an MR scan must accommodate the motion that can occur. Most frequently, such examinations are performed during a single breath hold in order to prevent motion-induced artifacts and blurring. Scans in these regions are limited to the duration of a patient's breath hold (usually less than 20 – 30 seconds), and therefore, spatial resolution, temporal resolution, or both, are typically compromised. This holds particularly true for PC imaging, as one reference data set must be acquired in addition to the data sets required for each flow encoding direction. An alternative method to breath hold imaging uses a navigator echo for a free-breathing acquisition (85).

Barger *et al.* developed a non-cine PC acquisition using azimuthally undersampled projections, or radial lines in k-space, that provides higher spatial resolution per unit time than a traditional spin-warp encoding technique (86). In high contrast environments, such as those found in phase contrast MRA, resolution does not firmly depend on the number of radial lines sampled. For a given scan time, images with better spatial and/or temporal resolution can be acquired using PC PR (Phase Contrast with undersampled PRojections). Alternatively, PC PR can be used to reduce the total scan time without decreasing the spatial and/or temporal resolution. Azimuthal undersampling does not decrease the spatial resolution but it does introduce streak artifacts (87) that, in most cases, are tolerable when the number of signal generating objects in the FOV is limited and the SNR from these objects is high. The intensity of streak artifacts increases with the amount of undersampling (88).

We have developed a cardiac-triggered cine version of PC PR to rapidly acquire a high spatial and temporal resolution 2D data set with the goal of obtaining accurate measurements of flow waveforms in the renal arteries of patients with renal artery stenosis. The purpose of this study was to validate PC PR by assessing the accuracy of controlled *in vitro* flow measurements and determining the feasibility of obtaining accurate flow measurements in human subjects. Although our ultimate goal is to measure flow in the renal arteries, we have evaluated PC PR *in vivo* by comparing the flow rate in the aorta to the sum of flow rates in the iliac arteries, since the sum of flow rates in the iliac arteries should equal the flow rate in the aorta.

6.2 Materials and Methods

6.2.1 in vitro Studies

The undersampled and cardiac-triggered cine PC PR sequence was implemented on a 1.5 T MR scanner (Signa Excite, GE Healthcare, Milwaukee, WI). Projection pairs with and without bipolar gradients were acquired sequentially in time at the identical projection angle for velocity encoding. Data acquisition was segmented such that 1 or 2 projections, or radial k-space lines, were acquired per segment (vps). One segment was acquired per simulated cardiac cycle. Each segment was repeatedly acquired as many times as possible within each simulated cardiac cycle. The data were reconstructed into images representing information at different time points (phases or frames) throughout the simulated cardiac cycle.

For *in vitro* assessment, the PC PR method was used to image blood mimicking fluid that was being pumped through a 0.635 cm inner diameter tube by a computer-controlled flow pump (100060 UHDC Flow System, R.G. Shelley LTD., Toronto, Canada) with an accuracy of ±1 %

as quoted by the pump manufacturer. A four-element phased array torso coil (GE Healthcare, Milwaukee, WI) was employed for through-plane flow measurements and the following imaging parameters were used: TR/TE = 6.4/3.0 ms, BW = ± 31.25 kHz, FOV = 24 – 34 cm, slice thickness = 5 mm, flip angle = 30°, and 256 data samples along each projection. Data were acquired during constant flow and sinusoidal flow; the former was triggered at 60 beats per minute (BPM) using a waveform generator (M310 ECG Simulator, Fogg System Company, Inc., Denver, Colorado) and the latter was triggered at 60 BPM using a signal generated by the pump. Scans were performed with 8, 16, 32, 64, 128, and 256 projections for constant and sinusoidal flow rates of 1 – 10 ml/s in 1 ml/s intervals for scan times ranging from 4 to 120 seconds. Sinusoidal flow waveforms were designed to have a DC offset corresponding to each average flow rate, and the flow varied ±1 ml/s about each average flow rate. Scans were repeated three times at each flow rate and with each of the specified number of projections. Images were reconstructed offline. The projection data were regridded using a Kaiser-Bessel interpolation kernel of ± 2 pixels. The regridded data were then inverse Fourier transformed and phase difference and magnitude images were produced. The phase difference data from the four coil elements were combined using the hybrid method described by Bernstein *et al.* (89)

The images were subsequently analyzed with a commercial flow analysis package (CV Flow, Medis, The Netherlands). Regions of interest (ROIs) were drawn on each of the magnitude images and were automatically copied onto the corresponding phase difference images by the software. ROIs were propagated across all phases. Flow data were generated by the software and recorded for analysis.

Finally, the data were summarized with Bland-Altman analysis (90), comparing the known flow rate of the pump to the measured flow rate from the images acquired with the PC PR method. The data used in the analysis were averages of flow measurements acquired from the three repeated scans and all of the flow measurements acquired throughout the simulated cardiac cycle.

6.2.2 Human in vivo Studies

Evaluations *in vivo* were performed on five normal subjects (3 males, 2 females, mean age = 40 ± 15 years) with parameters similar to those described above. Informed consent was obtained prior to each examination. Images were acquired during breath hold intervals as long as 25 seconds (64 projections) and as short as 4 seconds (8 projections). In each of the human subjects three data sets were acquired, one oriented orthogonal to the flow in the aorta, a second oriented orthogonal to the flow in the left iliac artery, and a third oriented orthogonal to the flow in the right iliac artery. The three scans were performed in each subject using 64, 32, 16, and 8 projections and repeated with 1 and 2 views per segment (vps). Images were also acquired with a traditional cardiac-gated, segmented spin-warp PC acquisition method with TR/TE = 9.9/4.4 ms, 2 vps, BW = ± 31.25 kHz, flip angle = 45°, 28 – 35 seconds per scan using 128 phase encoding values, and ½ FOV. Data were acquired using a four-element phased array torso coil. The scan time of the spin-warp acquisition with 1 vps was prohibitively long to be completed during a breath hold, and therefore, not attempted. Data were tabulated to compare the flow rate in the aorta to the sum of the flow rates in the iliac arteries. The *p*-values from a paired t-test with significance level of 0.05 were computed from the tabulated data to compare flow measurements obtained from the PC PR and spin-warp acquisitions.

6.3 Results

6.3.1 in vitro Studies

Images of constant flow through the phantom (flow rates of 1 – 10 ml/s in 1 ml/s increments), acquired in 34 seconds using 64 projections, yielded flow measurements that were on average 2.35 % lower than the actual flow rates of the pump (Figure 6.1). Scans using other undersampling factors yielded average percent differences of: -1.97 % using 32 projections, -9.13 % using 16 projections, and -16.01 % using 8 projections (Table 6.1). For scans acquired in times longer than an average breath hold, the average percent difference was -1.89 % using 128 projections and -0.82 % using 256 projections (Table 6.1). Images of pulsatile flow through the phantom (average flow rates of 1 – 10 ml/s in 1 ml/s increments) yielded flow measurements averaging percent differences of: +0.45 % using 256 projections, +0.08 % using 128 projections, +1.09 % using 64 projections, +1.52 % using 32 projections, +6.57 % using 16 projections, and +13.47 % using 8 projections (Table 6.2). Images of pulsatile flow acquired with PC PR using 8, 16, 32, and 256 projections are shown in Figure 6.2a.

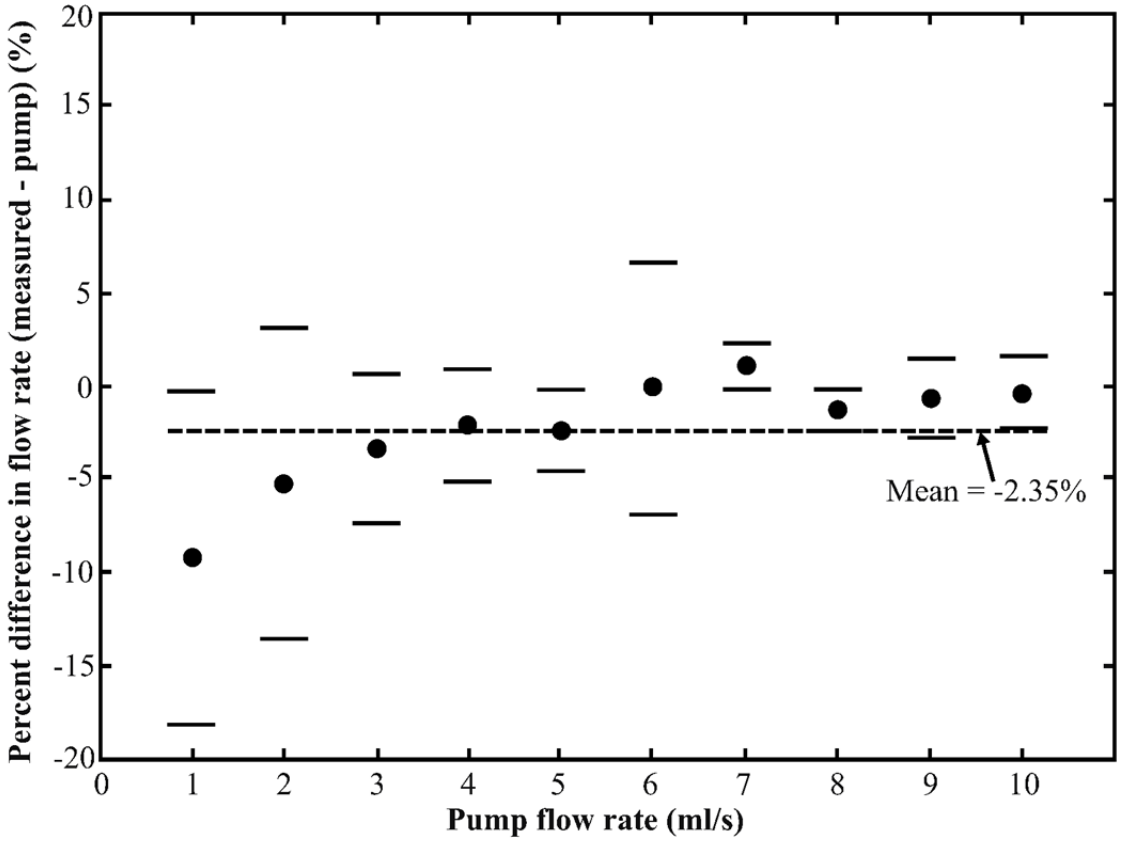

Figure 6.1 Bland-Altman analysis comparing known flow rates from a flow pump phantom and flow measured with PC-PR with 64 projections. The percent differences between the averaged measured flow rates and the pump's flow rates are shown on the abscissa. Three scans were performed at each flow rate for averaging and error calculations. Error bars are shown (mean ± 2 SD). The mean percent difference across all flow rates was -2.35%.

Table 6.1 Constant Flow

Average flow rate (ml/s)	% Difference ± 2 SD (ml/s) for various numbers of projections					
	$N_p = 256$	$N_p = 128$	$N_p = 64$	$N_p = 32$	$N_p = 16$	$N_p = 8$
1	-0.68 ± 3.12	-7.53 ± 8.26	-9.20 ± 8.91	-8.07 ± 11.04	-34.35 ± 11.67	-39.47 ± 13.81
2	-0.91 ± 2.12	-4.33 ± 4.77	-5.20 ± 8.32	-4.40 ± 5.20	-17.98 ± 5.94	-26.33 ± 5.09
3	-2.09 ± 1.20	-1.44 ± 2.85	-3.36 ± 3.97	-3.22 ± 1.89	-13.93 ± 9.34	-19.02 ± 1.90
4	-1.80 ± 1.57	-2.57 ± 3.13	-2.10 ± 2.95	-0.17 ± 0.31	-6.93 ± 7.13	-13.71 ± 4.05
5	-1.05 ± 2.49	-3.96 ± 1.32	-2.37 ± 2.14	-0.64 ± 1.29	-7.29 ± 6.06	-13.66 ± 1.79
6	-1.12 ± 2.50	-2.24 ± 3.04	-0.10 ± 6.74	-0.44 ± 1.24	-4.58 ± 5.84	-11.13 ± 6.89
7	-0.70 ± 1.69	+0.15 ± 1.03	+1.07 ± 1.21	-0.20± 0.47	-1.92 ± 8.66	-13.46 ± 9.70
8	+0.29 ± 1.93	+1.13 ± 1.06	-1.28 ± 1.15	-0.67 ± 1.15	-1.66 ± 2.20	-8.25 ± 3.45
9	-0.13 ± 0.53	+1.10 ± 1.97	-0.64 ± 2.06	-1.48 ± 2.46	-1.82 ± 4.25	-7.46 ± 2.80
10	-0.04 ± 0.71	+0.81 ± 1.48	-0.36 ± 1.91	-0.37 ± 1.40	-0.83 ± 0.97	-7.60 ± 6.50

* Average percent differences between the average measured flow rates calculated using images acquired with PC-PR and the known flow rate of the pump.
N_p = number of projections, SD = standard deviation

Table 6.2 Pulsatile Flow

Average flow rate (ml/s)	% Difference ± 2 SD (ml/s) for various numbers of projections					
	$N_p = 256$	$N_p = 128$	$N_p = 64$	$N_p = 32$	$N_p = 16$	$N_p = 8$
1	+1.41 ± 6.66	+0.27 ± 7.59	+4.67 ± 18.01	+6.60 ± 35.00	+26.01 ± 3.89	+49.10 ± 15.20
2	+0.95 ± 3.55	+0.71 ± 5.76	-2.71 ± 4.01	+5.20 ± 11.70	+13.01 ± 6.92	+11.55 ± 5.00
3	+0.61 ± 2.75	-0.12 ± 2.55	+1.25 ± 2.69	+0.68 ± 6.64	+5.07 ± 7.88	+14.40 ± 10.00
4	+0.92 ± 1.86	-0.09 ± 1.74	+1.14 ± 2.66	-2.28 ± 3.70	+5.77 ± 7.88	+22.28 ± 5.30
5	+0.04 ± 0.44	+0.10 ± 2.72	-0.40 ± 1.18	+0.84 ± 6.03	+9.84 ± 3.52	+13.44 ± 1.28
6	+0.11 ± 1.22	-0.18 ± 1.72	-0.36 ± 1.50	+1.60 ± 5.40	+1.36 ± 5.92	+1.97 ± 4.33
7	+0.20 ± 0.76	-0.24 ± 1.78	+0.39 ± 1.02	+1.01 ± 3.17	+1.49 ± 4.72	+3.99 ± 1.60
8	+0.22 ± 0.87	+0.81 ± 0.74	+0.09 ± 1.42	-0.33 ± 0.82	-0.74 ± 0.90	+6.20 ± 7.75
9	+0.37 ± 0.89	+0.19 ± 0.90	+0.62 ± 1.03	+0.70 ± 2.21	+1.81 ± 1.32	+6.01 ± 2.04
10	-0.31 ± 0.82	-0.64 ± 2.30	+0.82 ± 0.65	+1.12 ± 1.15	+2.04 ± 0.37	+5.76 ± 4.62

* Average percent differences between the average measured flow rates calculated using images acquired with PC-PR and the known flow rate of the pump.
N_p = number of projections, SD = standard deviation

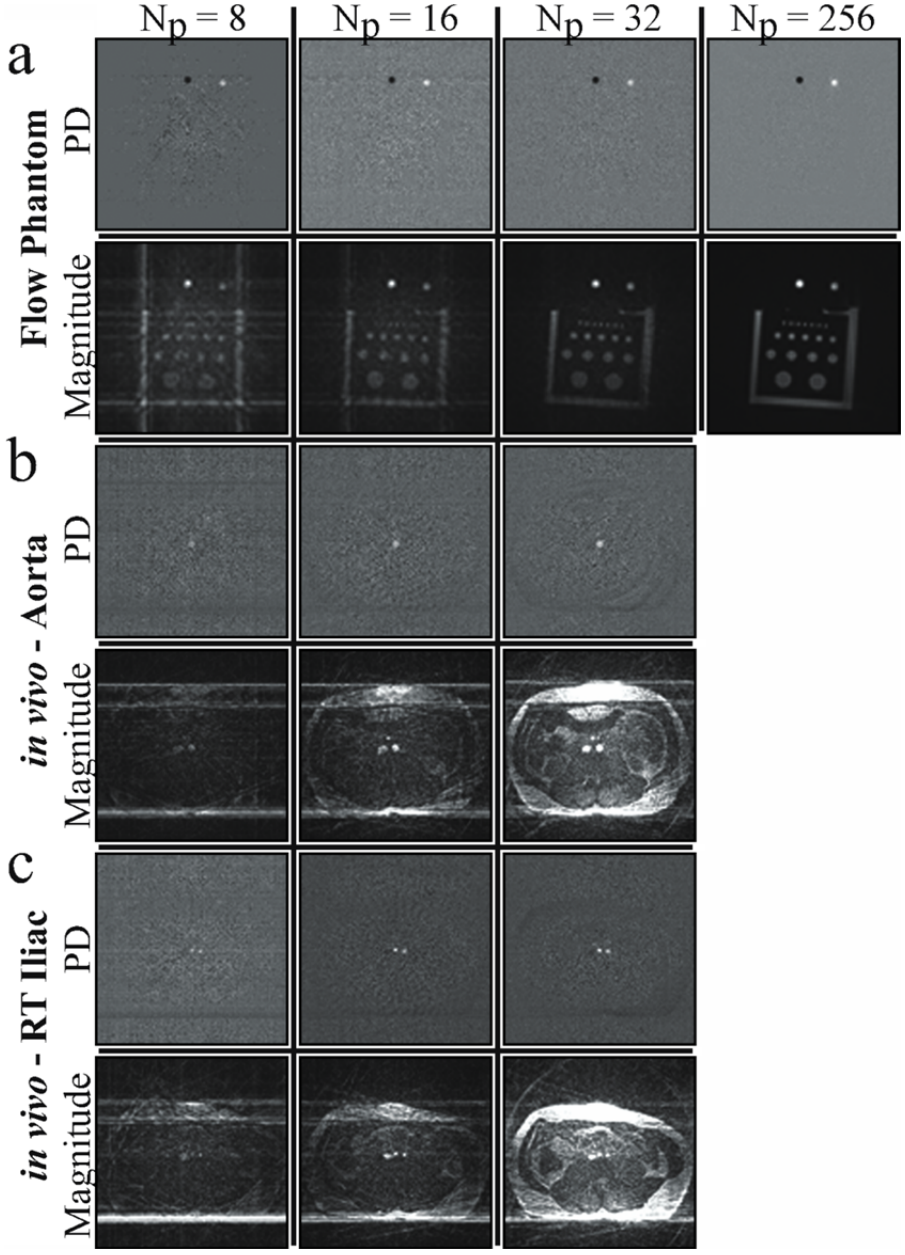

Figure 6.2 Phase difference and magnitude images acquired using PC-PR. **a.** Cross-sectional in vitro images showing one phase of pulsatile flow through the phantom acquired using 8, 16, 32, and 256 projections. (A resolution phantom used to simulate stationary tissue appears in the magnitude images). **b.** Cross-sectional in vivo images showing one phase of flow through the aorta acquired using 8, 16, and 32 projections. **c.** Cross-sectional images showing one phase of flow through the right iliac artery acquired using 8, 16, and 32 projections. All images were acquired using two vps. RT = right, PD = phase difference, N_p = number of projections.

6.3.2 Human in vivo Studies

Scans acquired using 32 projections and 1 vps, used to evaluate the potential benefit of improved temporal resolution, yielded flow measurements with accuracies similar to those obtained using PC PR with 2 vps. Average flow rates were calculated using all of the images acquired during the RR interval, with 40 – 45 phases collected with PC PR scans at 1 vps, 20-22 phases collected with PC PR scans at 2 vps, and 13 phases acquired with the traditional spin-warp acquisition at 2 vps. Images acquired *in vivo* using PC PR are shown in Figure 6.2b,c. Even though there are significant streak artifacts in the magnitude images emanating from high signal in the abdominal wall, these artifacts are not present in the phase difference images since the abdominal wall does not move during the acquisition. Note that the imaging time required for the spin-warp acquisition with 128 phase-encoding values, 2 vps, and a ½ FOV was the same time required for the PC PR acquisition using 32 projections, 1 vps, and a whole FOV. The SNR and CNR of images acquired using PC PR with 8 and 16 projections was inadequate and therefore no flow rates were measured when using these parameters *in vivo*.

The difference between the flow rate in the aorta and the summed flow rates in the iliac arteries was calculated for each method. A paired t-test revealed a significant difference (p-value < 0.05 [$p = 0.02$]) between measurements obtained using the PC PR acquisition with 32 projections and 1 vps and the spin-warp method acquired using 128 phase encoding values and 2 vps. Similarly a significant difference (p-value < 0.05 [$p = 0.0003$]) was determined between measurements obtained using the PC PR acquisition with 64 projections and 2 vps and the spin-warp method acquired using 128 phase encoding values and 2 vps. Finally, a p-value > 0.05 ($p = 0.72$) was computed when pairing data from undersampled PC PR using 1 and 2 vps and

therefore no significant difference was established between using PC PR with 1 or 2 vps. Figure 6.3 shows the results of these paired t-tests along with a bar graph showing the mean difference between the flow rate in the aorta and the summed flow rates in the iliac arteries for the three acquisition methods.

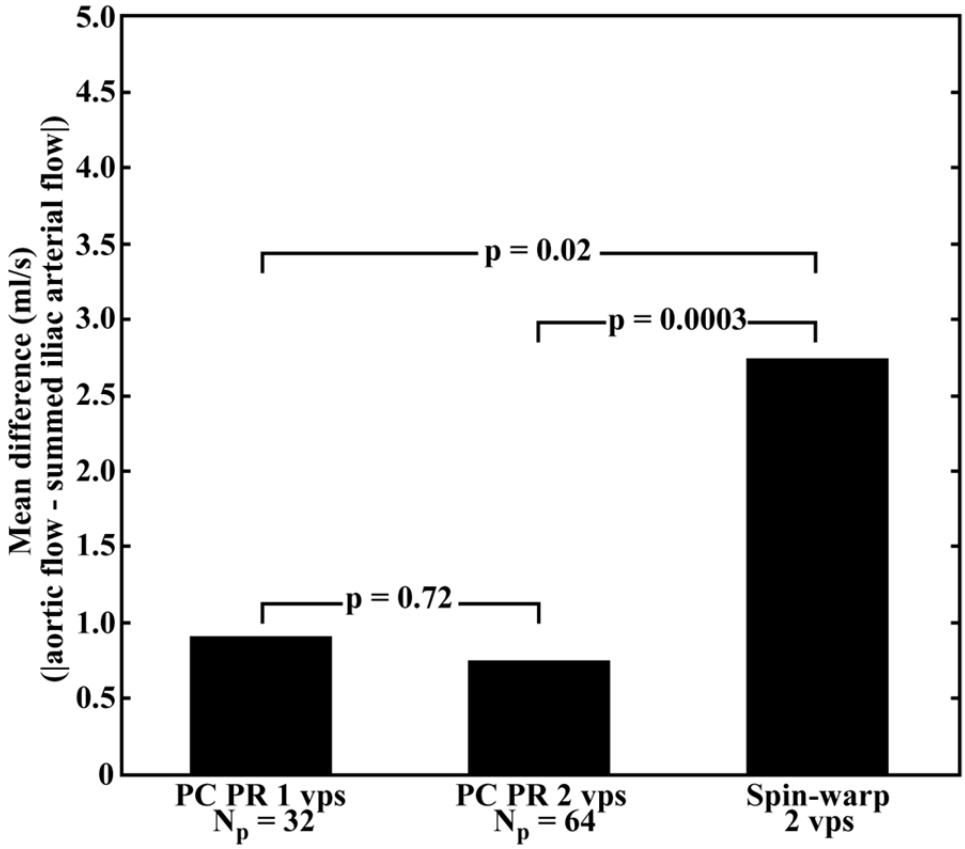

Figure 6.3 Mean difference in flow rates between aortic flow and the summed flow rates in the right and left iliac arteries as measured from PC-PR scans acquired with one and two vps, along with the mean difference in measurements obtained using a cardiac-gated spin-warp PC acquisition with two vps. p-values obtained using a paired Student's t-test with a significance level of 0.05 are shown to compare the differences between each method.

6.4 Discussion

Maximum average breath holds for patients are about 30 seconds in duration. PC PR results *in vitro* showed accurate flow rates obtained at scan times as short as 13 – 17 seconds with an acquisition using 32 projections and 2 vps, demonstrating that PC PR is a useful method

for obtaining accurate flow measurements even in an individual with limited breath holding ability. With individuals who can hold their breath for 30 seconds or longer, PC PR provides the option to reduce streak artifacts by acquiring 64 projections and 2 vps or improving temporal resolution by acquiring 32 projections and 1 vps. Therefore, the PC PR acquisition is useful for reducing scan time without diminishing the integrity of flow measurements and may be particularly useful for imaging individuals who cannot hold their breath for an extended period of time.

Overall, *in vitro* flow measurements obtained using the PC PR acquisition method were accurate using scans acquired with as few as 32 projections. In fact, the magnitude of the error in the flow measurements was consistently within a few tenths of one ml/s, independent of the average flow rate. As a result, as shown in Figure 6.1, the percent differences in the flow measurements obtained using flow rates less than or equal to 2 ml/s were larger than those obtained at higher flow rates. With a FOV of 24 – 34 cm and 256 data samples along each projection, a voxel dimension of 1.3 mm was obtained. When imaging smaller vessels, the spatial resolution can be improved by increasing the number of sample points along each projection to 512, resulting in only a minimum increase in scan time.

For *in vivo* flow measurements, there tended to be greater variation in flow measurements using the traditional spin-warp acquisition than the PC PR acquisition. Using the spin-warp method, the flow measurement from the aorta was different from the summed flow measurements from the two iliac arteries. For the PC PR acquisition using 32 and 64 projections, the flow rates were similar between the aorta and iliac arteries. Although the true flow rates in the vessels were unknown, the flow measurements acquired using PC PR provided more

consistent results. Low spatial resolution may account for the inaccurate flow measurements obtained using the spin-warp acquisition. It has been demonstrated that flow measurements will be inaccurate if an insufficient number of pixels spans the vessel of interest (29).

Paired t-tests demonstrated a significant difference in the *in vivo* measurements obtained using the spin-warp and the PC PR methods. On the contrary, paired t-test showed no significant difference between measurements obtained using the PC PR acquisition with 1 or 2 vps. Although these t-tests do not possess the ability to characterize the similarity of the measured flow rate in the aorta to the sum of the measured flow rates in the iliac arteries, this statistical test does show the marked difference between the results obtained using the PC PR method and the traditional spin-warp method. Although not indicated by the statistics, the PC PR acquisition with 1 vps provides improved temporal resolution versus the PC PR acquisition with 2 vps. This improved temporal resolution may be useful for detecting the peak flow during the RR interval. In comparing the spin-warp and PC PR acquisitions, the minimum repetition times were used in each examination. Since radial acquisitions do not need a phase-encoding gradient, the PC PR method had a lower minimum TR than the spin-warp acquisition.

In general, undersampled radial acquisitions, such as PC PR, are limited by streak artifacts introduced by undersampling. Although these artifacts tend to emanate out of and away from the vessels of interest, the aesthetics may render the image difficult to analyze. In addition, the definition of vessel boundaries in the magnitude images can become more challenging and affect the ROI placement. Vessels exhibiting pulsatility generate the most noticeable streak artifacts. The cardiac-gated acquisition used in this study mitigated some of the pulsatility effects, allowing for a further reduction in the number of projections than previously possible

(86). Streak artifacts are worse when fewer projections are used. By limiting the minimum number of projections to 32, the effects of streaks on adjacent vessels can be minimized. Nevertheless, reasonable results were obtained using 8 and 16 projections.

The PC PR method has shown promising results of accurate flow measurements in healthy volunteers. Although our ultimate application of the PC PR technique is for the renal arteries, we chose to use the aorta and iliac arteries as an intrinsic validation in humans. In an ongoing study, we are using the PC PR method to measure the flow rates in the renal arteries of swine during a forced breath hold to evaluate the feasibility of detecting the hemodynamic significance of renal artery stenoses.

In future studies, it may be advantageous to compare the PC PR technique with spin-warp PC methods that employ parallel imaging to achieve reductions in scan time of factors of 2 or 4. Furthermore, a non-Cartesian SENSE method has been implemented by Pruessmann *et al.* (91) Thus, future studies can include comparisons between PC PR and spin-warp PC methods that use parallel imaging.

In conclusion we have shown that the PC PR technique provides accurate and reproducible flow measurements *in vitro* in scan times less than an average breath hold. Results in healthy normal volunteers are promising. Depending on the ability of a patient to perform a breath hold, PC PR may be used to reduce the scan time without compromising the accuracy of flow measurements. PC PR may be useful in the future for renal flow imaging and improved assessment of the hemodynamic significance of stenoses.

Chapter 7 Aortic Pulse Wave Velocity Measurements with 4D Radial Undersampled Phase Contrast MRI

PURPOSE: To compare pulse wave velocity (PWV) measurements obtained from radially undersampled 4D phase-contrast MRI (PC MRI) with 2DPC measurements and to evaluate four PWV algorithms.

MATERIALS AND METHODS: PWV was computed from radially undersampled 3-dimensional, 3-directionally velocity-encoded PC MRI acquisitions performed on a 3T MR scanner in 18 volunteers. High temporal resolution 2DPC scans serving as a reference standard were available in 14 volunteers. Four PWV algorithms were tested: time-to-upstroke (TTU), time-to-peak (TTP), time-to-foot (TTF), and cross-correlation (XCorr). Bland-Altman analysis was used to determine inter- and intraobserver reproducibility and to compare differences between algorithms. Differences in age and PWV measurements were analyzed with Student's t-tests. The variability of age-corrected data was assessed with a Brown-Forsythe ANOVA test.

RESULTS: 2D (4.6 – 5.3 m/s) and 4D (3.8 – 4.8m/s) PWV results were in agreement with previously reported values in healthy subjects. Of the four PWV algorithms, the TTU, TTF, and XCorr algorithms gave similar and reliable results. Average biases of +0.30 m/s and -0.01 m/s were determined for intra- and interobserver variability, respectively. The Brown-Forsythe test revealed that no differences in variability could be found between 2D and 4D PWV measurements.

CONCLUSION: 4D PC MRI with radial undersampling provides reliable and reproducible measurements of PWV. TTU, TTF, and XCorr were the preferred PWV algorithms.

7.1 Introduction

Non-invasive techniques and biomarkers for evaluating the progression of atherosclerosis are of great interest for diagnosis and treatment monitoring. Pulse wave velocity (PWV), the rate at which the systolic wave of blood traverses the vasculature, is one such biomarker, as it is indirectly indicative of vascular stiffness. As arteries become stiffer with age or due to the development from subclinical to clinically apparent atherosclerosis, pulse wave velocity increases because of the loss of elastic recoil in the vessel (92). PWV increases independently with age and blood pressure (51) and is predictive of stroke irrespective of blood pressure (93).

PWV can be evaluated by detecting the temporal shift in blood flow waveforms at two or more locations in a vessel. Such measurements can be performed either invasively (pressure transducers) or non-invasively (applanation tonometry, ultrasound, MR imaging). Ultrasound-based carotid-to-femoral (artery) pulse wave velocity is a standard clinical procedure. However, distance measurements between these two locations are inaccurate and can lead to differences in PWV values of up to 30% (94).

Several MRI-based methods of measuring PWV have been reported in the literature. Most MR studies on PWV have been performed with the use of a 2D phase contrast (PC) acquisition with (unidirectional) through-plane velocity encoding (56). In its most basic form, two locations separated by a known distance are used (54, 55, 95, 96). Results rely on the temporal difference between the waveforms from the two locations and hence on the quality of

waveform sampling (97, 98). Examinations based on Fourier-velocity-encoded MRI produce time-velocity profiles with very high temporal resolution, on the order of 3.5 ms (99, 100). However, curvatures within the vasculature limit this approach, which is of particular concern since vessels tend to become tortuous with disease (101).

Recently, time-resolved 3-dimensional (so-called "4D") PC MRI approaches with volumetric coverage and velocity sensitivity in all three spatial directions have been presented (102, 103). A volumetric approach to PC MRI could help to overcome patient-specific and/or methodological limitations in 2D PWV measurements, such as potentially tedious slice placement in 2D approaches, especially in tortuous vessels. However, the achievable temporal resolution is inherently lower in 4D PC MRI because of the three-directional velocity encoding employed. A previously described Cartesian 4D PC MRI approach to PWV measurements provided thick-slab volumetric coverage with three-directional flow encoding. This technique has shown great potential, but at the expense of long scan times (15-20 minutes), compromised temporal resolution (>40 ms), and no validation against a clinical standard or other MRI-based measurement of PWV (98).

Several algorithms for computing PWV have been proposed in the literature (54, 57, 95, 98, 104, 105), such as the time-to-peak (TTP), time-to-foot (TTF), cross-correlation (XCorr), and second-derivative time-to-upstroke (TTU) algorithms. For studies comparing different algorithms, either the TTF (98) or the XCorr (104) algorithms were most reliable.

Phase contrast MRI with vastly undersampled isotropic projection reconstruction (PC VIPR) applies radial undersampling (87) to address a few of the technical limitations of the

Cartesian approach. It offers increased spatial and temporal resolution with large volume coverage in reduced scan times at the cost of acceptable artifacts (102, 106). The purpose of this prospective study was to compare PWV based on 4D velocity data acquired with PC VIPR to a high temporal resolution 2D approach as the reference standard. We hypothesized that the 4D technique would provide PWV measurements of equivalent magnitude and variability to the 2D approach. For both techniques, PWV calculations were based on previously reported algorithms, including the TTP, TTF, XCorr, and TTU algorithms. Secondary aims included the analysis of PWV differences between age groups (volunteers < and >35 years of age) and the determination of the most suitable algorithm(s) for calculating PWV.

7.2 Materials and Methods

7.2.1 Subjects

Twenty healthy volunteers were included in this HIPAA-compliant study. The study protocol was approved by the local institutional human subjects review board (IRB). Written informed consent was obtained from all subjects prior to inclusion. As part of the inclusion criteria, volunteers had to meet the following criteria: (1) No history of cardiovascular disease, (2) no history of smoking, (3) no cardiovascular medication, and (4) a body mass index (BMI) ≤ 30 kg/m^2. Data for two subjects were retrospectively excluded from the study for gating failures: one subject presented with a previously undiagnosed arrhythmia that led to erroneous ECG triggering. Similarly, the data for the second subject was invalid due to faulty ECG- and respiratory triggering. Furthermore, in four of the 18 2-dimensional PC MRI data sets, the cardiac trigger was sufficiently delayed such that the systolic upstroke of the flow waveform was never sampled. These four 2D data sets were excluded from the study. All comparisons between

2D and 4D data used the remaining 14 subjects (7 men, 7 women, ages 22 – 59 years, mean age (± 1 SD): 34.0 ± 13.5 years). In analyses performed on 4D data alone, data were used from all eighteen healthy volunteers (9 men, 9 women, ages 22 – 60 years, mean age (± 1 SD): 38.4 ± 14.8 years; mean BMI: 25.6 ± 3.5 kg/m^2).

7.2.2 MR Imaging

4D PC VIPR data were acquired on a 3T clinical MR scanner (MR750, GE Healthcare, Waukesha, WI) using a 32-channel torso coil (NeoCoil, Pewaukee, WI). A dual-echo 5-point velocity encoded sequence with retrospective ECG-gating was used (34). Typical scan parameters were: V_{enc} = 150 cm/s, TR/TE = 6.4-6.7ms/2.2ms, flip angle = 20-22º, bandwidth = 488.3 Hertz/pixel, readout = 256 samples, resulting in 1.25 mm^3 isotropic spatial resolution. The acquisition was conducted with an axial excitation that provided an imaging volume of 32 x 32 x 22 cm^3 with selective excitation in the superior-to-inferior direction. Respiratory gating with a 50% acceptance window that continuously adapts to the expiration position was used. The PC VIPR scan time was on the order of 11.5 minutes. During post-processing, time frames were reconstructed with temporal filtering in the RR-cycle, similar to view sharing in Cartesian acquisitions; this reconstruction provided time frames of 32 – 33.5 ms duration (107, 108). This temporal filter provides a temporal window equal to 5*TR (32 – 33.5 ms) in the lower frequency regions of k-space and widens for higher spatial frequencies to a maximum of 25*TR (160 – 167.5 ms) in the outer regions of k-space. Depending on each individual's heart rate (range: 49 – 72 bpm; mean (± 1 SD): 55.5 ± 6.5 bpm), data were reconstructed to 30.3 ± 3.6 time frames/cardiac cycle.

A commercial 2D PC sequence with prospective ECG-gating was applied in four scan planes placed orthogonal to the main flow direction in the ascending aorta, aortic arch, and in the proximal and supra-diaphragmatic descending aorta. Scan parameters included: V_{enc} = 150 cm/s, TR/TE = 5.2ms/3.0ms, flip angle = 30º, matrix size 256 x 256 pixels, slice thickness = 7 mm, in-plane spatial resolution = 1.6 x 1.6 mm^2, and 54.3 ± 21.2 time frames, temporal resolution:

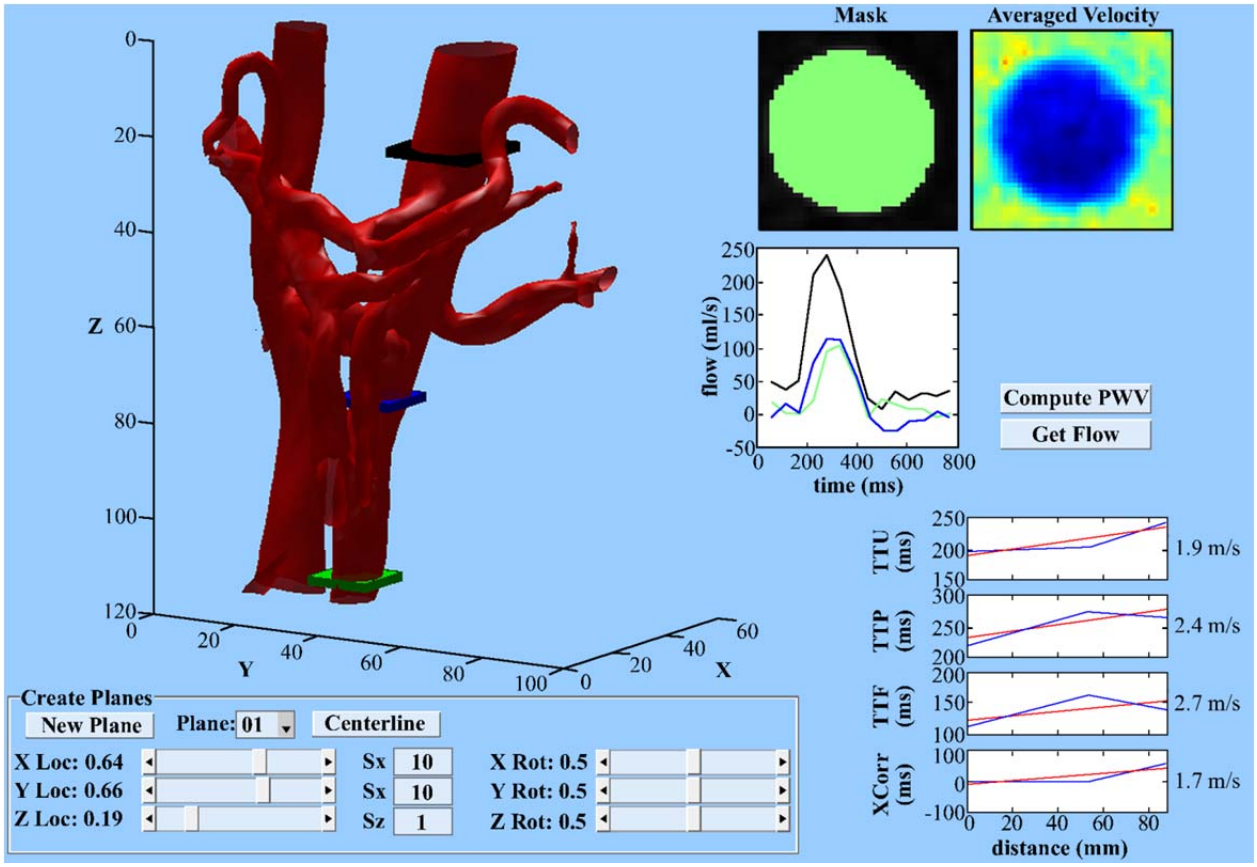

Figure 7.1 Custom MATLAB graphical user interface that allows for the analysis of pulse wave velocity from 4D phase contrast data. A time-averaged surface-shaded display of the 4D data set is loaded into the interface (upper left corner). Slider bars (lower left corner) are used to place any number of planes in the volume to obtain a series of flow waveforms (upper right corner). These flow waveforms are analyzed with the four pulse wave velocity algorithms (lower right corner). Note that the portion of this user interface dedicated to the analysis of pulse wave velocity from 2D data is not shown here. Also note that for simplicity in presentation, a time-averaged 4D data set from the abdominal aorta is shown here, despite the focus of this study being in the thoracic aorta.

~10.4 ms. The choice of four slices provides data from each section of the thoracic aorta and provides a low number of planes to minimize the scan time required for the 2D evaluation of PWV. A contrast-enhanced MR angiogram with 0.03 mmol/kg gadofosveset trisodium (Ablavar®, Lantheus, Billerica, MA) injected at 0.6 ml/s followed by a 30 ml saline chaser was performed per clinical standard to guide placement of the 2D planes (109).

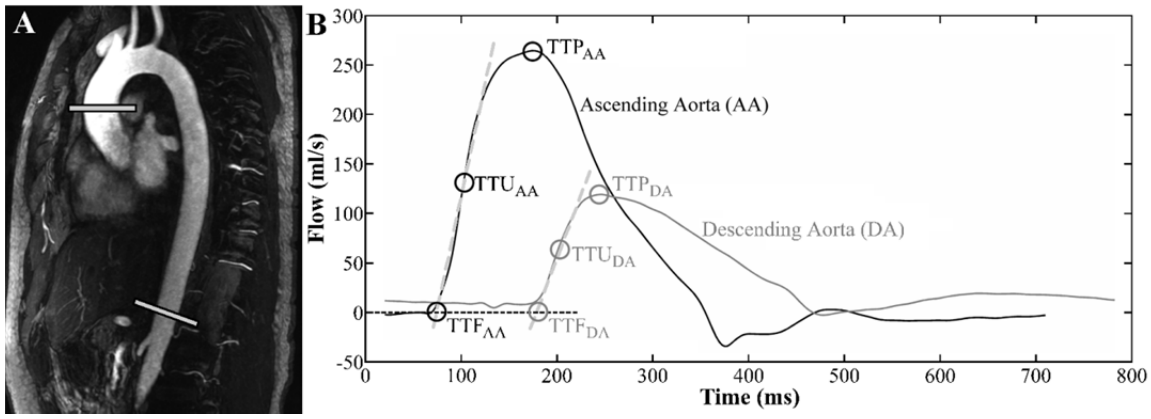

Figure 7.2 A contrast-enhanced angiogram (**A**) with representative planes in the ascending and descending aorta. Flow waveforms (**B**) from the two planes are shown with the time-to-upstroke (TTU), time-to-foot (TTF), and time-to-peak (TTP) algorithms. The best fit linear lines along the upstroke were used to identify the foot of the waveforms. Please note that the two planes shown in **A** are used to represent the two waveforms shown in **B**. In this study, four planes were used in the 2D approach and six planes were used in the 4D approach.

7.2.3 Data Analysis

A MATLAB-based software tool (The MathWorks, Natick, MA) was developed to perform the PWV calculations from 2D and 4D data (Figure 7.1**Error! Reference source not found.**). For 2D data, regions of interest (ROIs) were interactively drawn within the vessel lumen to measure the flow waveform. The distance calculation between the four scan planes was based on a double-oblique reformatted slice of the CE-MRA data ('candy cane' view, Figure 7.2). To compute a vessel centerline, the user placed a series of points in the approximate center of the vessel along the length of the aorta. A spline interpolation was created from this set of

points to approximate a vessel centerline. The intersection of the centerline with each individual 2D PC plane was used for distance calculations.

To analyze the 4D data, 6 planes slightly larger than the diameter of the aorta were manually placed double-obliquely such that a cross-sectional axial view of the aorta could be extracted from the 4D data set. These planes were placed in evenly spaced distances using a time-averaged surface shaded display of the aorta created from the PC angiogram. The exact distances between planes were determined by computing the centroid of each plane and calculating distances between centroids along a three-dimensional cubic spline interpolant that functioned as a vessel centerline. Six planes along the thoracic aorta was an adequate number of planes to compute the spline centerline. A fewer number of planes led to a spline that significantly deviated from the vessel center. Additionally, the 6 planes used in the 4D analysis covered the same superior-to-inferior distance along the aorta that was covered by the four planes used with the 2D approach above.

Flow waveforms were upsampled to 400 points via spline interpolation. Temporal shifts in the flow waveforms between planes were determined with four algorithms (Figure 7.2): TTU, TTP, TTF, and XCorr. The TTP, TTF, and XCorr algorithms were computed as previously described (98). Similar to previously proposed derivative methods of computing PWV (105), TTU was defined as the point of maximum acceleration on the upstroke of the waveform. As described previously (98), the distances between planes were plotted versus the time shifts computed from the TTU, TTP, TTF, and XCorr algorithms. A linear line was fitted to the data and the PWV was computed as the inverse slope of this line.

7.2.4 Statistical Analysis

Since neither test represents an established gold standard, 2D and 4D PWV calculations were compared following Bland and Altman analysis (90) for each of the four algorithms (TTU, TTP, TTF, and XCorr). The bias ± 2 SD was reported for each comparison and as an average for both the 2D and 4D approaches. 2D and 4D measurements were also compared with a paired Student's t-test. Inter- and intraobserver reproducibility of the 4D data was evaluated for 10/18 randomly chosen subjects and assessed with Bland-Altman analysis. The reproducibility of PWV measurements depends on several factors, including the slice selection and the placement of regions of interest. Given that the slice selection of 2D data was performed at the time of acquisition, the reproducibility of 2D data was not assessed because the *a priori* selection of 2D slices mitigates true differences in repeated measurements from 2D data.

Since four algorithms were evaluated in this study, it was of interest to assess and compare the variability of each algorithm. Given the relationship between PWV and age irrespective of blood pressure and other atherosclerotic risk factors (51), regression models of PWV on age and its square (age^2) were fitted to the data; the coefficient of determination R^2 was used to assess the percentage of variance in the response explained by the model. The results were plotted next to the raw data results; the shift between raw data and adjusted data represents the influence of age. This age adjustment thus allows for a comparison of the variability of the 2D and 4D PWV measurements despite the large age range (22 – 60 years) of our subjects. Differences in variability between 2D and 4D were assessed by a Brown-Forsythe ANOVA test.

To reveal physiological changes with age, data were separated into two groups based on age: subjects ≤ 35 years of age and subjects > 35 years of age. Data between age groups were

tested for differences with an unpaired Student's t-test ($p < 0.05$) for each method of analysis for both the 2D and 4D data sets.

The criterion for statistical significance was $p < 0.05$ (two-sided). There was no adjustment of p-values for multiple testing. Statistical analyses were performed in R 2.12.1 (R Development Core Team 2010).

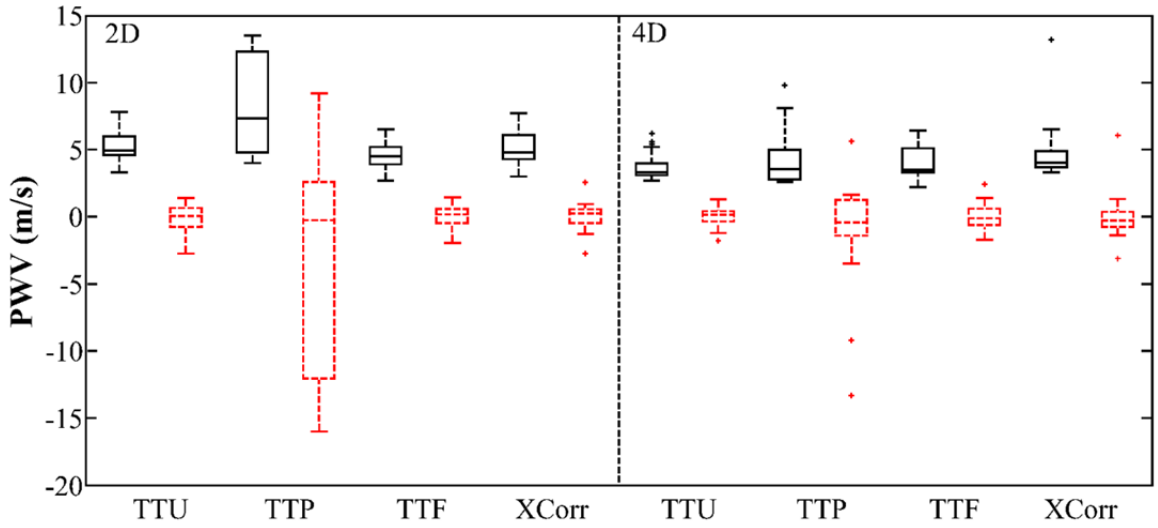

Figure 7.3 Box plots of PWV measurements as calculated from 2D PC slices and 4D PC VIPR data sets. The vertical axis was scaled around the box plots; two outliers (at 30.5 and 74.5 m/s) for the 2D TTP measurements lie outside of this range and are not shown in this graph. Raw data are shown with solid lines; age-adjusted values are shown with dashed red lines.

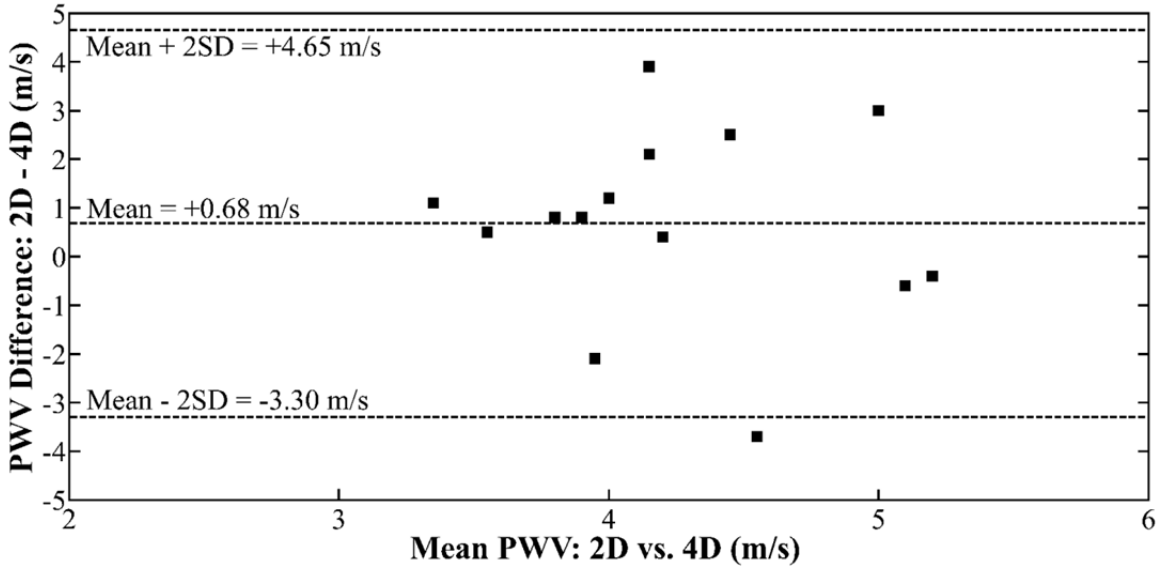

Figure 7.4 Bland-Altman analysis of the 2D vs. 4D PWV results computed with the TTF algorithm. PWV measurements from 2D PC data tended to be greater, with an average bias (± 2 SD) of +0.68 ± 3.98 m/s.

7.3 Results

Figure 7.3 shows the mean and standard deviation of the PWV measurements as calculated from 2D PC slices and 4D PC VIPR data sets. 2D and 4D PWV data were similar in magnitude and spread, except for values calculated with the TTP algorithm (Figure 7.3; solid box plots). Given the high degree of variability of the TTP data and non-physiological results, the TTP algorithm was deemed to be unreliable and results were excluded from the subsequent, more detailed analyses.

Overall, mean 4D PWV (n = 18) measurements ranged from 3.8 – 4.8 m/s, whereas mean 2D PWV (n = 14) measurements were greater and ranged from 4.6 – 5.3 m/s (Table 7.1). In a direct comparison of 2D and 4D results in 14 subjects, the mean PWV ranged from 3.5 – 4.2 m/s for the 4D data and from 4.6 – 5.3 m/s for the 2D data (Table 7.1). Bland-Altman analysis in these 14 subjects confirmed that 2D PWV measurements tended to be greater than 4D PWV

measurements, with bias and 95% limits of agreement (average bias ± 2 SD) of +1.8 ± 3.15, +0.68 ± 3.98, and +0.84 ± 3.37 m/s for the TTU, TTF, and XCorr algorithms, respectively (Figure 7.4). However, only TTU calculations showed significantly greater values for 2D than for 4D PWV measurements ($p < 0.001$; Table 7.1). For the 4D data ($n = 10$), interobserver reproducibility provided an overall mean (± 2 SD) bias of +0.30 ± 2.83 m/s and intraobserver reproducibility provided an overall mean (± 2 SD) bias of -0.01 ± 2.51 m/s (Figure 7.5; Table 7.1).

Table 7.1 PWV results from 2D and 4D data based on four different algorithms. Except for p-values, values shown are in m/s. Significant p-values are shown in bold.

Algorithm	4D (n = 18)	2D (n = 14)	4D (n = 14)	Bias ± 2 SD (n = 14)	2D vs. 4D p-values	4D intraobserver bias ± 2 SD (n = 10)	4D Interobserver bias ± 2 SD (n = 10)
TTU	3.8 ± 1.1	5.3 ± 1.3	3.5 ± 0.9	+1.8 ± 3.15	**0.001**	+0.15 ± 2.82	+0.40 ± 2.67
TTP	5.0 ± 10.8	14.1 ± 18.7	4.2 ± 2.0	+9.86 ± 35.9	0.054	-3.77 ± 18.6	-4.37 ± 21.8
TTF	4.0 ± 1.1	4.6 ± 1.1	3.9 ± 1.2	+0.68 ± 3.98	0.224	-0.10 ± 3.26	+0.78 ± 3.29
XCorr	4.8 ± 2.3	5.1 ± 1.4	4.2 ± 0.9	+0.84 ± 3.37	0.086	-0.09 ± 1.22	-0.27 ± 2.31

TTU = time-to-upstroke; TTP = time-to-peak; TTF = time-to-foot; XCorr = cross-correlation; SD = standard deviation

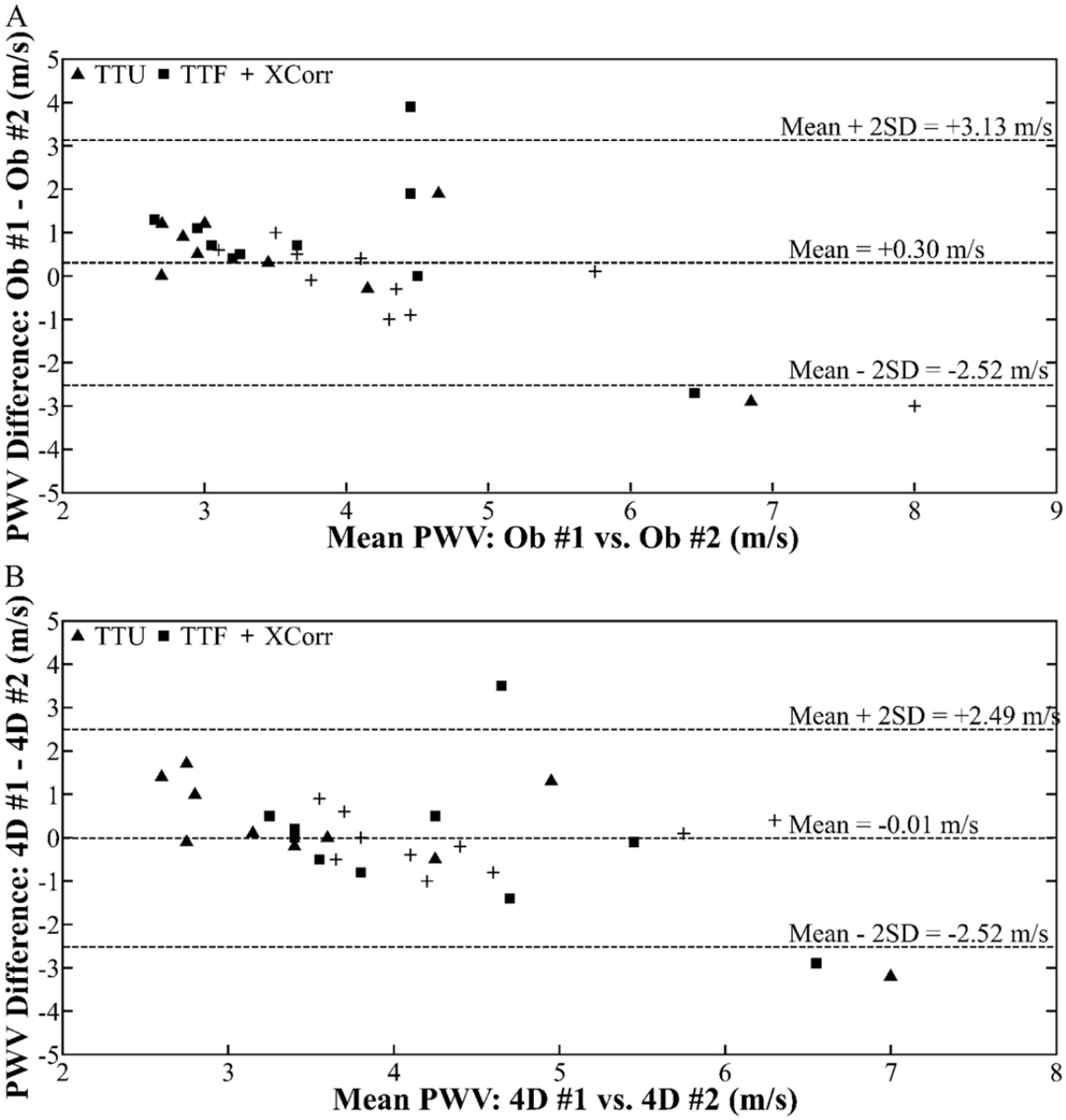

Figure 7.5 Bland-Altman plots for inter- (**A**) and intraobserver (**B**) reproducibility of 4D PWV measurements. Interobserver reproducibility provided a mean (± 2 SD) bias of +0.30 ± 2.83 m/s and intraobserver reproducibility provided a mean (± 2 SD) bias of -0.01 ± 2.51 m/s.

Box plots of the residuals of an age and age^2 regression model to the data demonstrated that some of the variability of the data (R^2 ranging from 11% to 46%) could be accounted for by the age of the subject (Figure 7.3; dashed red box plots). To test for differences in the variability of all eight groups in Figure 7.3, the Brown-Forsythe test demonstrated a p-value of 1.1 x 10^{-6},

indicating that one of the sets of measurements was significantly more variable than others. The residuals of the TTP data were visibly more variable than measurements computed from the other methods (Figure 7.3); removal of the TTP data from the Brown-Forsythe test demonstrated a p-value of 0.609, implying no significant differences in variability could be found between 2D and 4D measurements with the TTU, TTF, and XCorr algorithms, which justified the initial exclusion of TTP data.

For 4D PWV data grouped by ages of ≤ 35 and > 35 years of age, the TTU ($p = 0.02$) and XCorr ($p = 0.048$) algorithms demonstrated expected increases with age, whereas no trend with age could be found for the TTF ($p = 0.42$) data. No age/PWV relationships could be found in the 2D PWV data ($p \geq 0.073$).

7.4 Discussion

The results of this study demonstrate the feasibility of measuring global aortic PWV with the radially undersampled 4D flow-sensitive MRI technique, PC VIPR. While numerous studies have used MRI to evaluate PWV, this is the first study to perform such measurements with a radially undersampled 4D technique in a reasonable scan time without a sacrifice in spatial resolution or field of view. The 4D-based PWV measurements performed in this study were of similar magnitude to values reported in the literature (98, 104) and were of equal variability and similar magnitude to our reference 2D PWV measurements. Without a practical non-invasive 'gold' standard to compare these MRI-based PWV measurements, no conclusions can be made regarding the superiority or inferiority of the 4D technique for measuring PWV. Since 2D-based PWV measurements have been established as a reliable technique (95), the purpose of this study was to assess whether a 4D radially undersampled technique could estimate PWV reliably. Such

an investigation is necessary given the 4D acquisition's lower temporal resolution compared to 2D approaches and the reduced scan time relative to other flow-sensitive 4D techniques (98). While the 4D PC VIPR acquisition still requires 11.5 minutes of scan time, the acquisition of multiple 2D slices along with an angiogram is time-consuming due to the prescription of double-oblique planes and the recovery periods needed between successive breath holds. Furthermore, the analysis time for 2D and 4D PWV measurements was similar as well.

The PC VIPR technique provides several advantages aside from the ability to analyze the data with regards to PWV: PC VIPR does not rely on accurate slice prescriptions and also provides perfectly co-registered anatomical, angiographic, and three-directional flow information over a large volume, which can be qualitatively and quantitatively evaluated. Knowledge of the three-directional velocity information can be used to calculate other hemodynamics parameters, such as wall shear stress, oscillatory shear index, pressure gradients, turbulence, kinetic energy and other parameters. Therefore, the ability to characterize PWV with PC VIPR would be an additional useful parameter that could be derived from a single PC VIPR acquisition. M-mode-based MR imaging has superior temporal resolution (~3.5 ms), shorter scan times (~2 minutes) (100), and allows for regional PWV measurements, but only in a straight segment of the aorta. PWV measurements derived from the 4D technique in this study can be used for the whole aortic arch and can account for variations in vascular anatomy; however, the regional assessment of PWV is a significant challenge due to the limited temporal resolution of 4D PC MRI approaches.

TTP PWV measurements were the most variable and most prone to extremely aberrant, non-physiological values. TTP PWV is largely dependent on the systolic peak of the waveform, and hence, highly reliant on sufficient temporal resolution to detect the true systolic peak. In

addition, reflected pressure waves and noise contributions may have contributed to errors in the peak time from one plane to the next, making it the least robust algorithm of the methods tested here; this is in accordance with previous studies assessing TTP versus other algorithms (98, 104). Similarly for the 4D TTP calculations, the markedly lower temporal resolution of the PC VIPR technique may have increased uncertainty in sampling the true peak of the waveform in one plane but not another, leading to unreliable 4D TTP measurements.

TTU and TTF measurements rely on multiple points in the flow waveform and are thus less sensitive to temporal undersampling and noise. Additionally, the time points needed for TTU and TTF measurements are likely earlier in the flow waveform compared to time points affected by reflected waves. As XCorr measurements inherently use the entire waveform, XCorr is likely less susceptible to the effects of trigger delays and noise. As a result of these insensitivities, the TTU, TTF, and XCorr algorithms provided similar magnitude and variability. Given that occasional outliers occur with all of the PWV algorithms, we advocate for a multi-algorithm approach to PWV measurements that includes the TTU, TTF, and XCorr algorithms. Thus, an extreme value from one algorithm can be compensated for by the similarity between values from the remaining algorithms. A multi-algorithm approach to PWV measurements requires at least three algorithms; if only two algorithms were used and the values from each were substantially different, it is unknown which number can be trusted, if any. Given the unreliability of the TTP algorithm, an algorithm was needed in addition to the TTF and XCorr algorithms that have been established in the literature. The TTU algorithm provides the third measurement in the multi-algorithm approach.

The ~32 ms temporal resolution of the PC VIPR sequence is a limitation of the study and could be insufficient to resolve differences for diseased subjects with PWV values greater than 5 m/s. The lower temporal resolution of the PC VIPR technique may also explain why average PWV values were lower than with the 2D approach to PWV measurements. Since this study did not include diseased subjects, we are uncertain of the ability of our 4D PWV technique to detect values greater than 5 m/s, given that this was the greatest value detected in this study. In future studies with diseased subjects and elevated pulse wave velocities, analysis planes may need to be placed further apart from one another to resolve the differences in waveform characteristics. Although our 4D PWV measurements were not compared to the gold standard invasive pressure measurements, our method was compared to 2D PWV measurements, which have been validated previously with invasive pressure measurements (95). While four planes were used to measure PWV with 2D data, six analysis planes were used to compute PWV with the 4D data due to the centerline algorithm employed in our analysis tool. Although the number of analysis planes is different between the 2D and 4D approaches, the spatial extent of the planes was the same for measuring global aortic PWV. Nevertheless, this limitation could be avoided with the use of an alternative algorithm for computing the vessel centerline. Despite having strict inclusion criteria in terms of BMI and history of smoking and cardiovascular disease, our subjects spanned a large age range. While our analysis of variability accounted for variation due to age, a study with subjects in a narrower age range would be useful for more thoroughly comparing the variability of the TTU, TTF, and XCorr algorithms. Although a degree of bias was found in comparing the 2D and 4D PWV measurements (on the order of 0.68 – 1.8 m/s), differences were relatively small. Such small differences are unlikely to affect clinical decisions based on PWV

measurements because diseased subjects are likely to have a PWV that is approximately double the PWV of a normal subject (51).

Problems with cardiac gating led to a reduction in the number of cases included in the 2D to 4D comparison. As with all functional cardiovascular MR, sequences rely on proper gating. The two subjects with poor cardiac gating thus led to the improper acquisition of data. An additional problem with cardiac gating was met with the 2D acquisition. With the use of prospective cardiac gating, flow waveforms measured from slices acquired proximal to the heart were occasionally missing part of early systole. Since prospective gating requires a trigger from the QRS complex, the electrical delay between this trigger time and the acquisition led to the absence of the upstroke in slices through the ascending aorta and aortic arch. Such delays could be the result of a higher heart rate, a truly elevated pulse wave velocity, or anatomical differences that shorten the distance the systolic bolus needs to travel to the plane of interest. Without the upstroke, algorithms like TTF and TTU cannot function properly. Since the PC VIPR acquisition was retrospectively cardiac gated, no data were missing from the flow waveforms. In future studies retrospectively gated 2D PC acquisitions or Fourier-encoded data in straight vessel segments should be used as reference standards.

In conclusion, the 4D PC VIPR acquisition is a promising means of obtaining PWV measurements. The 4D PWV results included in this study were similar in magnitude and variability to values in the literature and to our reference 2D PWV results for the TTU, TTF, and XCorr algorithms. Low inter- and intraobserver variability for the 4D approach lends credence to its use in future clinical applications. Further studies with the 4D technique are warranted,

including studies in patients with variable disease severity, elevated PWV, and across a more complete spectrum of ages.

Chapter 8 Wall Shear Stress Downstream of an Aneurysm

PURPOSE: To determine whether ascending aortic aneurysms affect wall shear stress (WSS) in the descending aorta using a four-dimensional (4D) flow-sensitive time-resolved MR acquisition.

MATERIALS AND METHODS: Nine healthy volunteers and ten patients with an ascending aortic aneurysm were evaluated with a 4D flow-sensitive MR acquisition. Wall shear stress was computed in the descending thoracic aorta for each time point along the cardiac cycle. Peak WSS, aortic diameter, helicity, and flow/velocity were evaluated and compared between healthy volunteers and aneurysm patients.

RESULTS: Peak WSS over the cardiac cycle was significantly lower ($P < 1x10^{-9}$) in patients than in volunteers. Patients had significantly larger ascending aortas than normal subjects ($P < 1x10^{-6}$); no difference was found in the vessel diameter of the descending aorta ($P = 0.28$). Helicity in patients decreased as the aorta was traversed, whereas helicity in healthy volunteers remained steady ($P = 0.023$). Total and peak flow and mean and peak velocity were significantly higher in the volunteers for both the ascending and descending aorta.

CONCLUSION: Given the geometric changes induced by ascending aortic aneurysms, abnormal hemodynamics arise in both the aneurysm and in the downstream vasculature. In this study we determined that ascending aortic aneurysms lead to significantly lower WSS in the descending aorta.

8.1 Introduction

There is an ongoing discussion regarding the effects altered geometric conditions in the aorta might have on hemodynamics and vascular pathologies, such as atherosclerosis. Since geometry determines the distribution of force on the arterial walls as exerted by the blood ejected by the left ventricle, alterations in geometry cause changes in this force distribution. Wall shear stress (WSS) is one biomechanical factor that may be affected by such changes in force.

Since changes in geometric conditions may lead to changes in WSS, it is important to consider how such changes in WSS may lead to pathology. Several investigators have demonstrated that WSS affects the production of endothelial vasoactive mediators (110-112), as well as endothelial gene expression (113). Others have demonstrated that the magnitude of WSS affects the up- and down-regulation of genes, including various transcription factors, growth factors, adhesion molecules, and enzymes (44). Additionally, dysregulation of vascular stresses may lead to a pathologic state. For example, elevated peak longitudinal WSS may initiate aneurysm formation (114), whereas low peak longitudinal WSS may contribute to aneurysm growth (115). Such studies reflect the sensitivity of the vascular endothelium to loading conditions. Studies have also demonstrated an association between the distribution of atherosclerotic lesions and low wall shear stress (37, 116-118). The development of atherosclerotic plaques in areas of low wall shear stress is in part due to the loss of the atheroprotective effects of higher WSS on endothelial cell gene expression. Conversely, sufficiently low WSS leads to the production of proatherogenic inflammatory mediators (59). These changes in gene expression result in intimal thickening and the subsequent development of atherosclerosis.

WSS has been estimated with a variety of modalities, including ultrasound Doppler (119), computational fluid dynamics (120), and most recently magnetic resonance imaging (MRI) (45, 121). Ultrasound provides a quick and low-cost method of estimating WSS in vivo, but lacks three-dimensional information and has a limited acoustic window, especially in the mediastinum, due to the reflection of waves by air contained within the lungs. While computational fluid dynamics provides high spatial and temporal resolution for WSS analysis, it lacks a true representation of in vivo conditions, in addition to being computationally intensive when analyzing complex flow patterns. MRI measurements of WSS provide a means of measuring WSS in vivo, but studies in the past have been limited to 2D slices (45, 122-125) or have relied on semiquantitative descriptions of 3D flow patterns (126-130). Compared to computational fluid dynamics, MRI suffers from low spatial and temporal resolution, and as a result, the true WSS is very challenging to assess and several of these MR studies averaged WSS over the circumference of the vessel lumen. A newer method of acquiring four-dimensional (4D) MR flow information with radial undersampling, termed PC VIPR (phase contrast with vastly undersampled isotropic projection reconstruction), provides shorter scan times with improved spatial resolution, which may provide better estimates of WSS than other MR techniques (102, 106).

Geometric changes due to aneurysms are likely to have a significant effect on hemodynamics. Some investigators have demonstrated that even subtle differences in vessel geometry lead to significant changes in WSS (131). The fact that geometric deformities, such as aneurysms, produce pronounced rotational flow within the vasculature is one explanation for how geometric changes may lead to changes in WSS (132). Given the sensitivity with which

wall shear stress changes, we suspect that geometric and hemodynamic changes as a result of aneurysm formation would have a significant effect on regional wall shear stress. While measurements of WSS have been investigated within the aneurysmal bodies, the downstream effects of an aneurysm on WSS remain largely unknown.

The purpose of this study was to evaluate differences in WSS downstream of an ascending aortic aneurysm in a population of ten subjects with such an aneurysm and in nine healthy volunteers with the use of a high-resolution PC VIPR MR acquisition. We hypothesized that WSS in the descending aorta of patients with an ascending aortic aneurysm would be lower than the WSS in the descending aorta of normal volunteers. The analysis of WSS downstream provides a more complete picture of aneurysmal effects, as significant changes in WSS as a result of aneurysms may have important implications for diagnosis and treatment planning.

8.2 Materials and Methods

8.2.1 MRI

This HIPAA compliant study was approved by our institutional human subjects review committee and written informed consent was obtained from all subjects. 4D phase contrast data were acquired with PC VIPR (vastly undersampled isotropic projection reconstruction) on 1.5T or 3T MR scanners (GE Healthcare, Waukesha, WI) in nine healthy volunteers without cardiovascular disease (6 men; 3 women; average age = 34.2 ± 13.5 [± 1SD] years, range 21 – 54 years) and ten patients with an aneurysm in the ascending aorta (6 men; 4 women; average age = 44.7 ± 22.5 years, range 10 – 85 years). Differences in age between the volunteer and patient groups were evaluated with an unpaired equal variance Student's t-test ($P < 0.05$). Bicuspid

aortic valves were present in 7/10 patients. None of the aneurysm patients had Marfan syndrome, Ehlers-Danlos syndrome, or an aortic dissection. Four of the ten aneurysm patients had hypertension. Six of the ten aneurysm patients were treated with one or more of the following medications at the time of the study: benazepril/hydrochlorothiazide, ropinirole, metoprolol, carvedilol, atenolol, and losartan. Scans were performed with an eight-channel cardiac coil and the following parameters: imaging volume = 320 x 320 x 180 mm^3, readout = 256-320, reconstructed to 1.0-1.25 mm^3 acquired isotropic spatial resolution, VENC of 80-120 cm/s, TR/TE/flip = 8.7ms/2.8ms/10º, retrospective cardiac and respiratory gating, reconstructed to twenty time frames along the cardiac cycle, scan time ~ 10 min. Contrast was administered intravenously (0.1 mmol/kg gadobenate dimeglumine, MultiHance, Bracco Diagnostics, Inc., Princeton, NJ, USA) prior to the 4-point dual-echo PC VIPR acquisition (106).

8.2.2 Vessel Segmentation and WSS Estimation

Vessel segmentation was performed manually with in-house software (133) (MATLAB version 8.0, The MathWorks Inc., Cambridge, MA, USA). First, points were selected around the circumference of the vessel on complex difference images reformatted as axial to the vessel. From these points, a cubic spline was created within the axial plane. This step was repeated on every fifth axial slice ranging from the end of the aortic arch to immediately superior to the celiac artery (Figure 8.1a,d). From this array of axial splines, splines in the superior-to-inferior (SI) direction—along the length of the aorta—were also created from points around the circumference of each axial spline. The intersection of the SI and axial splines created surface points along which an inward unit normal vector was computed from the derivatives of both

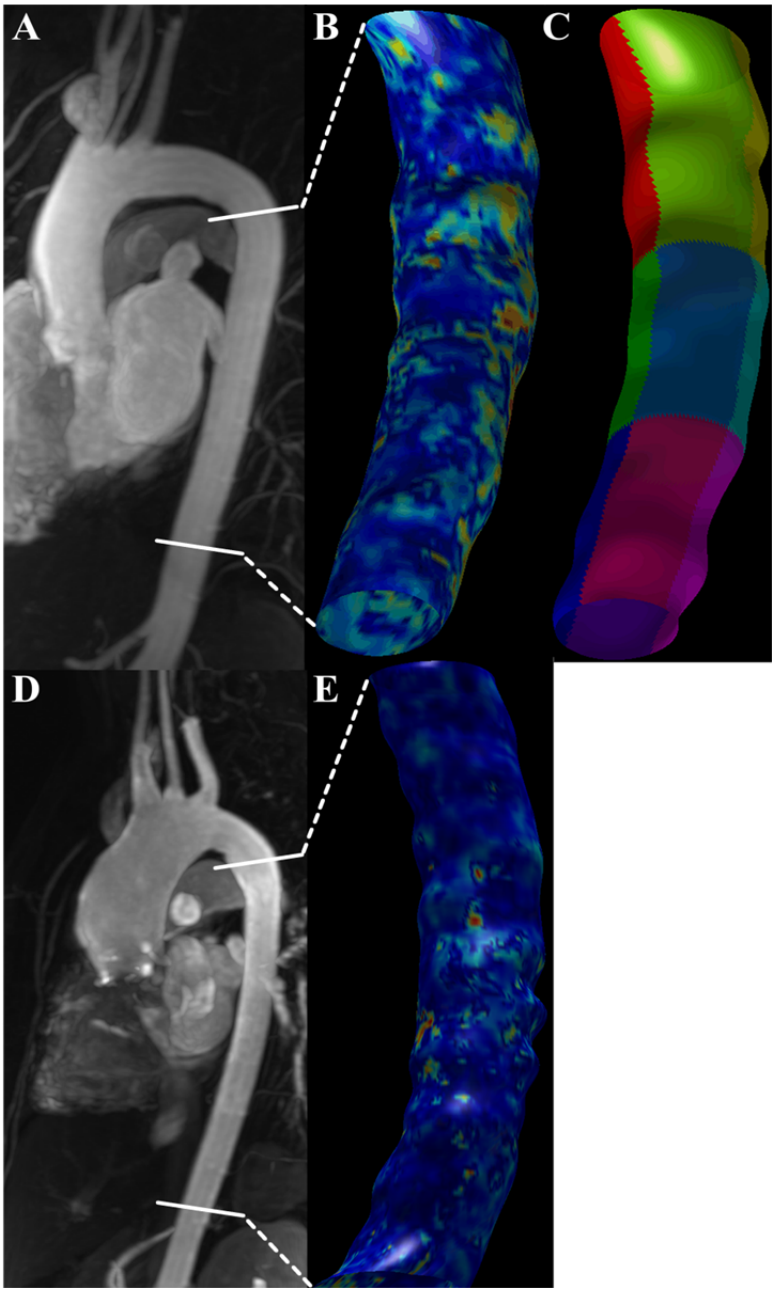

Figure 8.1 A. Maximum intensity projection of the aorta in a healthy volunteer. **B.** Map of wall shear stress measurements in the descending thoracic aorta for a single time frame in a healthy volunteer. **C.** Twelve segments were used to bin wall shear stress measurements in the descending thoracic aorta for all subjects. **D.** Maximum intensity projection of the aorta in a patient with an ascending aortic aneurysm. **E**. Map of wall shear stress measurements in the descending thoracic aorta for a single time frame in a patient with an ascending aortic aneurysm. In parts **B** and **E**, low wall shear stress values are shown in blue, while the greatest values are shown in red.

axial and SI splines; total wall shear stress was then calculated as the viscosity of blood multiplied by the slope of the velocity along this unit normal vector, as described previously (133) (Figure 8.1b,e). Blood viscosity was assumed to be 0.04 Pa·s for all subjects. This process was repeated for each time frame over the cardiac cycle.

8.2.3 Data Analysis

Measurements of aortic diameter were acquired double obliquely from contrast-enhanced magnetic resonance angiograms or the complex difference images of the PC VIPR data set using a Vitrea workstation (Vital Images, Minnetonka, MN, USA). Diameter measurements were evaluated in the ascending aorta at the level of the pulmonary artery in healthy volunteers and at the maximum aortic diameter in the ascending aortic aneurysms. Diameters were also measured at the mid aortic arch and the descending aorta at the level of the pulmonary artery and diaphragm. An aneurysm index was computed as the ratio of the ascending aortic diameter at the level of the pulmonary artery to the descending aortic diameter at the level of the diaphragm (134). The aneurysm index and diameters were compared between volunteers and patients with an unpaired equal variance Student's t-test ($P < 0.05$).

A custom-built MATLAB tool (133) (MATLAB version 8.0, The MathWorks Inc., Cambridge, MA, USA) was developed to analyze planes from the 4D data set and to extract velocity and flow information. Measurements of total flow over the cardiac cycle, peak flow, mean velocity, and peak velocity were extracted from planes placed in the ascending and descending aorta at the level of the pulmonary artery. Such analyses were performed in a subset of the data (five patients and five volunteers); measurements were compared between patients

and volunteers in both the ascending and descending aorta using an unpaired equal variance Student's t-test ($P < 0.05$).

Measurements of WSS for each surface were binned and averaged into twelve segments for each time frame (Figure 8.1c)—grouped into 4 circumferential regions at three SI levels. WSS was averaged for the entire segmentation in the descending thoracic aorta and plotted for each of the volunteers and patients. A diastolic baseline WSS was obtained for each subject by averaging all WSS measurements in the final five time frames; baseline measurements were compared between volunteers and patients with an unpaired equal variance Student's t-test ($P < 0.05$).

The peak WSS for each of the twelve segments was averaged independently for the groups of volunteers and patients; averages between volunteers and patients were compared in each segment with an unpaired equal variance Student's t-test ($P < 0.05$). Additionally, the time frame in which the peak WSS occurred, along with the percent increase in WSS from diastolic baseline to peak, were compared between volunteers and patients with an unpaired equal variance Student's t-test ($P < 0.05$). Box plots were created for these measurements of baseline and peak WSS.

To assess the presence of helicity and vorticity within the image volume, the phase difference PC VIPR data sets were evaluated with a visualization software package (EnLiten; CEI Inc., Apex, NC, USA). Helicity was scored on a scale of 0 to 4, with 0 being no clear pattern of helicity and 4 being pronounced helicity. Vorticity was scored as either present or not. While quantitative and automatic methods of assessing helicity and vorticity would be ideal, simple and

reliable measurements have proven to be difficult (135, 136). Helicity and vorticity scoring were performed on three time points: peak systole, late systole/early diastole, and late diastole. For each time point, scoring was performed separately for the upper, middle, and lower segments as shown in Figure 8.1c. Scoring of helicity and vorticity was repeated with a second observer to assess interobserver agreement.

Agreement for helicity and vorticity scoring was evaluated with Cohen's kappa with linear weights. A 95% confidence interval (137) and p-value for the hypothesis of kappa = 0 with $P < 0.05$ were also generated. Box plots of the average scores between observers were prepared for the three time points and the three segments. Additionally, helicity scores averaged from the two observers were used in linear mixed effects models to assess the effect of aneurysm presence, cardiac cycle stage, and aortic segment on helicity. $P < 0.05$ (two-sided) was used as the criterion for statistical significance. Statistical graphics and computations were obtained in R 2.12.1 (R Development Core Team 2009) with the nlme package 3.1-97.

Table 8.1 Aortic diameter measurements in ten patients and nine volunteers.

	Aortic Diameter (mm)	
	Volunteers	Patients
AscAo – PA*	27.6 ± 3.3	42.4 ± 4.5
Aortic Maximum	N/A	44.8 ± 4.5
Aortic Arch	23.8 ± 2.2	25.0 ± 4.6
DescAo – PA	22.1 ± 2.6	23.8 ± 4.0
DescAo – Diaphragm	20.0 ± 1.6	22.9 ± 7.5
Aneurysm Index*	1.3 ± 0.1	2.0 ± 0.4

AscAo = Ascending Aorta; PA = pulmonary artery; DescAo = Descending Aorta
* $P < 0.05$

8.3 Results

No significant difference was found in age between patients and volunteers (P = 0.24). Images acquired from the PC VIPR acquisition were of good technical quality and appropriate for analysis. Diameter measurements in the ascending aorta at the level of the pulmonary artery were significantly larger in the patients than in the volunteers (Table 8.1; $P < 1 \times 10^{-6}$). No significant differences were found for diameter measurements in the aortic arch (P = 0.48), descending aorta at the level of the pulmonary artery (P = 0.28), or the descending aorta at the level of the diaphragm (Table 8.1; P = 0.30). The aneurysm index was significantly higher in the patients (2.0 ± 0.4; range: 1.1 – 2.4) than in the volunteers (Table 8.1; 1.3 ± 0.1; range: 1.2 – 1.6; $P < 1 \times 10^{-3}$). Total flow, peak flow, mean velocity, and peak velocity were all significantly higher in the volunteers than in the patients for both the ascending and descending aorta (P < 0.05; Table 8.2).

Table 8.2 Mean values of total flow, peak flow, mean velocity, and peak velocity for five patients and five volunteers.

	Patients/Volunteers	
	Ascending Aorta (P-value)	Descending Aorta (P-value)
Total Flow (ml/min)	2660.8/5278.9 (0.001)	1407.3/3603.0 (0.003)
Peak Flow (ml/s)	206.3/415.6 (0.005)	150.9/250.4 (0.040)
Mean Velocity (cm/s)	2.7/10.1 (2.1×10^{-6})	5.6/12.4 (0.005)
Peak Velocity (cm/s)	10.0/45.9 (1.2×10^{-4})	29.6/50.4 (0.033)

Table 8.3 Peak wall shear stress over the cardiac cycle in ten patients and nine volunteers.

	WSS (N/m^2) in Patients/Volunteers*			
	Lateral	Medial	Anterior	Posterior
Upper	0.33/0.56	0.48/0.74	0.44/0.81	0.38/0.67
Middle	0.49/0.72	0.48/0.80	0.44/0.81	0.44/0.69
Lower	0.41/0.72	0.47/0.74	0.42/0.70	0.40/0.66

* Peak WSS was significantly lower in patients than volunteers for all twelve segments (P < 0.05)

Spatially averaged wall shear stress over the entire descending thoracic aorta is plotted over the cardiac cycle for all volunteers and patients in Figure 8.2. Wall shear stress tended to be lower in patients than volunteers. The baseline WSS, averaged over the entire segmentation for the final five time frames, was 0.082 ± 0.03 N/m^2 for the ten patients and 0.064 ± 0.01 N/m^2 for the nine volunteers. No significant differences were found between these baseline WSS measurements (P = 0.12).

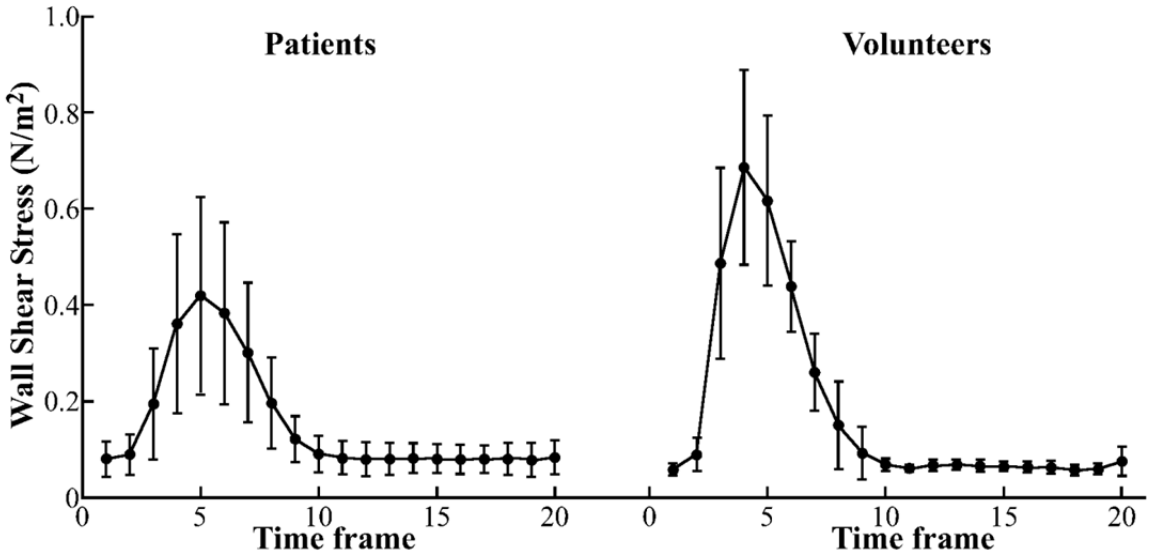

Figure 8.2 Spatially averaged wall shear stress in the descending thoracic aorta. Maximum wall shear stress was greater in the volunteers than in the patients ($P < 1 \times 10^{-9}$). No differences were found during diastole between the patients and volunteers. Peak wall shear stress tended to occur earlier in the cardiac cycle in the volunteers than in the patients. Errors bars show standard deviation.

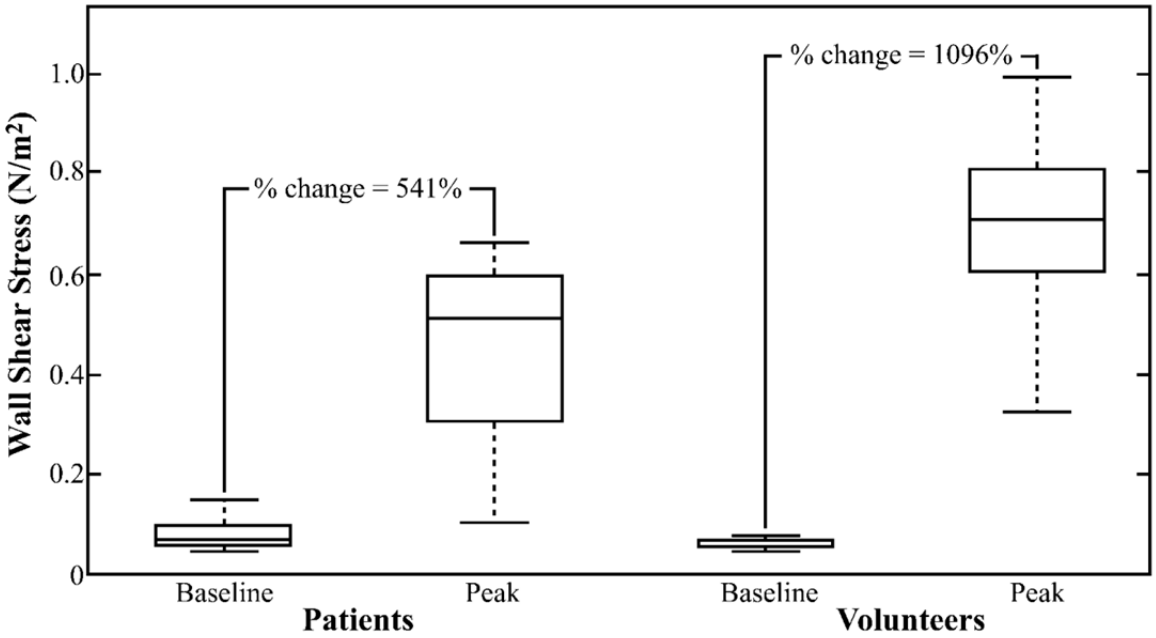

Figure 8.3 Box plots for average diastolic and peak wall shear stress measurements in the descending thoracic aorta. Average percent increases from baseline to peak are shown above the box plots. Percent increases in WSS from baseline to peak were significantly higher in volunteers than in patients ($P < 0.001$).

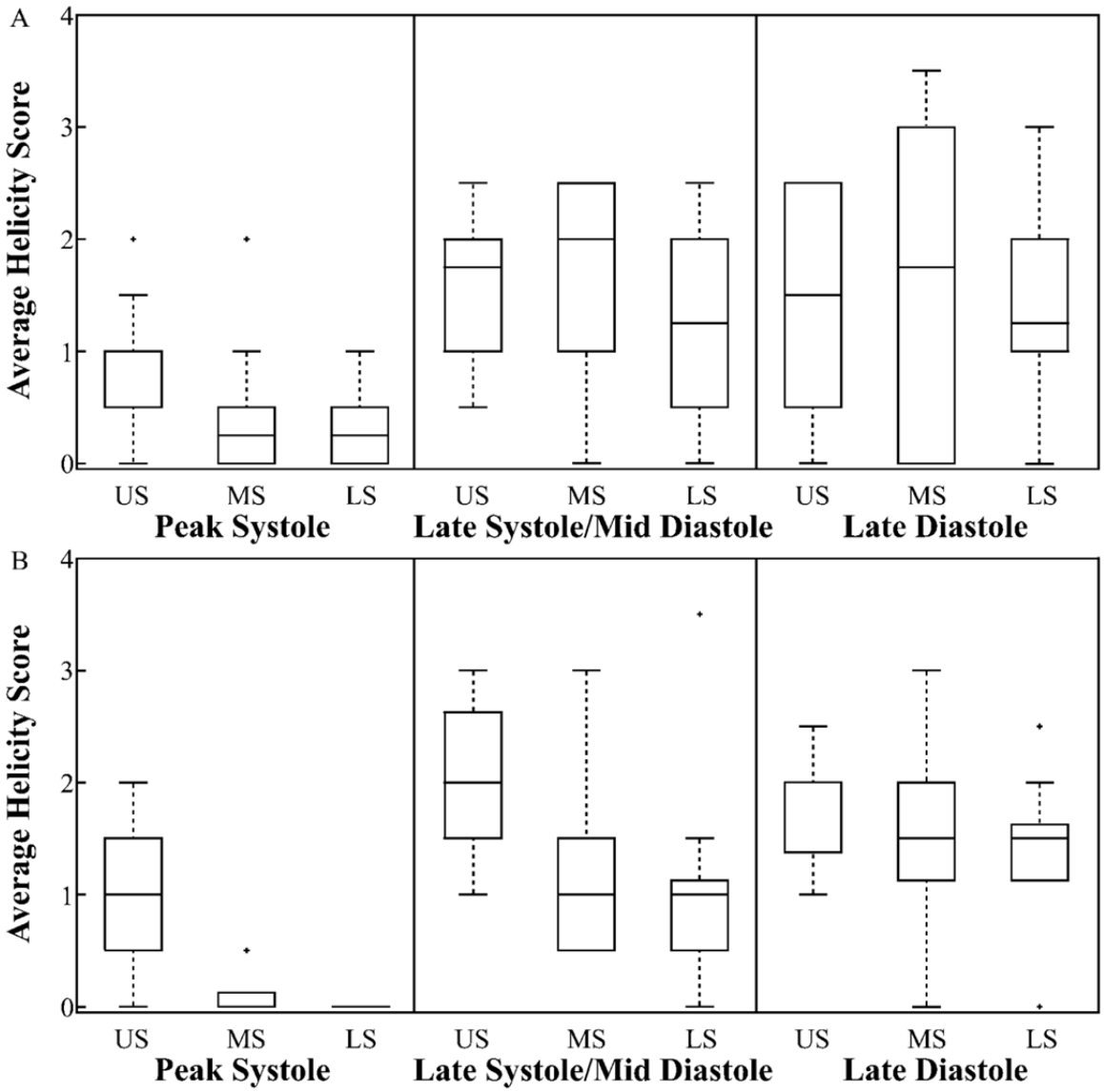

Figure 8.4 Box plots for average helicity scores in patients (**A**) and volunteers (**B**). Helicity scores were computed on a scale of 0 to 4, with 0 being no helicity and 4 being pronounced helicity; helicity was scored at three time points: (1) Peak Systole, (2) Late Systole/Mid Diastole, and (3) Late Diastole. Within each time point, helicity was scored in three segments in the descending thoracic aorta: (1) Upper Segment (US), (2) Middle Segment (MS), and (3) Lower Segment (LS).

Peak WSS was significantly lower in patients (average = 0.43 ± 0.05 N/m^2) than in volunteers (average = 0.72 ± 0.07 N/m^2; $P < 1 \times 10^{-9}$) over the twelve segments (Table 8.3). The time frame with the greatest WSS tended to occur later in patients (average = 6)

than in volunteers (average = 4), although these values were not significantly different (P = 0.22). The percent increase in WSS from baseline to peak was significantly higher in volunteers (average = 1096%) than in patients (average = 541%; P < 0.001; Figure 8.3).

For the helicity scoring, interobserver variability produced a Cohen's kappa of 0.42 (95% CI: 0.23 – 0.61; P < 0.001). For the vorticity scoring, interobserver variability produced a Cohen's kappa of 0.28 (95% CI: -0.05 – 0.60; P < 0.01). Helicity tended to be less common during peak systole than other time points (Figure 8.4). Vorticity was uncommon amongst the data. The ANOVA analysis demonstrated that there were differences in helicity due to cardiac cycle stage (P < 0.001), with significantly less helicity during peak systole than during late diastole (P < 0.001), but no differences were found for late systole/early diastole (P = 0.61).

8.4 Discussion

We present for the first time, to our knowledge, an analysis of wall shear stress measurements in the descending thoracic aorta downstream of an ascending aortic aneurysm. WSS was lower on average in the cohort of patients than in the cohort of volunteers, with a significantly lower peak WSS and a significantly lower percent increase from diastolic baseline to peak.

Given the significant differences in WSS measurements in the descending thoracic aorta between the two cohorts, it is suspected that aneurysms are the causal factor for such differences. For example, it is well-known that WSS is inversely related to the cube of the vessel radius (138). Since vascular geometry has an effect on hemodynamic forces, the aneurysmal dilation of the ascending aorta likely increases the vessel diameter to such a degree that, for the maintenance

of flow, the velocity must decrease. An expanded diameter would cause a decrease in velocity and contribute to the decrease in WSS seen in our study. Indeed, measurements of aortic diameter demonstrated a significantly larger ascending aorta and aneurysm index in the patients than in the volunteers (Table 8.1), indicating a substantial change in the geometry of the aorta compared to the normal volunteers. Furthermore, aneurysms tend to add a rotational component to the flow in the vicinity of the aneurysmal body (132). The kinetic energy of the flowing blood is dampened as the aneurysm creates this helical flow component. In helical flow, energy put into rotation detracts from the net energy put into forward flow. Such a decrease in energy will lead to lower flow rates in the direction of bulk blood flow and therefore a smaller velocity gradient in the calculation of WSS. There are two components of wall shear stress—circumferential and tangential—and thus any blood flow directed perpendicular to these components as a result of helical flow will not contribute to the total wall shear stress, as reported in this study. Increased helicity has the potential to significantly impact total wall shear stress values. However, in our study, the aneurysm patients were found to have equal or less helicity than the healthy volunteers in the descending aorta. The inability to distinguish the degree of helicity between subject groups could be due to the small sample size, the result of a true lack of helicity distal from the aneurysmal body, or the limitation of the five-point scale used to score the degree of helicity.

Given that aneurysms cause hemodynamic changes locally and distally, clinicians must consider how WSS may play a role in an ensemble of aneurysm-induced pathologies. While Meng *et al.* demonstrated that sufficiently high WSS may instigate the formation of an aneurysm (114), the aneurysm in turn decreases WSS. The decrease in WSS subsequent to aneurysm

formation has a two-fold effect: potential expansion of the aneurysm itself, as demonstrated by Boussel *et al*. (115), and the potential for atherosclerotic plaque formation (118) downstream of the aneurysm. Since pathologies may arise downstream of an aneurysm, and since the aneurysm may be exacerbated by self-induced hemodynamic changes, it is important for clinicians to evaluate the entire region surrounding the aneurysm. Use of a 4D phase contrast MRI acquisition, as used is this study, is particularly well suited for evaluating the aneurysm and the surrounding area using both wall shear stress and flow/velocity measurements.

Significant differences were found in flow and velocity measurements between normal subjects and patients with an ascending aortic aneurysm (Table 8.2). Differences in velocity were expected as a result of differences in the diameter of the ascending aorta. However, differences in flow between groups were unexpected. Upon further review of the patients' charts, patients who had lower flow values were found to have been on one or more anti-hypertensive medications for the medical treatment of their aneurysm. While the effects of these drugs on stroke volume, heart rate, and cardiac output are variable depending on the combination of drugs in a given individual and the duration for which a person has taken the medication, these medications likely affected the flow values measured in this patient group.

While we were able to find a significant difference in WSS parameters between patients and volunteers, this study included a limited number of subjects. For the sake of analysis, measurements of WSS were binned into twelve arbitrary segments. While Wentzel *et al.* also used quarters axially to bin the data, we chose to bin our data into three vertical segments instead of four (139). Recalculating the numbers with a different number of bins could affect the differences determined in our study. Nevertheless, our WSS measurements were on the same

order of magnitude as Wentzel's results. Due to the relatively low sample sizes in this study, clinically relevant differences in helicity may have gone undetected due to low statistical power. Our assumption that helicity is continuous is a possible drawback. We did not pursue the use of statistical methods for an ordinal response for two reasons: (1) these methods are more complex and less interpretable than mixed-effects models, and (2) we felt the 5-point scale was rich enough that discreteness would not affect us unduly. Diagnostic plots did not reveal any problems with model fit. Given limitations in spatial resolution, and as a result, partial volume effects, it is difficult for MRI to identify the true vessel wall. As a result, MRI-based measurements of WSS are likely not measurements of true WSS, but are rather semi-quantitative in nature and useful for making relative comparisons between groups. Furthermore, our study did not adjust p-values for multiple hypothesis tests, which might give rise to an inflated Type I error. Our study did not evaluate the aneurysm patients post-treatment with, for example, doxycycline, a statin, or an angiotensin II receptor blocker. Numerous flow-derived parameters are involved in the development of atherosclerosis in addition to wall shear stress, including oscillatory shear index and turbulence. This study only focused on differences in wall shear stress. Finally, no reference standard exists with which we can compare our measurements of WSS. Despite these limitations, the significant differences between patients and volunteers seen in this study demonstrate that MRI-based WSS measurements provide a valuable surrogate marker for hemodynamic forces.

In conclusion, we have demonstrated significantly lower WSS downstream of an ascending aortic aneurysm as compared to healthy volunteers. The presence of abnormal hemodynamics both within the aneurysm and in the downstream vasculature necessitates that the

entire region surrounding the aneurysm be evaluated. Analysis with a 4D imaging technique, such as the MRI approach used in this study, is particularly useful for such an evaluation. Further studies are needed to evaluate the long-term effects of the decreased WSS found in this study.

Chapter 9 Repeatability and Internal Consistency of Flow Measurements

PURPOSE: To assess the repeatability and internal consistency of flow measurements in the renal arteries and pararenal aorta with the use of 2D and 4D phase contrast (PC) magnetic resonance imaging (MRI).

MATERIALS AND METHODS: Ten healthy volunteers were imaged with a radially-undersampled 4DPC technique centered over the renal arteries and with four 2DPC slices placed in the supra/infrarenal aorta and the left/right renal arteries; this MR exam was performed twice on each subject. Flow measurements in all four vessels were computed from 2D and 4D data. Student's t-tests ($p < 0.05$) were used to assess differences between in-flow (suprarenal aorta) and out-flow (infrarenal aorta + left renal artery + right renal artery) for the 2D and 4D techniques, to compare in- and out-flow, and to compare repeated measurements of 2D and 4D flow measurements.

RESULTS: No significant differences were found in repeated measurements of 2D ($p = 0.15$) or 4D ($p = 0.39$) data. No significant difference was found between 2D (3.4 ± 2.8 ml/cardiac cycle) and 4D (3.5 ± 2.7 ml/cardiac cycle) in- and out-flow differences ($p = 0.88$). Out-flow was greater than in-flow for 2D measurements ($p = 0.003$); no difference was found for 4D measurements.

CONCLUSION: The 2D and 4D techniques demonstrated strong repeatability and internal consistency of flow measurements in the renal arteries and pararenal aorta.

9.1 Introduction

In recent years 4D phase contrast (PC) magnetic resonance imaging (MRI) has become more common as a tool to investigate anatomy, angiography, and flow and velocity information. 4D PC acquisitions provide large volumetric coverage and three-directional velocity encoding for multiple time points in the cardiac cycle. Additionally, 4D PC data sets can be used to derive various flow-related parameters, including pulse wave velocity, pressure gradients, and wall shear stress (140). A number of studies have been performed to validate 4D PC flow measurements, such as the comparison of 4D PC flow measurements to flow phantoms (102, 141) and to 2D flow measurements as a reference standard (102, 103, 142-144). 4D PC flow measurements have also been compared with laser Doppler velocimetry (145) and with ultrasound flow measurements in the cranial vessels (146) and the left ventricle (143). Furthermore, pressure gradients derived from 4D PC data sets have been validated with invasive pressure probes (62). Initial studies showed that pressure gradients measured with 4D PC and invasive pressure probes were found to be in strong agreement in the carotid and iliac arteries. Such studies are useful for demonstrating the feasibility of using 4D PC flow techniques clinically.

Navigator-based respiratory gating, as well as continuously adapting respiratory gating with bellows, has allowed for 4D PC data sets to be collected during free breathing (147-149). However, respiratory gating further prolongs the already lengthy acquisitions. Furthermore, the high demands for spatial resolution and large volume coverage needed to assess the complicated anatomy of the abdominal vasculature (Figure 9.1) have hampered the use of 4D PC MRI in the abdomen. Radial undersampling has been promising as a means to overcome these limitations;

radial undersampling has allowed for the assessment of renal flow in addition to the acquisition of high quality PC angiograms without the need for an external contrast agent (147, 148). Given the potential for respiratory motion in abdominal exams, further evaluation is needed to assess the performance of 4D PC techniques in the abdomen.

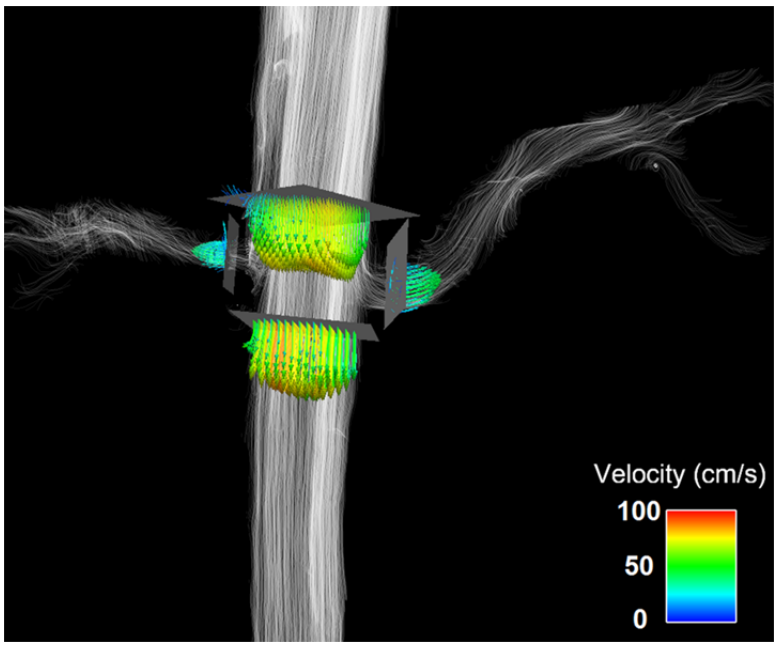

Figure 9.1 Vascular geometry and hemodynamics in the abdominal aorta and renal arteries of a healthy volunteer. 3D stream lines depict the systolic blood flow in the abdominal vasculature. Planes demonstrate velocities in the suprarenal aorta, infrarenal aorta, and left/right renal arteries.

The purpose of this study was to assess and compare the repeatability and internal consistency of 2D and 4D PC flow measurements in the renal arteries and pararenal aorta. To evaluate the internal consistency of flow measurements, flow in the suprarenal aorta (SRA) was compared to the sum of flow measurements in the renal arteries and infrarenal aorta (IRA). Given that no gold standard exists for human in vivo flow measurements, 2D PC flow measurements were used as a reference standard for assessing the 4D PC flow measurements. The comparison of 2D and 4D PC flow measurements is pertinent, given that the placement of

2D slices is subject to user error—as when slices are not placed double-obliquely and when a slice intersects a branching vessel. Since any plane can be extracted retrospectively from the 4D PC data sets, such user errors during scan prescription are mitigated. Furthermore, radially undersampled 4D PC acquisitions may require less total scan time than a series of 2D PC acquisitions, given that an angiogram is needed for 2D slice prescriptions and rest is needed between multiple breath holds. We have also addressed in this study the technical challenges of comparing 2D and 4D PC measurements, given that the frame duration can differ between the acquisitions. Coverage of the cardiac cycle can also differ between the acquisitions, particularly when using the commonly used prospective gating for the 2D PC acquisition and retrospective gating for 4D flow imaging—as with our radial approach. To our knowledge this is the first comparison of 2D and 4D PC flow measurements in the renal/pararenal vasculature and the first assessment of the repeatability of 4D PC flow measurements in any vascular territory.

9.2 Materials and Methods

9.2.1 Subjects

Ten healthy volunteers (6 men, 4 women, ages 24 – 31 years, mean age (±1 SD): 27.4 ± 2.3 years) were included in this HIPAA-compliant study. The study protocol was approved by the local institutional human subjects review board (IRB). Written informed consent was obtained from all subjects prior to inclusion. Subjects refrained from food and drink for a minimum of four hours prior to the MR examination to mitigate the effects of food and drink on blood volume status and hemodynamics. All subjects had a single renal artery supplying each of the kidneys.

9.2.2 MR Imaging

Subjects were imaged on a 3T clinical MR scanner (MR750, GE Healthcare, Waukesha, WI) using a 32-channel torso coil (NeoCoil, Pewaukee, WI). 4D PC data were acquired in the abdomen with the field of view centered on the take-off of the renal arteries. 2D PC slices were acquired in the supra- and infrarenal aorta as well as in each renal artery as shown in Figure 9.1. Slices were prescribed double-obliquely based on reformatted images from a non-contrast MR angiogram (inhance inflow inversion recovery [IFIR]). Planes in the supra- and infrarenal aorta were placed approximately 5-10 mm away from the takeoff of the renal arteries. Planes in the renal arteries were placed 10-15 mm distal to the ostia of the renal arteries. Slice prescription of the 2D PC scans was performed during the acquisition of 4D PC data. After the acquisition of 2D and 4D PC data, the subjects were asked to exit the scanner for five minutes and then re-enter the scanner; the entire procedure described above was then repeated.

2D PC data were acquired with a product 2D sequence with prospective cardiac gating and rectilinear k-space sampling. Typical scan parameters were: VENC = 100 cm/s for renal arteries, VENC = 150 cm/s for the aorta, through-plane velocity encoding, TR/TE/flip = 4.92 ms/2.91 ms/20°, FOV = 34 x 34 cm^2, slice thickness = 6 mm, bandwidth = 488.3 Hertz/pixel, 192 x 140 encoding matrix, breath-holding, temporal resolution = ~20 ms, in-plane spatial resolution = 1.33 x 1.33 mm^2, 25 heart beats required for scan time. 4D PC data were acquired with a dual-echo 5-point velocity encoded sequence with radial undersampling, termed PC VIPR (phase contrast with vastly undersampled isotropic projection reconstruction), in combination with retrospective ECG gating (34, 102, 106). Typical scan parameters were: VENC = 150 cm/s, three-directional velocity encoding, TR/TE/flip = 6.1 ms/2.4 ms/8°, reconstructed imaging

volume = 34 x 34 x 34 cm^3, bandwidth = 488.3 Hertz/pixel, readout = 256 samples, resulting in 1.32 mm isotropic spatial resolution. The acquisition was conducted with an axial excitation and a slab thickness of 16 cm. Respiratory gating with a bellow signal was used with a 50% acceptance window that continuously adapted to the expiration position. The scan time was on the order of 11 minutes. During post-processing, data were reconstructed to 16 time frames with temporal filtering in the RR-cycle (108), similar to view sharing, to yield a temporal resolution of ~71.5 ms on average (depending on the subject's heart rate). This filter provides a temporal window equal to ~71.5 ms in the central spatial frequencies of k-space and a temporal window equal to 5*71.5 = 357.5 ms in the higher frequency regions of k-space.

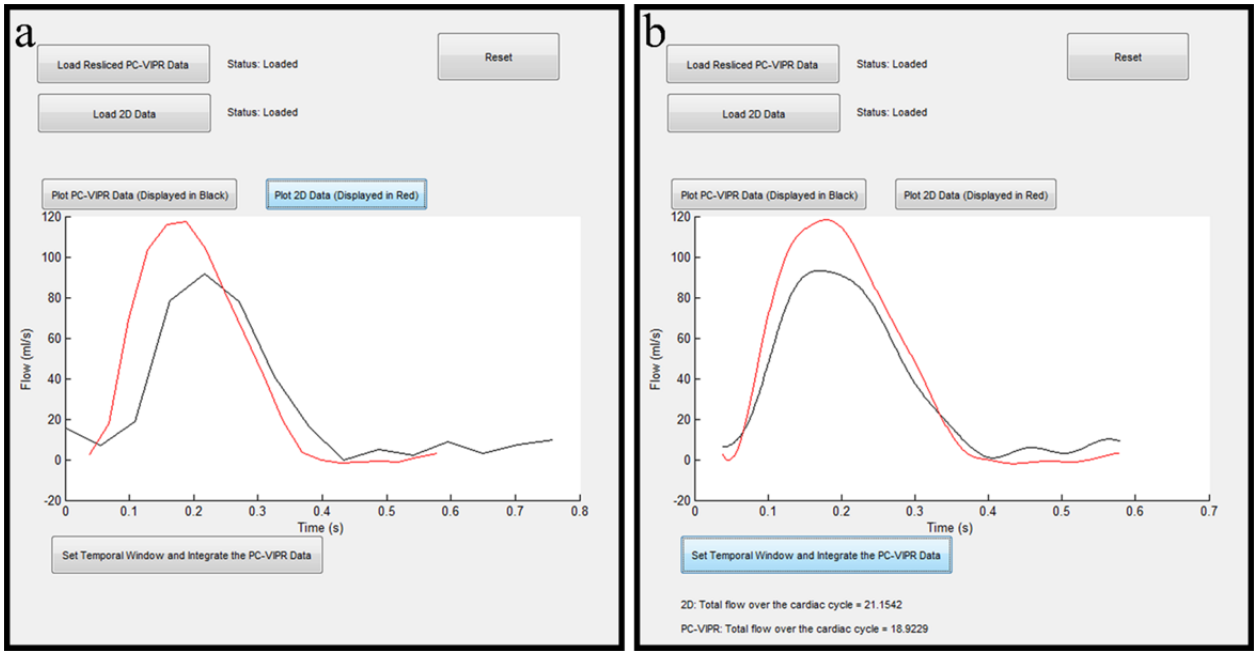

Figure 9.2 Custom MATLAB graphical user interface that allows two waveforms to be loaded (**a**). The two waveforms are aligned via a minimization problem that seeks to reduce the distance between the peaks, points at 50% of maximum, and foot (defined as the intersection between the horizontal axis and a line fitted to data along the upstroke between 20 and 80% of maximum) (**b**).

9.2.3 Data Analysis

Header information from the 2D PC slices were used to extract identical planes from the 4D data sets with the use of a custom MATLAB-based software tool (The MathWorks, Natick, MA). Flow was measured from 2D and 4D slices with the use of a custom MATLAB-based software tool; regions of interest (ROIs) were drawn manually on magnitude images and subsequently copied to the corresponding phase difference images by the software. ROIs were propagated across all time frames and adjusted for any movement of the vessel that may have occurred during the cardiac cycle. Mean flow for each time frame was exported from the software.

The 4D PC acquisition was acquired with retrospective cardiac gating in which the ECG trigger pulses were recorded; trigger pulses did not affect the acquisition view ordering. Therefore, data were acquired over the entire cardiac cycle. In contrast, the 2D acquisition was acquired with prospective cardiac gating, which requires a trigger delay and an arrhythmia rejection window. As a result, the cardiac cycle is not completely sampled with the 2D series of time frames and the resultant flow waveform is incomplete and shorter in duration compared to the 4D flow waveforms. Additionally, the trigger delay of the 2D acquisition, and the difference in temporal resolution between the 2D and 4D techniques, result in the flow waveform being shifted along the cardiac cycle relative to the 4D flow waveform. To compare flow measurements between the 2D and 4D techniques, the flow waveforms should be compared over the same portions of the cardiac cycle. Therefore, to compensate for the abbreviated cardiac cycle and temporal shift of the 2D flow waveform, a custom MATLAB-based software tool was created to align the 2D flow waveform with the 4D flow waveform (Figure 9.2); this waveform

shift was performed by first upsampling both flow waveforms to 400 data points using a cubic spline interpolant. Points at the peak, 50% of maximum, and the foot (defined as the intersection between the x-axis and a line fitted to data along the upstroke between 20 and 80% of maximum) were identified on each flow waveform. A minimization problem was processed with the software tool to minimize the distance between these three waveform points on the 2D and 4D flow waveforms. Once the two waveforms were aligned, the 4D flow waveform was cropped such that the temporal window was the same for both the 2D and 4D flow waveforms. The adjusted waveforms were integrated such that total flow over the cardiac cycle (ml/cardiac cycle) was measured. Differences between in-flow (suprarenal aorta) and out-flow (infrarenal aorta + left renal artery [LRA] + right renal artery [RRA]) were tabulated for the 2D and 4D data.

9.2.4 Statistical Analysis

2D and 4D flow measurements from the two exams in each subject were compared and plotted with Bland-Altman analysis (90). 2D and 4D flow measurements were also compared with a paired Student's t-test ($p < 0.05$) for each individual vessel and for all vessels combined. Stacked box plots were created for the 2D and 4D data from the first exam in each subject to compare in- and out-flow differences. 2D and 4D in- and out-flow differences were compared with an unpaired equal-variance Student's t-test ($p < 0.05$). In- and out-flow were compared with a paired Student's t-test ($p < 0.05$) for both the 2D and 4D approaches. The percent differences between in- and out-flow measurements were computed via the absolute value of the difference between in-flow and out-flow, divided by the mean of the in-flow and out-flow. The overall percent differences for in- and out-flow were reported as the mean ± 1 SD and compared between the 2D and 4D techniques with an unpaired equal-variance Student's t-test. Bland-

Altman plots were created for both the 2D and 4D data to assess the repeatability of flow measurements from the two exams in each subject. The percent differences of repeated 2D and 4D measurements were computed as the absolute value of the difference between the first and second flow measurements in each vessel, divided by the mean of the two flow measurements. The overall percent differences were reported for the 2D and 4D techniques as the mean ± 1 SD. The percent differences were compared between the 2D and 4D techniques with an unpaired equal-variance Student's t-test. A paired Student's t-test ($p < 0.05$) was performed to compare repeated measurements for both the 2D and 4D data. Linear regression of the repeated measurements of 2D and 4D data was performed using data from all four vessels (SRA, IRA, LRA, and RRA); R- and p-values ($p < 0.05$) were recorded.

9.3 Results

For the first examination in each subject, mean (±1 SD) flow measurements from the 2D data were 28.6 ± 6.7, 16.0 ± 3.8, 7.6 ± 2.2, and 8.4 ± 2.0 ml/cardiac cycle for the SRA, IRA, LRA, and RRA vessels, respectively. For the second examination in each subject, mean 2D flow measurements were 30.7 ± 7.3, 17.4 ± 5.0, 7.3 ± 2.1, and 8.0 ± 2.2 ml/cardiac cycle for the four vessels, respectively. Similarly for the first examination in each subject, 4D flow measurements were 26.8 ± 6.9, 15.5 ± 4.5, 5.1 ± 1.5, and 5.9 ± 1.3 ml/cardiac cycle for the SRA, IRA, LRA, and RRA vessels, respectively; for the second examination, measurements averaged 28.8 ± 7.7, 14.5 ± 3.8, 5.4 ± 2.1, and 6.2 ± 1.7 ml/cardiac cycle, respectively. Bland-Altman analysis comparing 2D and 4D flow measurements for all four vessels demonstrated an overall mean flow difference (±2 SD) of 2.0 ± 4.3 ml/cardiac cycle Figure 9.3. Overall, 2D flow measurements were significantly greater than 4D flow measurements ($p = 2.0 \times 10^{-12}$). In each individual vessel,

2D flow measurements were significantly greater than 4D flow measurements for the SRA ($p = 4.89 \times 10^{-3}$), IRA ($p = 9.60 \times 10^{-3}$), LRA ($p = 3.81 \times 10^{-5}$), and RRA ($p = 1.70 \times 10^{-7}$).

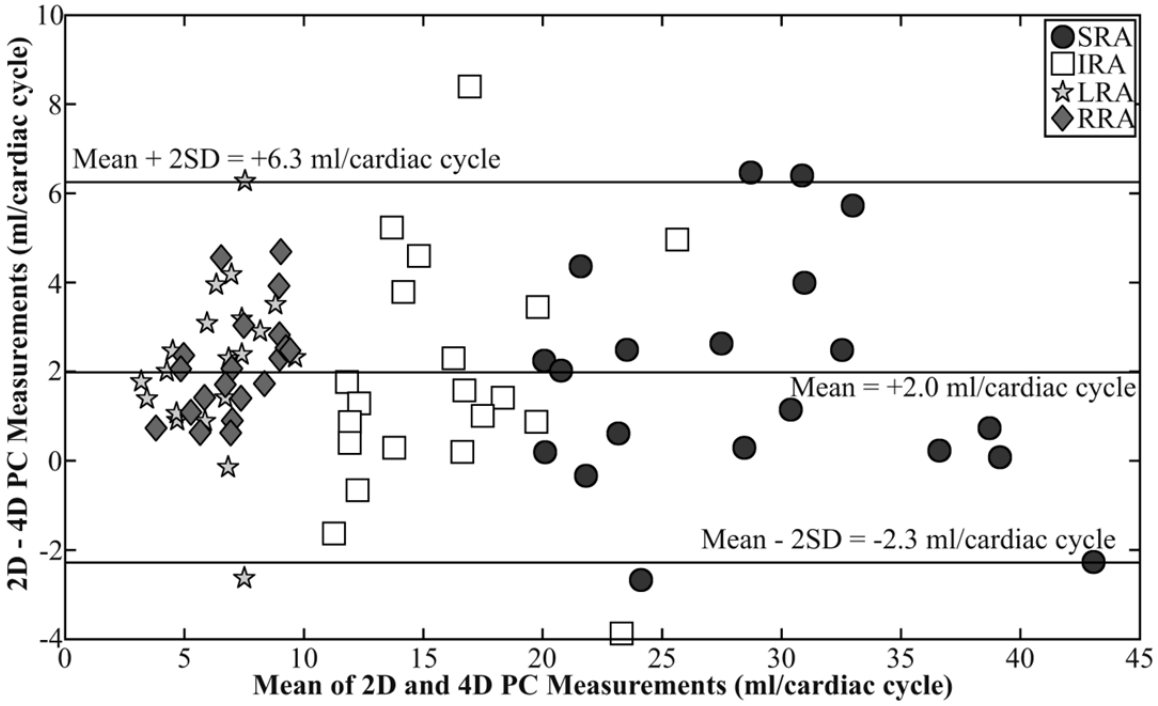

Figure 9.3 Bland-Altman analysis of 2D and 4D phase contrast flow measurements (ml/cardiac cycle) in the supra- and infrarenal aorta and the left and right renal arteries via two examinations in each of ten volunteers. The difference in flow measurements between the 2D and 4D techniques is shown on the ordinate, while the mean of the 2D and 4D flow measurements is shown on the abscissa. As represented by the horizontal lines, the mean (±2 SD) of the difference between 2D and 4D flow measurements was +2.0 ± 2.3 ml/cardiac cycle.

No significant difference was found between 2D (absolute value of mean ± 1 SD: 3.4 ± 2.8 ml/cardiac cycle) and 4D (absolute value of mean ± 1 SD: 3.5 ± 2.7 ml/cardiac cycle) in- and out-flow differences (Figure 9.4; $p = 0.88$). The mean (±1 SD) percent difference for in- and out-flow measurements was 11.3 ± 9.4 % for the 2D data and 12.6 ± 8.8 % for the 4D data. No significant difference was found in the percent difference between the 2D and 4D results ($p = 0.65$). For 2D data, in-flow tended to be less than out-flow measurements, whereas for 4D data, in-flow tended to be greater than out-flow measurements. Out-flow measurements were

significantly greater than in-flow measurements with the 2D technique ($p = 0.003$); no significant difference was found between in-flow and out-flow measurements for the 4D technique ($p = 0.13$).

For repeatability, Bland Altman analysis in all four vessels demonstrated a mean difference (±2 SD) of 0.8 ± 6.2 ml/cardiac cycle for 2D data (Figure 9.5a) and a mean difference (±2 SD) of 0.4 ± 6.2 ml/cardiac cycle for the 4D data (Figure 9.5b). The mean (±1 SD) percent difference for repeated flow measurements was 14.0 ± 12.5 % for the 2D data and 15.1 ± 15.6 % for the 4D data. No significant difference was found in the percent difference between the 2D and 4D results ($p = 0.72$). For all four vessels, no significant differences were found in repeated measurements of 2D ($p = 0.15$) or 4D ($p = 0.39$) data. For repeated measurements in each individual vessel, significant differences were found in neither the 2D (SRA: $p = 0.06$; IRA: $p = 0.36$; LRA: $p = 0.60$; RRA: $p = 0.13$) nor the 4D data (SRA: $p = 0.12$; IRA: $p = 0.48$; LRA: $p = 0.47$; RRA: $p = 0.36$). Linear regression demonstrated strong agreement between repeated measurements for both 2D ($R = 0.96$, $p = 2.6 \times 10^{-22}$) and 4D ($R = 0.96$, $p = 9.9 \times 10^{-22}$) data.

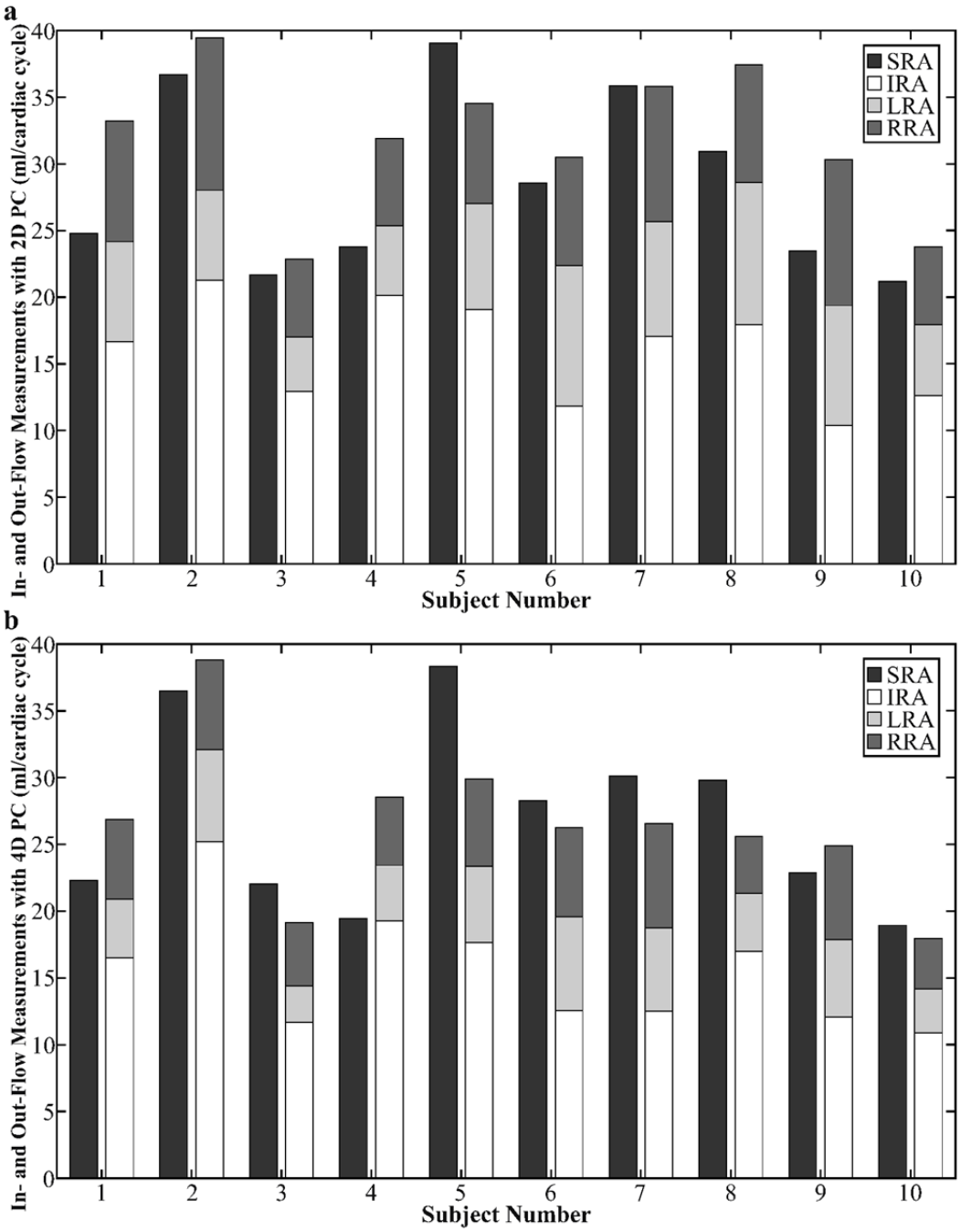

Figure 9.4 Stacked bar graphs showing in-flow (suprarenal aorta [SRA]) and out-flow (infrarenal aorta [IRA] + left renal artery [LRA] + right renal artery [RRA]) in ten volunteers as measured with 2D (a) and 4D (b) phase contrast techniques. Data shown are from the first exam in each subject.

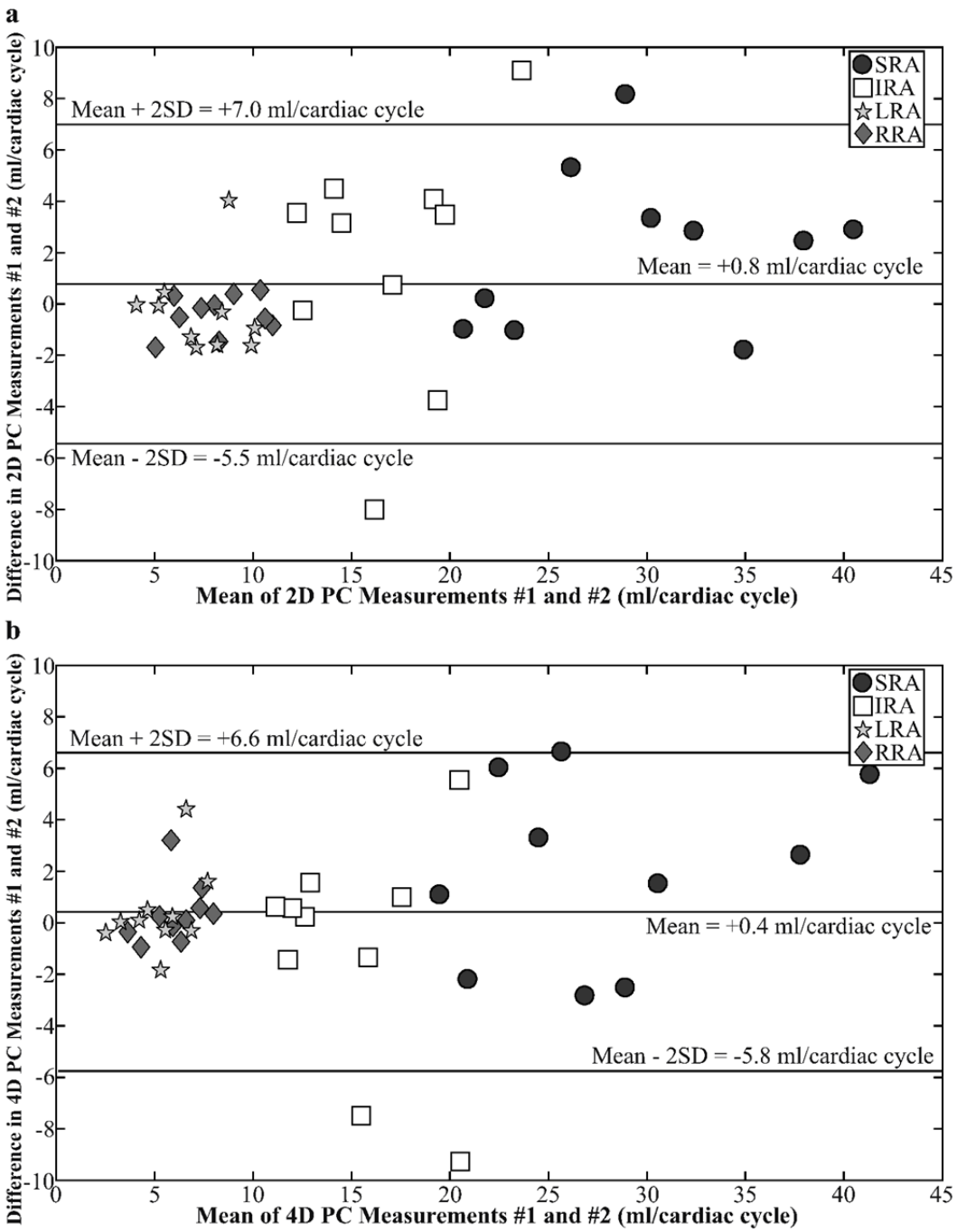

Figure 9.5 Bland-Altman analysis of the repeatability of 2D (a) and 4D (b) phase contrast flow measurements (ml/cardiac cycle) in the supra- and infrarenal aorta and the left and right renal arteries of ten volunteers. The difference in flow measurements between the first and second examinations is shown on the ordinate, while the mean of the first and second flow measurements is shown on the abscissa. As represented by the horizontal lines, the mean (±2 SD) of the difference between repeated 2D flow measurements was +0.8 ± 6.2 ml/cardiac cycle and for repeated 4D flow measurements was +0.4 ± 6.2 ml/cardiac cycle.

9.4 Discussion

The results of this study demonstrate the repeatability of flow measurements in the abdominal vasculature, as well as the internal consistency of in- and out-flow measurements in the renal arteries and pararenal aorta, with both the 2D and 4D PC techniques. For repeatability, 2D data demonstrated a mean difference (±2 SD) of 0.8 ± 6.2 ml/cardiac cycle and 0.4 ± 6.2 ml/cardiac cycle for 4D data. No significant differences were found ($p > 0.05$) and correlation coefficients showed very strong agreement ($R = 0.96$) in repeated measurements of 2D and 4D data. However, repeated 2D and 4D flow measurements varied an average of 14-15%. For measurements of internal consistency, differences were found between in- and out-flow (2D: 3.4 ± 2.8 ml/cardiac cycle; 4D: 3.5 ± 2.7 ml/cardiac cycle); no significant differences were found in comparing 2D and 4D in- and out-flow measurements. In- and out-flow varied by 11.3 ± 9.4 % for the 2D data and 12.6 ± 8.8 % for the 4D data. Out-flow measurements were significantly greater than in-flow measurements with the 2D technique ($p = 0.003$); no significant difference was found between in-flow and out-flow measurements for the 4D technique ($p = 0.13$). These findings demonstrate stronger repeatability and internal consistency for the 2D and 4D techniques than reported in the study by Bax et al. (150). Bax et al. used a retrospectively cardiac gated 2D approach with free breathing to measure repeatability and in-/out-flow differences in the renal arteries and pararenal aorta. Blurring secondary to respiratory motion led to a lesser degree of repeatability and internal consistency, as well as a limited technical success rate (78 - 85%) (150).

Flow measurements from the 4D approach were significantly lower than flow measurements from the 2D approach ($p = 2.0 \times 10^{-12}$), which is consistent with previous studies

comparing 2D and 4D flow measurements (103, 151). The lower temporal resolution of the 4D approach (~71.5 ms) compared to the 2D approach (~20 ms) may explain these differences in flow measurements. The temporal filter used in the reconstruction of 4D data creates temporal blurring of higher spatial frequencies; the lower temporal resolution with the 4D approach will more often fail to sample the true peak systolic flow and therefore tend to underestimate the total flow over the cardiac cycle. Additionally, the 4D acquisition lasts more than 10 minutes; thereby, data are combined from many heartbeats and may include variations in the length of the cardiac cycle. Therefore, the scan duration may also contribute to the temporal blurring effect and lead to a decrease in peak flow. The in-plane spatial resolution of the 2D and 4D approaches was identical; however, the 4D approach provides isotropic spatial resolution, and therefore, the slice thickness of extracted 4D slices (1.32 mm) is less than the 2D slice thickness (6 mm). Out-of-plane partial voluming is more likely to have contributed to errors in flow for the 2D technique than for the 4D technique. Furthermore, flow measurements from the 4D data were acquired on planes extracted from the imaging volume. The extraction of a 2D plane from a 4D volume could lead to interpolation effects that affect flow measurements. Nevertheless, there was no non-invasive gold standard to demonstrate whether either the 2D or 4D flow values were more accurate compared to the true flow rates within the vessels. The extraction of planes from the 4D data set is potentially advantageous, as it does not rely on proper slice prescription during the acquisition. Slice prescription can be problematic with 2D acquisitions, since it takes time to acquire proper localizers and prescribe slices double-obliquely; 2D slices may also intersect branching vessels. For example, prescription of a suprarenal aortic slice without intersecting the superior mesenteric artery is difficult. Hence, the selection of slices retrospectively is a

significant advantage of 4D PC data sets. Finally, the 4D PC acquisition required 11 minutes of scan time. In comparison the series of four 2D PC slices requires ~30 seconds per scan, with a minute of rest between each scan, as well as a five-minute non-contrast angiogram and up to five minutes for prescribing the four slices. Therefore, the four 2D PC slices require 10-15 minutes of scan time. In a time period approximately equivalent to a series of 2D PC slices, the radially undersampled 4D PC acquisition has the ability to provide comparable flow measurements, less error due to slice prescription, no breath holding, a more complete flow waveform via the use of retrospective cardiac gating, a non-contrast-enhanced angiogram, and the potential for deriving additional parameters from the volume data set, such as wall shear stress, pulse wave velocity, and pressure gradients, which require volumetric three-directional velocity information.

There are several limitations to this study. The 2D PC acquisition utilized prospective cardiac gating, whereas the 4D technique employed a retrospective cardiac gating technique. The prospectively gated 2D technique was selected because of its clinical use and the ability to scan within the time of a breath hold. The retrospectively gated 2D PC technique available on our MR scanner utilized rectilinear k-space sampling and was unfeasible within the time of a breath hold. Therefore, it was the priority of this study to use a clinically available 2D PC technique and one that could be performed within the time of a breath hold. Despite the difference in gating technique used in our 2D and 4D PC methods, we developed a tool to match the 2D and 4D flow waveforms. On another point, the repeatability of flow measurements was only assessed on back-to-back MR examinations. In addition to the study of back-to-back MR examinations, it would be advantageous to investigate the repeatability of flow measurements for MR examinations performed on separate days. As such, physiological variations in flow

measurements could be assessed. Ideally such a study would require repeated MR examinations on both the same day as well as on each of two subsequent days so that variations due to the technique could be adjusted for in the evaluation of physiological variations in flow. Furthermore, such a study would require the withholding of food and drink for four hours and for the MR exam to be performed at the same time of day each day to account for diurnal variations in hemodynamics. Finally, it should be noted that it may not be possible to generalize the results of this study to other 4D techniques, as a radially undersampled 4D technique was used in this study. While the 4D technique used respiratory gating with bellows to compensate for respiratory motion, radially sampled sequences are inherently less sensitive to respiratory motion than acquisitions with rectilinear k-space sampling. The fact that each projection traverses the center of k-space mitigates the effects of respiratory motion.

In conclusion, the 2D and 4D PC acquisitions provided a promising means of measuring flow in the renal arteries and pararenal aorta. Both techniques demonstrated repeatability on the order of 14-15% and strong internal consistency of flow measurements. 4D PC flow measurements were significantly lower than 2D PC flow measurements. Further studies comparing the 2D and 4D PC acquisitions is warranted, including studies to assess the effects of prospective and retrospective cardiac gating, to evaluate the 2D and 4D approaches with matching temporal resolution, and to determine the repeatability of flow measurements on inter-day MR examinations.

Chapter 10 Evaluation of Atherosclerosis in Swine

PURPOSE: To assess measurements of pulse wave velocity (PWV) and wall shear stress (WSS) in a swine model of atherosclerosis.

MATERIALS AND METHODS: Five swine with a balloon catheter-induced injury to the abdominal aorta and six uninjured swine were evaluated with a 4D phase contrast (PC) MRI acquisition, as well as with 2D PC acquisitions. PWV values were computed from the 2D and 4D PC techniques, compared between the injured and uninjured swine, and were validated against gold standard pressure probe-based PWV measurements. WSS values were also computed from the 4D PC MRI technique and compared between groups and between regions with and without balloon catheter-induced injury.

RESULTS: No significant differences were found in PWV between the 2D and 4D PC MRI measurements and the pressure probe-based measurements. PWV values were not significantly different between the injured and uninjured groups, although values from the 4D PC MR technique ($p = 0.08$) and the pressure probes (0.09) approached statistical significance. No significant differences were found for WSS values between the injured and uninjured groups. No significant differences were found between regions of injury and non-injury in the group of injured swine, although WSS values were significantly lower in downstream regions of uninjured swine compared to upstream regions.

CONCLUSION: The 4D PC MRI technique provided a promising means of evaluating PWV in a swine model of atherosclerosis. More subjects are necessary to establish statistical significance.

10.1 Introduction

Currently, the standard method of assessing a patient's risk of a cardiovascular event is with the computation of a Framingham Risk Score (FRS) (5). While studies have shown that intima-media thickness measurements with ultrasound provide an insignificant improvement to the FRS (18), the evaluation of the coronary calcium score via computed tomography has demonstrated a significant improvement to risk assessment beyond that provided by the FRS alone (15). However, the greatest concern regarding the evaluation of coronary calcium score is the exposure of patients to ionizing radiation. Since studies have demonstrated that an imaging-based diagnosis of atherosclerosis improves patient compliance and reinforces risk-reducing behaviors (152, 153), it would be prudent to develop an imaging-based biomarker that assists in cardiovascular risk assessment without the use of ionizing radiation.

In recent years a number of MRI-based biomarkers of atherosclerosis have been explored, including wall shear stress (WSS) and pulse wave velocity (PWV). Studies have shown that areas of low WSS serve as a predictive biomarker for the occurrence of atherosclerotic plaques (37, 116-118). WSS is a measure of drag forces on vessel walls; it is hypothesized that abnormal blood flow patterns, and in turn insufficient stress, lead to dysfunction of the endothelium (59). Endothelial dysfunction leads to vascular remodeling, such as adaptive intimal thickening, and may progress to advanced atherosclerotic lesions, especially in the presence of hyperlipidemia and hypertension (118). An elevated PWV is another MRI-based biomarker of atherosclerosis (93). As arteries are stiffened by the growth of atherosclerotic plaques, the pulse wave of blood down the aorta is accelerated because of the loss of elastic recoil in the vessel (92).

Studies on MRI-based WSS and PWV measurements have been limited. Previous studies on WSS used techniques that were limited in spatiotemporal resolution (60, 154), provided limited anatomic coverage (45, 121), and/or relied on semiquantitative descriptions of 3D flow patterns (126-130). Since long scan times are required for large coverage and high spatiotemporal resolution, a previous study on PWV sacrificed one or more of these parameters to achieve what they considered a clinically acceptable scan time of 15-20 minutes (98). Because WSS is derived from the small velocity gradient at the vessel wall, high spatial resolution is needed for accurate measurements. Since PWV is derived from the rapidly propagating wave of blood down the aorta, high temporal resolution is needed to capture accurately the temporal dynamics of this movement. There is a dire need for an MRI acquisition that provides high spatial and temporal resolution as well as good anatomic coverage.

The purpose of this study was to evaluate the measurements of WSS and PWV in a swine model of familial hypercholesterolemia (FH) with the use of a radially undersampled 4D phase contrast (PC) MRI technique that provides high spatiotemporal resolution, large anatomic coverage, and a scan time on the order of ten minutes. Five FH swine with, and six FH swine without, a balloon catheter-induced injury to the abdominal aorta were evaluated. WSS was assessed with the 4D PC MRI technique; PWV was computed with 2D and 4D PC MRI and validated with fiber optic pressure probes. We hypothesized that PWV would be elevated in the injured group and that injured areas would have greater WSS than uninjured areas. To our knowledge this is the first study of simultaneous MRI-derived WSS and PWV measurements and the first validation study of 4D PC MRI-based measurements of PWV. Familial hypercholesterolemias are a group of genetic defects that lead to significantly elevated levels of

low-density lipoprotein (LDL) cholesterol. Due to their elevated LDL levels, FH patients are at an increased risk of developing atherosclerosis and adverse cardiovascular events (19). Therefore, FH serves as an excellent and predictable model for assessing biomarkers of atherosclerosis.

10.2 Materials and Methods

10.2.1 Animal Population and Injury

Five swine (one male; four females; mean age ± 1SD = 8.5 ± 0.6 months; mean mass ± 1SD = 45.0 ± 5.5 kg; mean heart rate ± 1SD = 85 ± 16 bpm) with and six swine (three males; three females; mean age ± 1SD = 12.7 ± 7.2 months; mean mass ± 1SD = 50.6 ± 25.1 kg; mean heart rate ± 1SD = 91 ± 18 bpm) without an angioplasty balloon catheter-induced vascular injury were recruited into the study. The non-injured group was divided into two subgroups, with 3 animals near six months of age (two males; one female; mean age ± 1SD = 6.2 ± 0.3 months; mean mass ± 1SD = 28.4 ± 3.9 kg; mean heart rate ± 1SD = 91 ± 5 bpm) and three animals near eighteen months of age (one male; two females; mean age ± 1SD = 19.2 ± 1.6 months; mean mass ± 1SD = 72.9 ± 8.5 kg; mean heart rate ± 1SD = 91 ± 27 bpm). All swine were heterozygous for familial hypercholesterolemia. The study protocol was approved by the local Animal Care and Use Committee.

Prior to the injury procedure swine were fasted for 24 hours. Swine were pretreated with dantrolene (4.4 mg/kg) orally to prevent hyperthermia secondary to porcine stress syndrome (155). Animals were induced with telazol (1.6 mg/kg) and xylazine (1.4 mg/kg) intramuscularly. Atropine (0.05 mg/kg) was administered intramuscularly to reduce salivary secretions and

decrease gastric motility. Subsequently, the swine were intubated, shaven, scrubbed, and draped for surgery, and ventilated with 1.5% isoflurane (400 cc/breath; 7 breaths/min). Balloon catheter-induced injury in the vasculature was performed in the supra- and infrarenal aorta, as well as the left femoral artery (Figure 10.1) via initial placement of a sheath in one of the carotid arteries. Placement of the balloon catheters was performed via fluoroscopic guidance; injury was performed via over-inflation of the balloon and via retracting and advancing the balloon >5 times. A 7x2 and a 12x4 angiography balloon were used in the femoral artery and aorta, respectively.

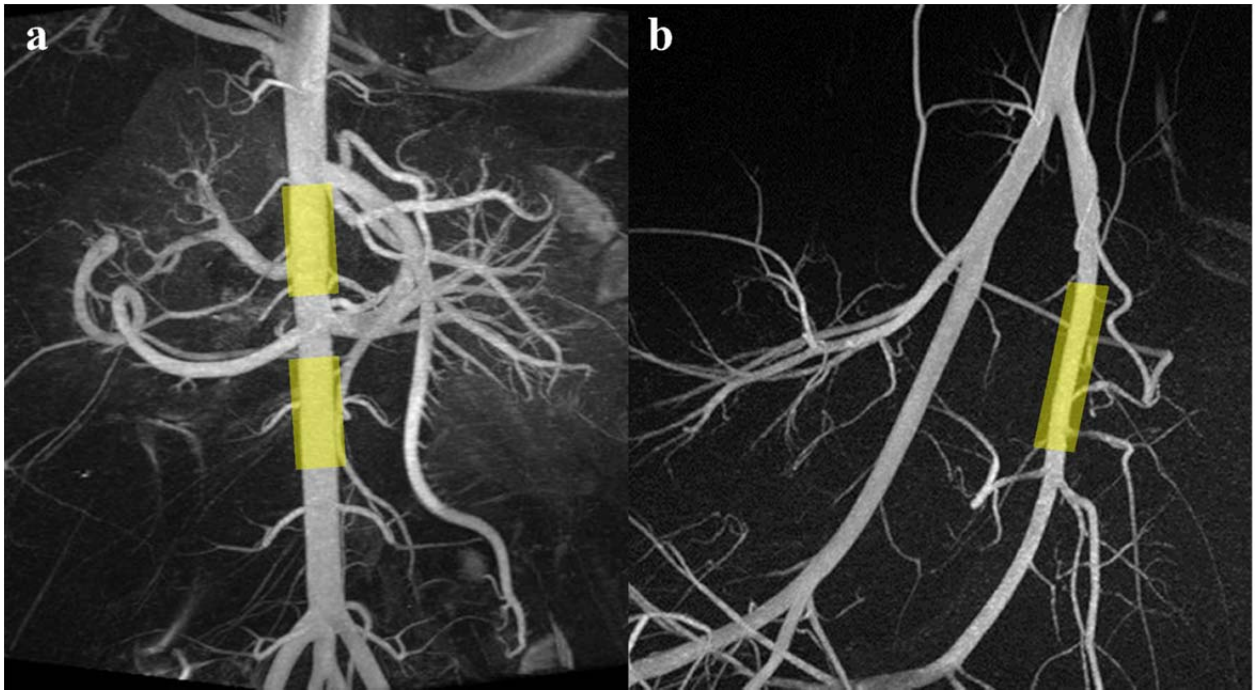

Figure 10.1 Angiograms from C-arm computed tomography in the abdominal aorta (**a**) and iliac/femoral vasculature (**b**). In five swine injury was created in the supra- and infrarenal aorta, as well as the left common femoral artery, as indicated by boxes shaded in yellow.

Subsequent to the injury the swine were recovered and maintained on a 20% fat and 2% cholesterol diet for ~4 weeks. Following this time period the animals were returned for MR imaging. At this time point prophylaxis with dantrolene and induction with xylazine and telazol

were performed as described above. Anesthetic maintenance was performed with propofol (12 mg/kg/hr) rather than isoflurane, given that volatile anesthetics, such as isoflurane, have a suppressive effect on hemodynamics (156, 157). Swine were then intubated and ventilated (700 cc/breath; 7 breaths/min). For the six uninjured swine, this same induction and anesthesia procedure was performed. The uninjured swine, up to 24 hours prior to the procedure, had been maintained on a standard diet. After anesthetization and prior to each MR study, 3D digital subtraction angiography, ultrasound, and pressure probe-based pulse wave velocity measurements were performed on each animal as described in the sections below.

10.2.2 C-Arm Computed Tomography

3D digital subtraction angiographic (DSA) images (Figure 10.1) were obtained on each animal with a C-arm computed tomography (CT) system (Artis zeego; Siemens, Erlangen, Germany). Image acquisition required two 5-second rotations—one rotation for a mask and the other rotation with the injection of iopamidol (370 mgI/ml; Isovue 370; Bracco Diagnostics, Princeton, New Jersey) into the jugular vein following an appropriate delay time. Reconstruction of the data was performed as previously described (158, 159). The acquisition was performed for both the abdominal aorta and femoral vasculature (Figure 10.1).

10.2.3 Ultrasound

Ultrasound-based strain estimation (160) was performed prior to each MR study in the injured femoral arteries. Data were collected on a Siemens Anteres (Mountain View, CA, USA) ultrasound system with a VFX13-5 transducer excited at 11.4 MHz. RF data were collected at a sampling rate of 40 MHz, depth of 4 cm, and a 27 s^{-1} frame rate. As described by McCormick et al. (160), the RF data are used to create a series of displacement images via algorithms for frame

skip and displacement interpolation. Regions of interest are drawn on B-mode images created from the RF data to identify regions for which strain is estimated with a modified least-squares approach (161). This analysis was performed by members of the University of Wisconsin Medical Physics Ultrasound Group.

10.2.4 Pressure Probes

Two fiber optic pressure probes (opSens, Quebec, Quebec, Canada) with the Fabry-Perot interferometer configuration (162) were bound together with Tegaderm (3M, St. Paul, MN, USA); the tips of the two probes were separated by a distance of 10 cm. These probes sense pressure via a microelectromechanical system (MEMS), which houses a diaphragm that deflects in proportion to the amount of strain imparted on it.

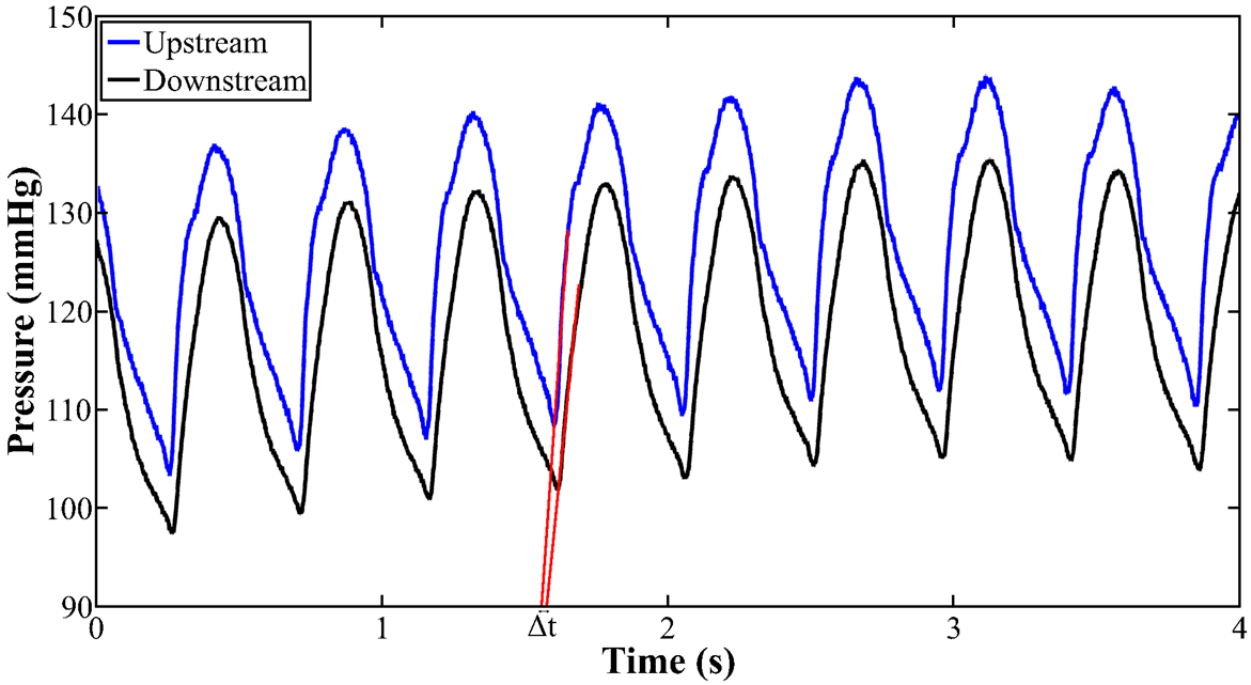

Figure 10.2 Pressure waveforms in the abdominal aorta of a pig; two probes are bound together and separated by a distance of 10 cm, thus providing two pressure waveforms (one upstream and one downstream. A linear line (red line) can be fit to the upstroke of a set of waveforms to find the temporal distance separating the two waveforms (Δt).

The probes were advanced through the sheath placed in the carotid artery and centered over the renal arteries; placement was performed with fluoroscopic guidance and the simultaneous advancement of a radiopaque catheter that was retracted following placement. Pressure waveforms over the cardiac cycle were obtained from both probes simultaneously with a sampling rate of 1 kHz (Figure 10.2).

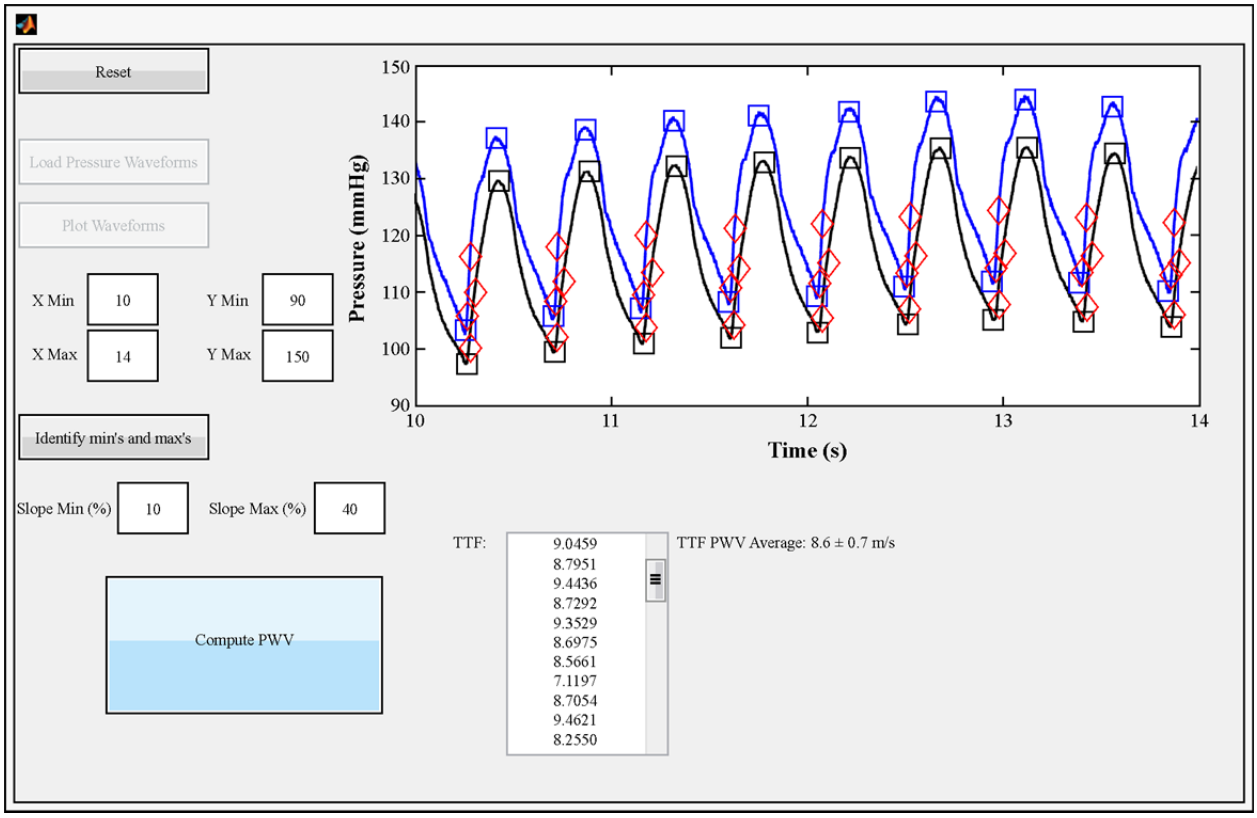

Figure 10.3 Graphical user interface for a tool that loads pressure probe data and automatically detects the peaks and valleys for each cycle of the waveform (blue and black squares). From the peaks the points at 10 and 40% of maximum (red diamonds) are identified; data between these points are used to fit a line to the upstroke of each cycle. The temporal difference between the two waveforms for each cycle is used to compute pulse wave velocity (PWV). The PWV of every cycle is listed in the scroll box and listed as an average in the adjoining text box.

The temporal distance between the two flow waveforms can be determined by fitting a line to data points between 10 and 40% of the maximum value of any one cycle of the

waveforms. Note that this range of value (10-40%) is different than that used for pulse wave velocity (PWV) measurements via flow waveforms (**Chapter 7**); 10-40% was used because the shape of the pressure waveform is different than a flow waveform and using 20-80% would lead to an improper fit of the waveforms' upstroke. With a line fitted to the upstroke of each waveform, the foot can be found via the intersection of this line with the horizontal axis. The time difference between the feet of the two pressure waveforms provides the temporal distance, Δt. Given that the probes are separated by 10 cm, we can compute PWV by dividing the distance by Δt. While in magnetic resonance imaging a single flow waveform is provided by any one acquisition, the high temporal resolution and numerous waveforms provided by the pressure probes can provide an individual PWV for every cycle recorded from the pressure probes. Thus, PWV can be recorded as the average value computed over numerous cardiac cycles. A MATLAB-based software tool (The MathWorks, Natick, MA, USA) was developed to automatically identify the waveform peaks within every cardiac cycle in the pressure waveform and to automatically compute and average the PWV from all cardiac cycles (Figure 10.3).

10.2.5 Magnetic Resonance Imaging

Swine were imaged on a 3T clinical MR scanner (MR750, GE Healthcare, Waukesha, WI) using a 32-channel torso coil (NeoCoil, Pewaukee, WI). A contrast-enhanced angiogram was acquired in the abdominal vasculature; scan parameters were: 1.5x dose (0.15 mmol/kg) gadobenate dimeglumine at an injection rate of 3 ml/s and a 20 ml flush, TR/TE/flip = 3.52 ms/1.16 ms/28°, FOV = 44 x 44 cm^2, slice thickness = 1.8 mm with 0.9 mm spacing between slices, bandwidth = 325.5 Hertz/pixel, 512 x 512 encoding matrix, breath-holding, in-plane

spatial resolution = 0.86 x 0.86 mm^2. Reformatted images from the angiogram were used to place double oblique 2D PC slices.

2D PC data were acquired with a product sequence with prospective cardiac gating and rectilinear k-space sampling. Five evenly spaced slices were prescribed along the lower thoracic and abdominal aorta using reformatted images from the contrast-enhanced angiogram. Typical scan parameters were: VENC = 150 cm/s, through-plane velocity encoding, TR/TE/flip = 6.22 ms/3.45 ms/20°, FOV = 34 x 34 cm^2, slice thickness = 6 mm, bandwidth = 244 Hertz/pixel, 256 x 256 encoding matrix, breath-holding, temporal resolution = ~25 ms, in-plane spatial resolution = 1.33 x 1.33 mm^2.

2D PC data were also acquired with a custom sequence with retrospective cardiac gating and radial k-space sampling. Five evenly spaced slices were placed using the identical slice prescriptions from the product 2D PC data above. Typical scan parameters were: VENC = 150 cm/s, through-plane velocity encoding, TR/TE/flip = 6.3 ms/3.5 ms/15°, FOV = 32 x 32 cm^2, slice thickness = 5 mm, bandwidth = 488 Hertz/pixel, 256 x 256 encoding matrix, breath-holding, temporal resolution = ~12 ms, in-plane spatial resolution = 1.25 x 1.25 mm^2.

4D PC data (PC VIPR) were acquired with a dual-echo 5-point velocity encoded sequence with radial undersampling in combination with retrospective ECG gating (34, 102, 106). Contrast was injected prior to the 4D PC acquisition with the same protocol used for the angiogram above. 4D PC data were acquired in the abdomen with the field of view centered on the take-off of the renal arteries. Typical scan parameters were: VENC = 150 cm/s, three-directional velocity encoding, TR/TE/flip = 6.1 ms/2.4 ms/8°, reconstructed imaging volume =

34 x 34 x 34 cm^3, bandwidth = 488.3 Hertz/pixel, readout = 256 samples, resulting in 1.32 mm isotropic spatial resolution. The acquisition was conducted with an axial excitation and a slab thickness of 16 cm. Respiratory gating with a bellow signal was used with a 50% acceptance window that continuously adapted to the expiration position. The scan time was on the order of 11 minutes. During post-processing, data were reconstructed into cardiac phases with a duration of 5*TR with temporal filtering in the RR-cycle (108), similar to view sharing, to yield a temporal resolution of ~31 ms on average. This filter provides a temporal window equal to ~31 ms in the central spatial frequencies of k-space and a temporal window equal to 5*31 = 155 ms in the higher frequency regions of k-space.

10.2.6 Histology

After the MR exam animals were euthanized with Beuthanasia-D (0.2 ml/kg) intravenously. Subsequently the femoral and aortic vessels were localized, dissected, removed, and placed in formalin; the tissue samples were not pressure perfused. Tissue sections were stained with haematoxylin and eosin.

10.2.7 Data Analysis

Pulse wave velocity was measured from the 4D PC and radial and Cartesian 2D PC sets of data, as described in **Chapter 7**. Wall shear stress was measured in the abdominal aorta from the 4D PC data as described in **Chapter 8** with values averaged over three vertical segments. The upper and lower segments represented the injured areas in the supra- and infrarenal aorta; the middle segment represented the injured area proximal to the ostia of the renal arteries.

10.2.8 Statistical Analysis

PWV measurements from the pressure probes, 4D PC, and radial and Cartesian 2D PC data sets were compared between the injured and uninjured animals with a non-paired equal-variance Student's t-test ($p < 0.05$). PWV measurements from the 4D PC and radial and Cartesian 2D PC data sets were compared to the gold standard pressure probe-based PWV measurements with paired Student's t-tests ($p < 0.05$) and Bland-Altman analysis (90).

Average WSS measurements were evaluated within the uninjured and injured groups via paired Student's t-tests to compare the upper versus the middle segments, the middle versus the lower segments, and the upper versus the lower segments. Unpaired equal-variance Student's t-tests were also used to compare WSS measurements for each the upper, middle, and lower segments between the injured and uninjured groups.

Linear regression was used to assess how PWV was related to group (injured versus uninjured), gender, age, heart rate, mass, and vessel diameter. Univariate models were fitted to each variable; if the p-value from the F-test was significant, the variable was entered into a multivariable model. Separate analyses were performed for each of the three PWV methods (Cartesian 2D PC, radial 2D PC, 4D PC). The same analysis was repeated for upper, middle, and lower WSS. $p < 0.05$ (one-sided) was considered as statistically significant. p-values were not adjusted for multiple testing. The analysis was done in R 2.12.2 (R Development Core Team 2009).

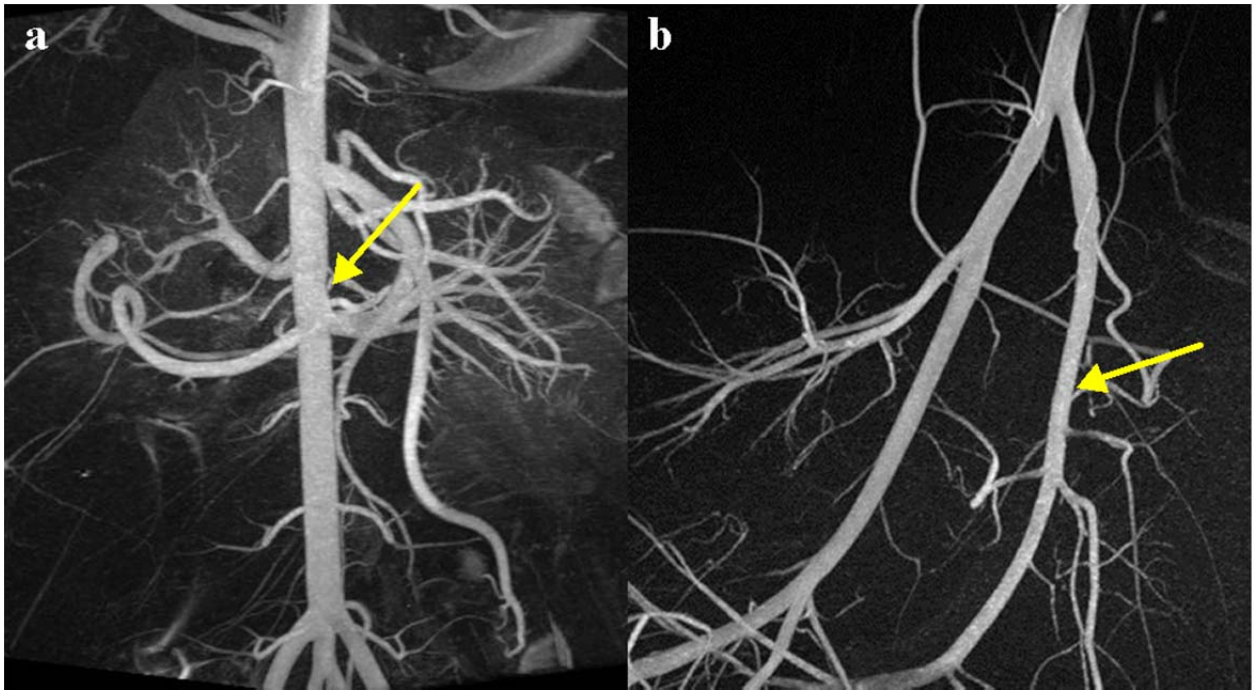

Figure 10.4 Angiograms from C-arm computed tomography in the abdominal aorta (**a**) and iliac/femoral vasculature (**b**). In five swine injury was created in the supra- and infrarenal aorta, as well as the left common femoral artery. Minimal changes to vascular integrity are visible via the slight irregularities indicated by the yellow arrows.

10.3 Results

10.3.1 C-Arm Computed Tomography

C-arm computed tomography provided high resolution images of the vasculature. For the injured animals, most angiograms were unremarkable and therefore no stenoses or irregularities were identified. For the worst case, as shown in Figure 10.4, slight irregularities could be appreciated in the areas of injury, especially in the suprarenal abdominal aorta and the left femoral artery. These images confirmed that none of the animals had cardiovascular disease that significantly intruded into the vascular lumen.

10.3.2 Ultrasound

Initial results in imaging strain in the femoral arteries of injured swine demonstrated elevated strain in regions of injury (Figure 10.5). Such elevated strain is indicative of a vessel wall with greater compressibility, which may be representative of early atherosclerotic plaque.

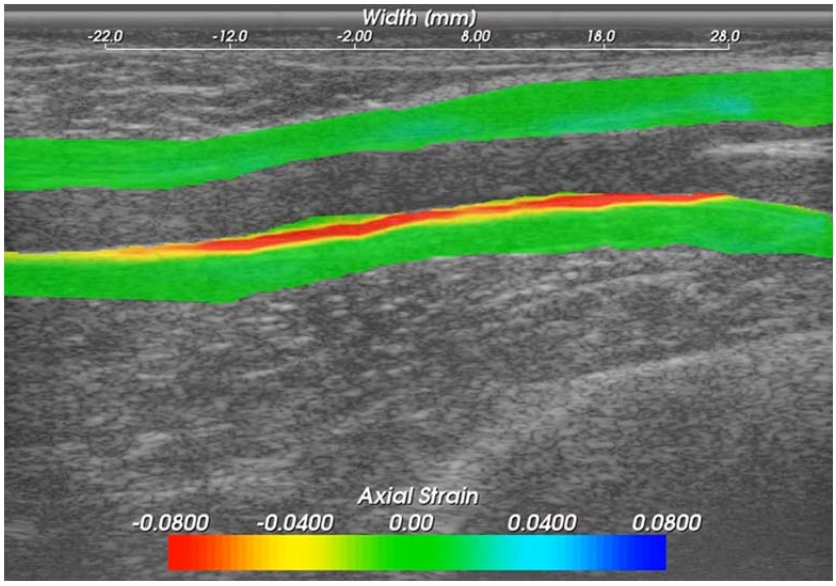

Figure 10.5 Ultrasound-based axial strain images of an injured femoral artery in a pig. The femoral artery is between the two green regions. Elevated strain (in red) represents a more compressible arterial wall. Image courtesy of Tomy Varghese, PhD.

10.3.3 Magnetic Resonance Imaging and Pressure Probes

Figure 10.6 demonstrates the PWV results as measured from pressure probes, 4D PC MRI, and radial and Cartesian 2D PC MRI. Note that the pressure probe system was not available until pig #4, that the acquisition of 2D PC data failed in pig #1 due to aliasing, and that flow waveforms from the Cartesian 2D PC data for pig #7 were missing the systolic upstroke secondary to prospective cardiac gating, making standard PWV analysis impossible.

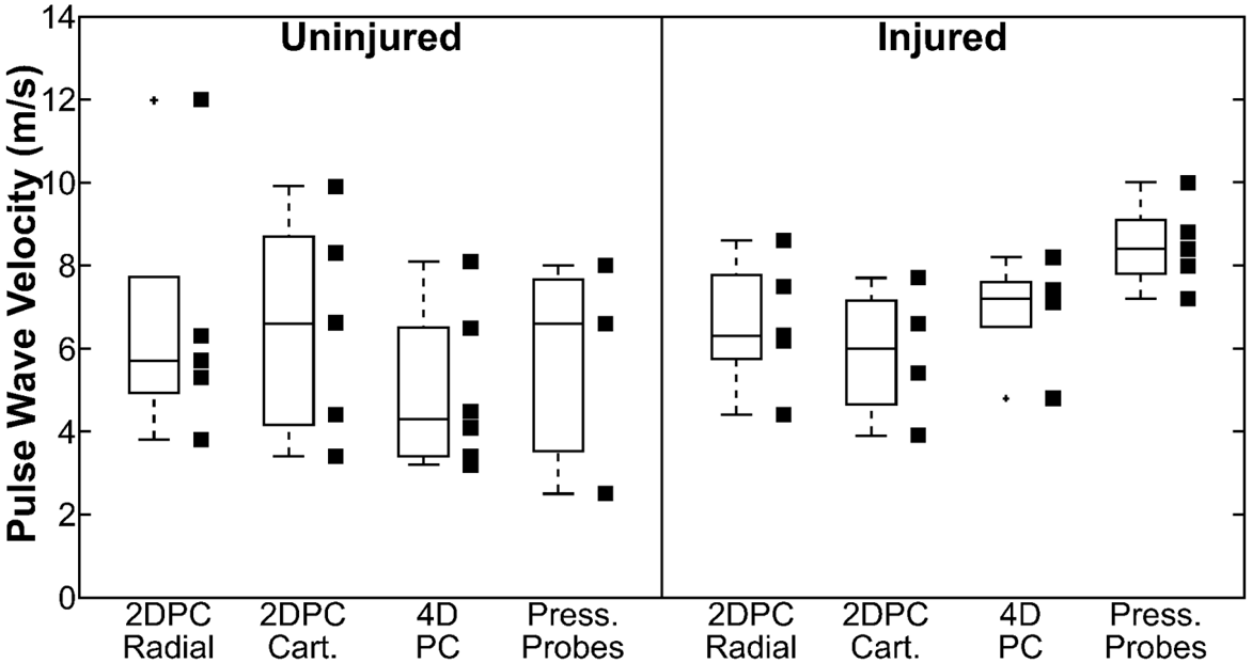

Figure 10.6 Box and scatter plots of global aortic pulse wave velocity measurements derived from pressure probes, 4D PC MRI, and radial and Cartesian 2D PC MRI in six uninjured and five injured swine.

For the uninjured group, PWV averaged 5.7 ± 2.9 m/s for pressure probe data, 5.0 ± 1.9 m/s for 4D PC MRI data, 6.6 ± 3.1 m/s for radial 2D PC MRI data, and 6.5 ± 2.7 m/s for Cartesian 2D PC MRI data. For the injured group, PWV averaged 8.5 ± 1.0 m/s for pressure probe data, 6.9 ± 1.3 m/s for 4D PC MRI data, 6.6 ± 1.6 for radial 2D PC MRI data, and 5.9 ± 1.6 m/s for Cartesian 2D PC MRI data. No significant difference was found between injured versus uninjured PWV values for the radial 2D PC MRI data ($p = 0.99$) or the Cartesian 2D PC MRI data ($p = 0.70$). Injured versus uninjured PWV values approached significance for the 4D PC MRI data ($p = 0.08$) and pressure probe data ($p = 0.09$).

Bland-Altman analysis (90) revealed that the 4D PC MRI technique (Figure 10.7), the radial 2D PC technique (Figure 10.8), and the Cartesian 2D PC technique (Figure 10.9) tended to underestimate PWV compared to the gold standard pressure probe measurements, with a mean

bias (±2SD) of -0.9 ± 3.1 m/s, -0.3 ± 8.1 m/s, and -0.4 ± 6.8 m/s, respectively. No significant differences were found between the pressure probe-based PWV measurements and the PWV measurements from 4D PC MRI (p = 0.16), radial 2D PC MRI (p = 0.83), and Cartesian 2D PC MRI (p = 0.74).

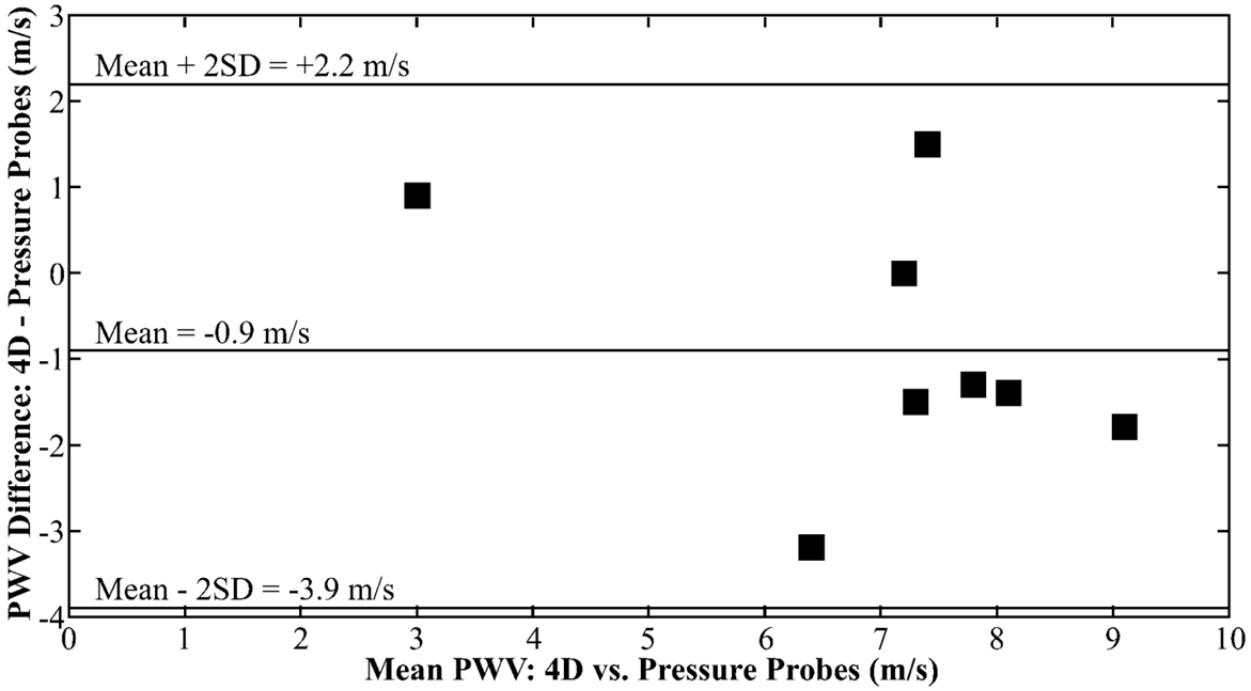

Figure 10.7 Bland-Altman plots for comparing pulse wave velocity measurements from the 4D PC MRI technique against the gold standard pressure probe-based pulse wave velocity measurements. The mean (±2 SD) Bland-Altman difference was -0.9 ± 3.1 m/s.

For WSS measurements (Figure 10.10) in the uninjured pigs, the upper (mean ± 1SD = 0.325 ± 0.092 Pa) and middle (mean ± 1SD = 0.291 ± 0.093 Pa) segments were significantly greater than WSS values in the lower (mean ± 1SD = 0.252 ± 0.085 Pa) segment, with p-values of 0.003 and 0.006, respectively. No significant difference was found between the upper and middle segments in the uninjured animals (p = 0.082). For the injured pigs, no significant differences were found between the upper (mean ± 1SD = 0.354 ± 0.067 Pa) and middle (mean ±

1SD = 0.328 ± 0.062 Pa) segments (p = 0.318), the upper and lower (mean ± 1SD = 0.279 ± 0.036 Pa) segments (p = 0.054), and the middle and lower segments (p = 0.133).

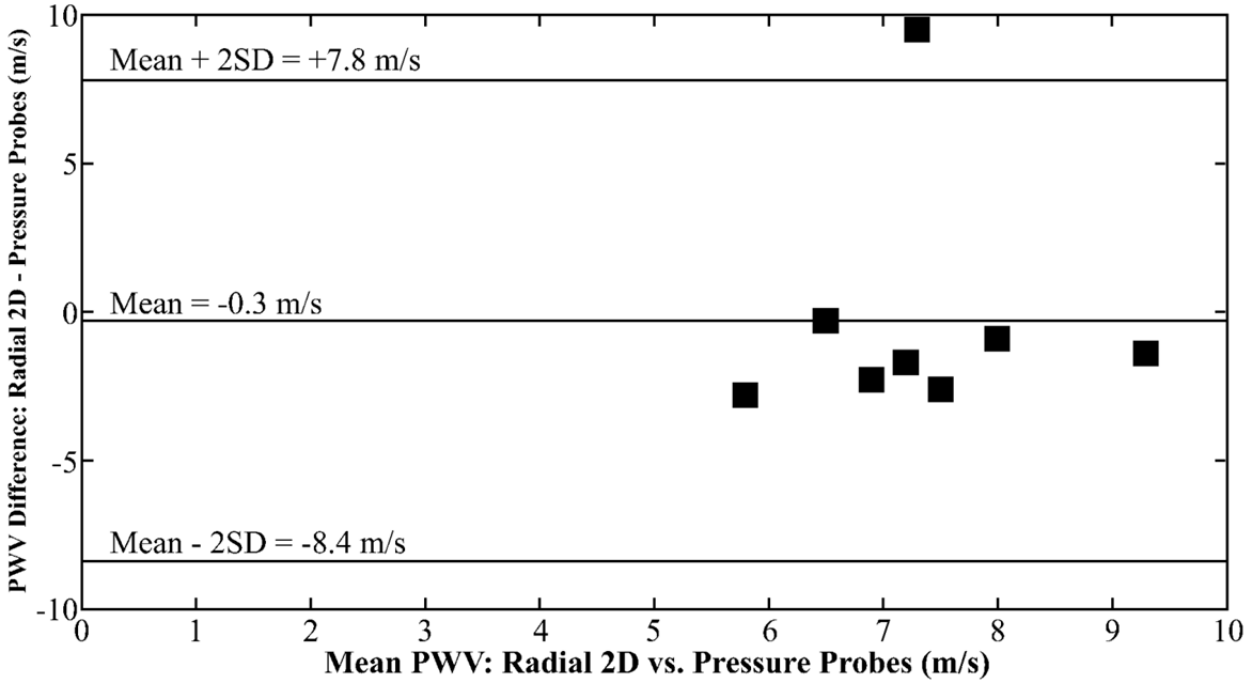

Figure 10.8 Bland-Altman plots for comparing pulse wave velocity measurements from the radial 2D PC MRI technique against the gold standard pressure probe-based pulse wave velocity measurements. The mean (±2 SD) Bland-Altman difference was -0.3 ± 8.1 m/s.

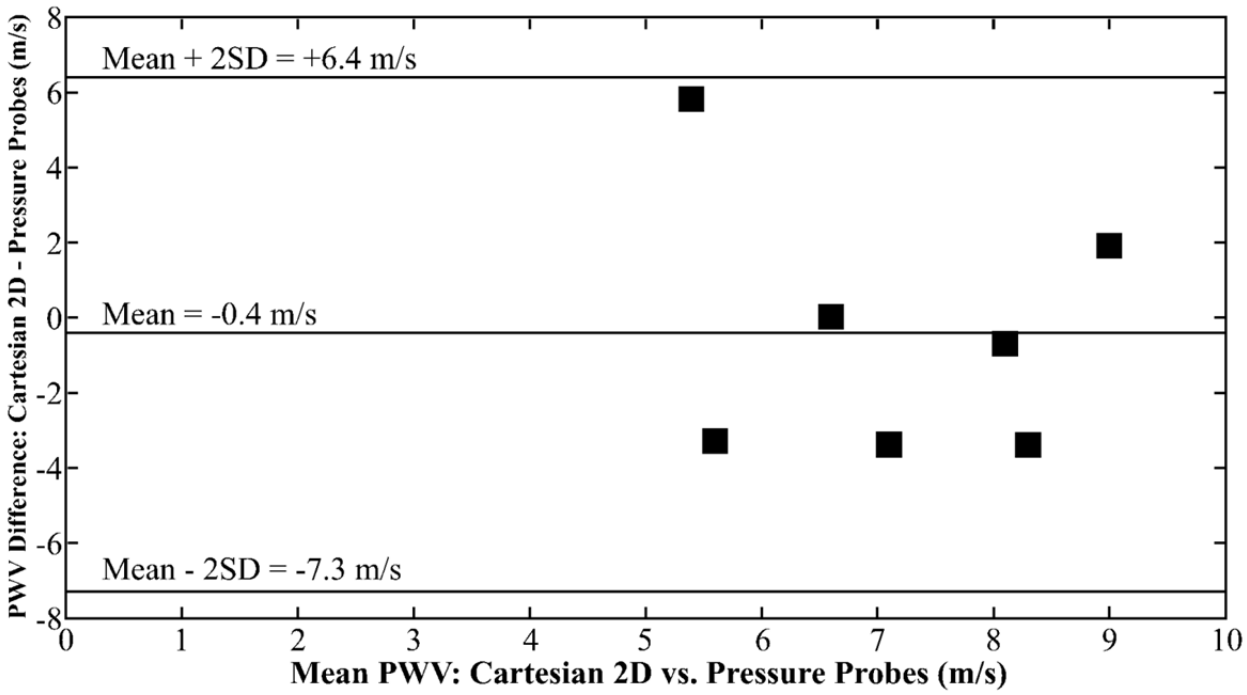

Figure 10.9 Bland-Altman plots for comparing pulse wave velocity measurements from the Cartesian 2D PC MRI technique against the gold standard pressure probe-based pulse wave velocity measurements. The mean (±2 SD) Bland-Altman difference was -0.4 ± 6.8 m/s.

No significant differences in WSS were found between the injured and uninjured pigs for the upper ($p = 0.57$), middle ($p = 0.47$), and lower ($p = 0.53$) segments.

For linear regression analysis, gender, age, heart rate, mass, and vessel diameter were not significant predictors for PWV measurements. The only significant predictor was that of vessel diameter for WSS in the upper segment ($p = 0.04$); age was a marginally significant predictor of WSS in the upper segment ($p = 0.08$).

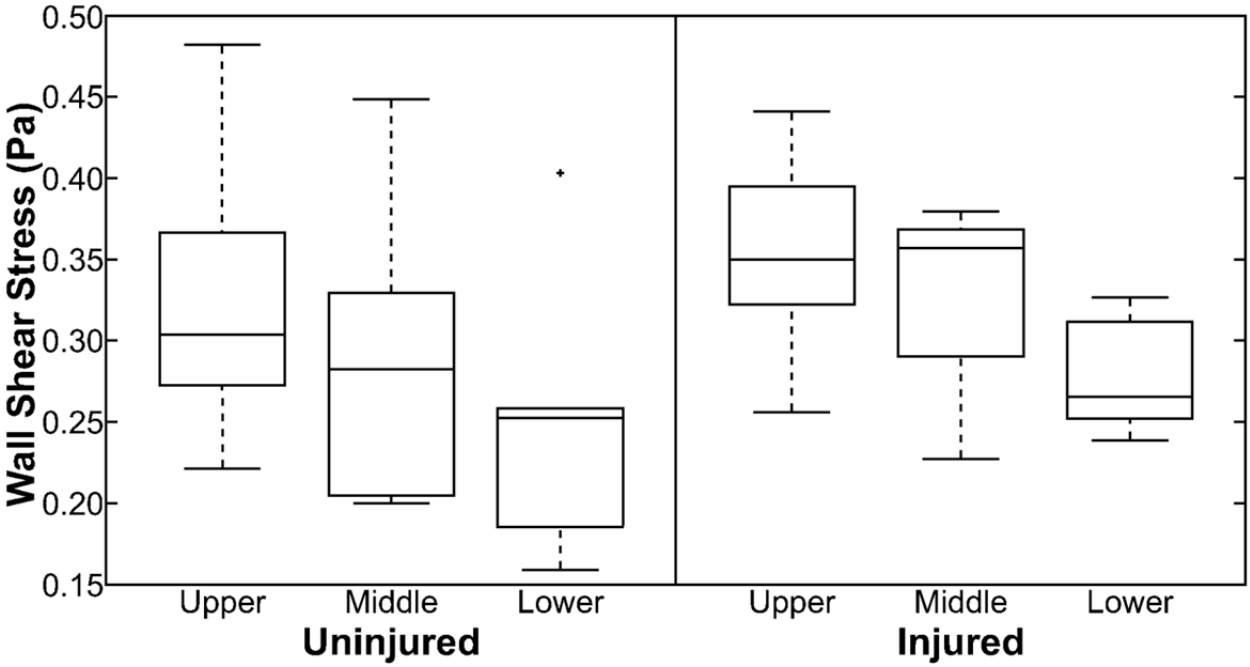

Figure 10.10 Box plots of wall shear stress computed from 4D PC MRI in the suprarenal abdominal aorta (upper segment), pararenal aorta (middle segment), and infrarenal aorta (lower segment). For the injured swine, the upper and lower segments correspond to regions injured with an angioplasty balloon.

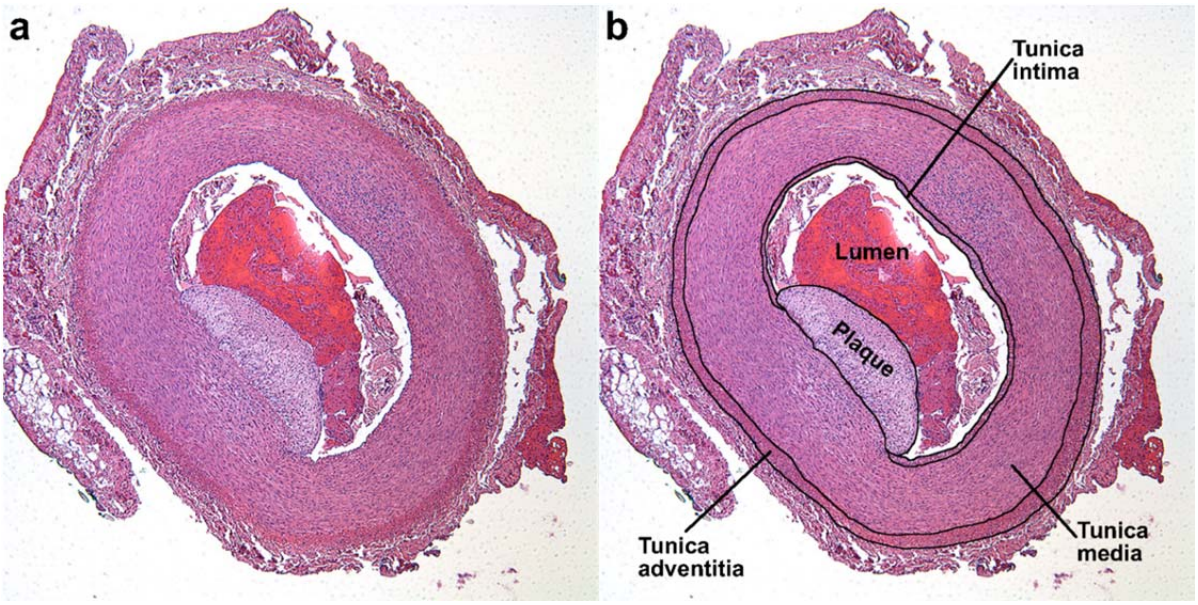

Figure 10.11 Early atherosclerotic plaques were detected in the femoral arteries of swine via haematoxylin and eosin staining in paraffin sections. Note that parts **a** and **b** are identical, except for the labels provided on part **b**. Also note that the geometric proportions in this slide are not necessarily accurate, given that vessels were not pressure perfused following excision.

10.3.4 Histology

Initial histological results from the injured femoral arteries demonstrated visible plaque development (Figure 10.11).

10.4 Discussion

The results of this study demonstrate our initial attempts of validating PWV measurements from 4D PC MRI, as well as radial and Cartesian 2D PC MRI, against the gold standard pressure probe-based PWV measurements in a swine model of familial hypercholesterolemia. Additionally, this was our initial attempt to create an injury model, to elevate the PWV values in swine, and to analyze the effects of the injury on WSS. To our knowledge this is the first comparison of 2D and 4D PC MRI-based PWV measurements in a diseased state, the first validation of 4D PC MRI PWV measurements, the first evaluation of PWV and WSS in an injury model, and the first simultaneous evaluation of PWV and WSS.

In terms of noninvasive imaging, digital subtraction angiography (DSA) is the standard means of detecting stenoses and evaluating vascular integrity. While 3D DSA images showed a minimal degree of irregularity (Figure 10.4), this evaluation is biased due to the lack of blinding. Given the limited extent to which vascular anomalies can be appreciated in these injured swine via 3D DSA, it would be encouraging to identify image-derived biomarkers that could differentiate a diseased from a non-diseased state before substantial changes occur with angiography.

Results from this study with ultrasound-based strain imaging (Figure 10.5) are limited, but encouraging. The ultrasound system needed to perform such measurements was not

consistently available for each of the swine in this study. However, these initial results suggest that the angioplasty balloon catheter-induced injury led to elevated strain. Nevertheless, it should be noted that ultrasound has a limited acoustic window through which vessels can be imaged. The femoral arteries, especially in pigs, are fairly superficial, making analysis with ultrasound viable. However, the injuries created in the aorta could not be imaged with ultrasound given how deep the aorta is relative to the skin. As described in Figure 4.5, plaques tend to develop at vessel bifurcations due to low flow, and low wall shear stress, in these areas. Although vascular territories with bifurcations were not evaluated in this swine study, it should be noted that ultrasound has limited access to several areas of interest, such as the iliac bifurcation and the takeoff of the renal arteries. The carotid arteries are often imaged with ultrasound because they bifurcate and are clinically important. Yet, there are numerous other vascular territories of interest that are not easily imaged with ultrasound.

The 4D PC MRI and the radial and Cartesian 2D PC MRI techniques underestimated PWV compared to the gold standard pressure probe-based PWV measurements. Underestimation of these measurements is likely secondary to both lower temporal resolution and temporal blurring from the acquisition of MR data over numerous heart beats. However, the 95% limits of agreement for the 4D PC MRI Bland-Altman differences (Figure 10.7) were substantially lower than the limits of agreement for the radial and Cartesian 2D PC PWV measurements. The discrepancy between 2D and 4D PC data is likely due to the difference in which data are analyzed. With 2D PC data the planes are selected at the time of acquisition. Thus, if five slices are acquired, only five different flow waveforms can be measured. With the low temporal resolution compared to the pressure probes, the sampling of one or more of those flow

waveforms can cause the waveform to appear shifted relative to the waveforms from other slices. Thus, computing PWV is highly dependent on how the waveforms are sampled from one plane to another. Furthermore, the shapes of waveforms vary substantially as the aorta is traversed. Thus, the shape can cause substantial changes to the time-to-foot fit, as well as the time-to-upstroke and cross-correlation methods of computing PWV. Since the 2D slices are determined at the time of acquisition, planes with flow waveforms of a consistent shape cannot be selected a posteriori. In comparison, the planes from 4D PC MRI are all from a single data set and thus it is less likely that sampling of the flow waveforms will vary from one plane to the next. Thus, PWV computation is likely to be more consistent. Additionally, the selection of planes is performed after the acquisition; this allows for planes to be selected that provide as consistent a shape as possible for the flow waveforms. While 4D PC MRI provides lower temporal resolution than the 2D PC techniques, the ability to select planes during the analysis and the consistency of sampling allowed for better overall PWV measurements.

While the sample sizes are small in this study and the results are complicated by the variable age of the animals, differences in PWV between the injured and uninjured swine have approached statistical significant with the 4D PC ($p = 0.08$) and pressure probe ($p = 0.09$) data. A power calculation with a t-test for normally distributed data (with unknown standard deviation) can be used to determine the number of animals needed in each group. Assuming 80% power and a difference of 2 m/s between the injured and uninjured groups, ten swine per group would be needed to achieve statistical significance. Further exploration with this animal model may reveal that evaluating the animals eight weeks post-injury, rather than four weeks post-injury as

in this study, may lead to greater PWV values in the injured group and thus reduce the number of animals needed to achieve statistical significance.

The WSS results are complicated by the nature of the study design. WSS is predominantly a predictive biomarker; from Eq. 4.7 it is revealed that in areas of low flow WSS is low and in turn this lower WSS leads to endothelial dysfunction. As the plaques develop secondary to endothelial dysfunction, the vessel radius will eventually decrease, which serves to elevate the WSS. In this study plaques were predominantly created via injury. Therefore, it is difficult to differentiate the factors that lead to particular WSS values; since plaques are created in this study the plaques are not due to low flow and therefore the areas of plaque should not have low WSS values. As plaques develop, the WSS should increase, but at four weeks post-injury there is likely to be outward remodeling of the vessels (Glagov phenomenon) (10) and therefore no substantial changes to the vessel radius. Nevertheless, it is interesting in this study that WSS values significantly decreased in lower segments of the aorta in the uninjured swine, as would be expected due to decreases in flow as the aorta is traversed. In contrast, such a pattern of lower WSS in downstream regions was not observed in the group of injured swine. While the study design, as discussed above, was not optimized for evaluating WSS, this is an interesting result that warrants further investigation.

One means of properly evaluating WSS in these animals would be to design an experiment in which plaques are allowed to develop naturally. With a longitudinal study of this design, the same animals can be evaluated and the WSS values can be tracked over time. Such a study would allow for the predictive nature of WSS to be evaluated, given that low WSS would be expected in various regions at the beginning of the study and that those same regions should

develop plaques by the end of the study. The problem, however, is that the animals will likely be too large for MRI scanning by the time plaques develop sufficiently to alter WSS values. An alternative study for evaluating WSS would be to perform a longitudinal study with a group of injured and a group of uninjured swine of matching ages. Since plaques are created in this study, the goal is not to find low WSS; rather, WSS should significantly increase in areas of injury due to decreases in vessel radius. Such a study design would also be an excellent means for further evaluating PWV measurements, as PWV should increase over each time point in the injured animals; the uninjured animals serve as a control for the PWV values, given that young animals are needed due to the size limitations of MR and that the cardiovascular system will change as the pigs develop to adulthood.

In conclusion, the 4D PC MRI acquisition provided a promising means of computing PWV in a swine model of atherosclerosis. Compared to gold standard pressure probe-based PWV measurements, 4D PC MRI provided similar values. While the study population was small, the PWV measurements from the 4D PC technique and pressure probes approached significance ($p = 0.08$-0.09) in comparing values from injured and uninjured swine. Further evaluation of PWV and WSS measurements is needed in the form of a longitudinal study with a population of injured and uninjured age-matched swine.

Chapter 11 Phase Contrast with Highly Constrained Backprojection and McKinnon-Bates Sparsification

PURPOSE: To explore and develop algorithms for accelerating the acquisition of radially undersampled phase contrast (PC) data with the use of highly constrained backprojection (HYPR) and a McKinnon-Bates approach.

MATERIALS AND METHODS: PC HYPR and McKinnon-Bates algorithms were developed to accelerate the acquisition of radially undersampled 2D PC data. Three sparsification algorithms were developed to minimize the degree of noise in accelerated phase contrast images. These sparsification techniques were based on cross-correlation, spatial sparsity, and acceleration and were incorporated into the PC HYPR and McKinnon-Bates techniques. To test the algorithms, a radially acquired 2D PC slice was acquired in the aorta at the level of the pulmonary artery with retrospective gating on a 3T scanner. A total of 1,350 projections were acquired with pseudo-random sampling such that the number of projections could be sorted into any number of time frames.

RESULTS: While the HYPR algorithm was successfully implemented for PC imaging, and although the resulting images resulted in good quality, the approach was limited. One limitation was the requirement to reconstruct low resolution images, sparsify them, and return the sparsified images to frequency space. The McKinnon-Bates approach provided superior image quality to the PC HYPR algorithm and avoided the limitations of the PC HYPR approach.

CONCLUSION: The McKinnon-Bates algorithm is a promising means of accelerating radially undersampled PC acquisitions.

11.1 Introduction

As discussed in **Chapter 4 Phase Contrast Magnetic Resonance Imaging**, the acquisition of phase contrast (PC) magnetic resonance imaging (MRI) data is a time consuming process. As a result, numerous techniques have been developed in recent years for accelerating PC MRI.

One method for accelerating the acquisition of PC data is radial undersampling (**5.1 Undersampling**) (86, 102, 163), which allows for reduced scan times at the cost of streak artifacts that are generally considered acceptable in the context of sparse data sets—inherent to PC imaging. Radial undersampling allows for accurate flow measurements even with substantial acceleration factors (163). Nevertheless, streak artifact is the limiting factor to greater undersampling factors.

A number of studies have explored the application of k-t BLAST/SENSE (**5.3 k-t BLAST/SENSE**) to PC MRI data acquisitions. These techniques have been applied to 2D PC techniques (164, 165), and to some extent have been validated with Doppler ultrasound-based flow measurements. k-t BLAST/SENSE have also been applied to 4D PC MRI techniques (142, 166-168); however, validation of these techniques has been limited and these techniques have not been applied on a 3T system, which would compensate for the decreased signal-to-noise ratio inherent in the k-t BLAST/SENSE algorithms. Temporal blurring has also been problematic with these techniques. Parallel imaging techniques (**5.2 Parallel Imaging**) have also been applied to PC MRI (142, 169-172). However, validation studies are again limited, given that most parallel imaging techniques are compared against the same acquisition with a fully sampled k-space, rather than against a gold standard. Similarly, a few studies have been performed to evaluate the

application of compressed sensing to PC MRI (173, 174). However, these techniques are in the early stages of development and have also not been thoroughly validated.

The purpose of this study was to explore and develop alternative algorithms for accelerating the acquisition of PC MRI data. Two approaches were developed, including a HYPR (highly constrained backprojection) algorithm adapted for PC MRI, as well as a McKinnon-Bates (79) approach for accelerating PC imaging.

11.2 Theory and Results

11.2.1 Phase Contrast with Highly Constrained Backprojection (HYPR)

The formation of a composite image in traditional HYPR processing is incompatible with PC MRI, given that sign information would be lost as the HYPR algorithm includes a magnitude operator. An alternative algorithm for HYPR processing was developed that allows for the preservation of sign (Figure 11.1.)

The PC HYPR algorithm begins with the reconstruction of both magnitude and phase difference images from a time series of 2D PC data acquired with radial undersampling. Figure 11.2a,b shows representative magnitude and phase images as acquired with 45 projections in the thoracic aorta of a pig during peak systole. After reconstruction of the original magnitude and phase time series, images are sparsified for subsequent PC HYPR processing. The first step in this sparsification process is the summation of differences (Figure 11.2c) between each phase image in the time series (Figure 11.2b), computed for every voxel as

$$\text{Difference Image} = \sum_{i=1}^{NumFrames-1} abs(k_i - k_{i+1}) \qquad \text{Eq. 11.1}$$

where *NumFrames* is the number of time frames in the image series and *k* is each individual image in the time series. Since voxels within a vessel will vary minimally compared to random noise, which varies substantially from one time frame to the next, this sparsification step seeks to cut out a portion of the background noise. The Difference Image is then thresholded such that values greater than 20% of the maximum value are nulled (Figure 11.2d). The thresholded Difference Image is then converted to a binary format and multiplied by the original series of magnitude and phase images to provide the initial step in the sparsification process (Figure 11.2e,f). The sparsified time series of phase images is cross-correlated with a sine wave for each voxel (Figure 11.2g). Ideally, voxels within a vessel will have greater correlation with a temporally varying function than will voxels of random noise. The cross-correlation map is then thresholded such that values less than 50% of the maximum are nulled (Figure 11.2h). The thresholded cross-correlation map is then spatially sparsified, in which a kernel is iterated through the map counting the number of non-zero values adjacent to every voxel. Voxels with less than three non-zero neighbors are nulled. This spatial sparsifying algorithm is iterated three times (Figure 11.2i-k). To prevent erosion of the vessels, the map is then convolved with a 2D rect function. The final map is then converted to a binary and multiplied by the magnitude and velocity images to obtain substantially sparsified images (Figure 11.2l,m).

Subsequently, the real and imaginary components of the time series are separated (Figure 11.2n,o) from the magnitude and phase difference images, with real images computed as the magnitude image multiplied by the cosine of the phase difference image and the imaginary

images computed as the magnitude image multiplied by the sine of the phase difference image. A sign map is created for each real and imaginary time frame (Figure 11.2p,q) such that a matrix of equal size to the image is created; values in the sign maps are assigned as -1 for negative values, 0 for null values, and +1 for positive values.

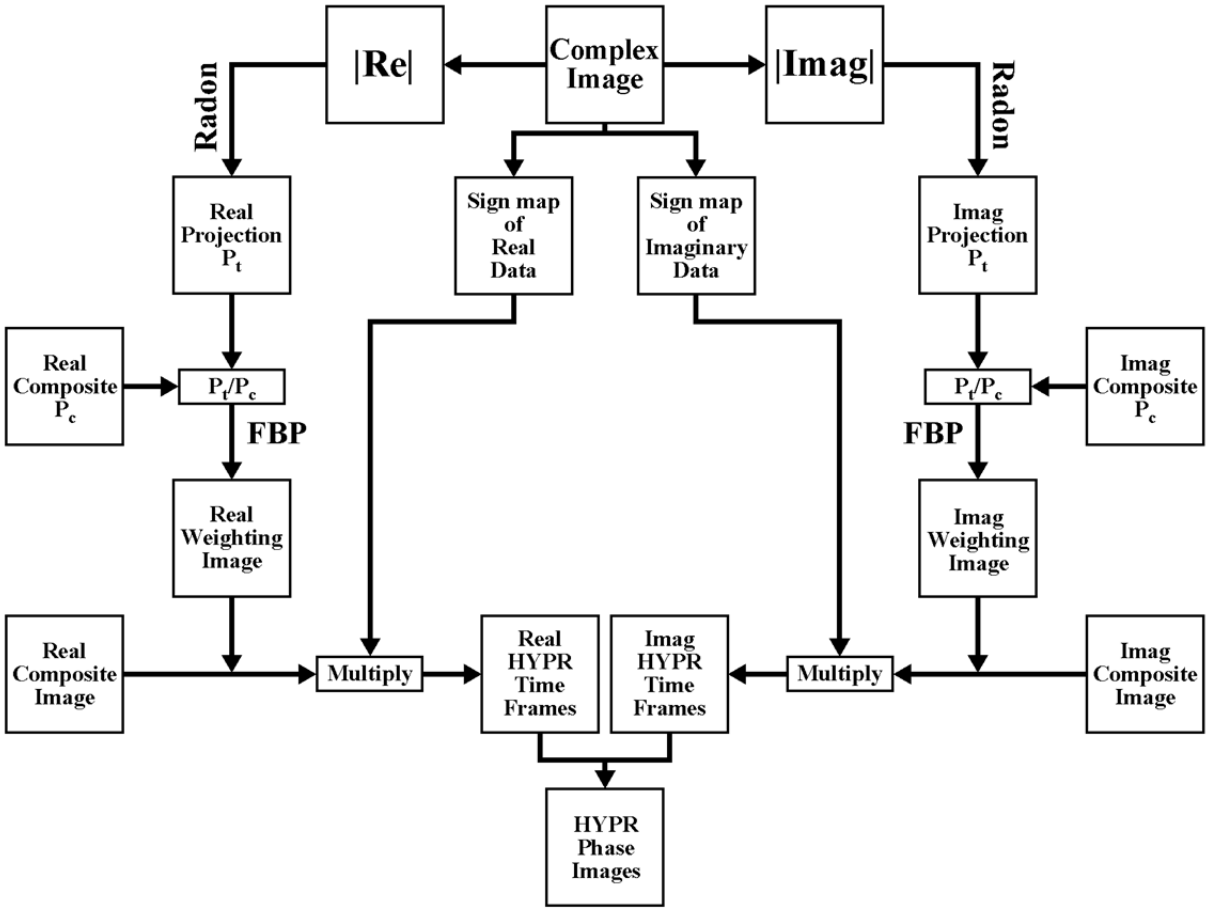

Figure 11.1 Algorithm for HYPR (highly constrained backprojection) processing of phase contrast magnetic resonance imaging data. Imag = imaginary, FBP = filtered backprojection

The absolute value of the real and imaginary components is computed to make all values positive (Figure 11.2r,s). Then, similar to traditional HYPR processing, a Radon transform is performed on both the real and imaginary images to create image space profiles (P_t) (Figure 11.2t,u). Real and imaginary composite images (Figure 11.2v,w) are created from all radial

projections and transformed to create an image space profile (P_c) (Figure 11.2x,y). P_t is divided by P_c separately for the real and imaginary components to create weighting images in sinogram space (Figure 11.2z,α). Filtered backprojection is then performed on the result of this division to create weighting images (Figure 11.2β,γ), which are subsequently multiplied by the composite image. To return the sign information from the original images, the sign maps are multiplied by the result of the multiplication of the composite and weighting images (Figure 11.2δ,ε). As a result, separate real and imaginary HYPR time frames are created with the sign preserved. The phase difference HYPR time frames can be computed via the inverse tangent of the imaginary divided by the real images (Figure 11.2ζ).

Velocity over time curves measured in the ascending aorta from the original and PC HYPR-processed time series reveal similar temporal dynamics (Figure 11.3). However, velocity values tended to be dampened in the PC HYPR-processed images, likely due to a scaling factor inherent in the processing of the data. In its current form, the algorithm is rather complex and requires several parameter choices that might require optimization for specific vascular regions.

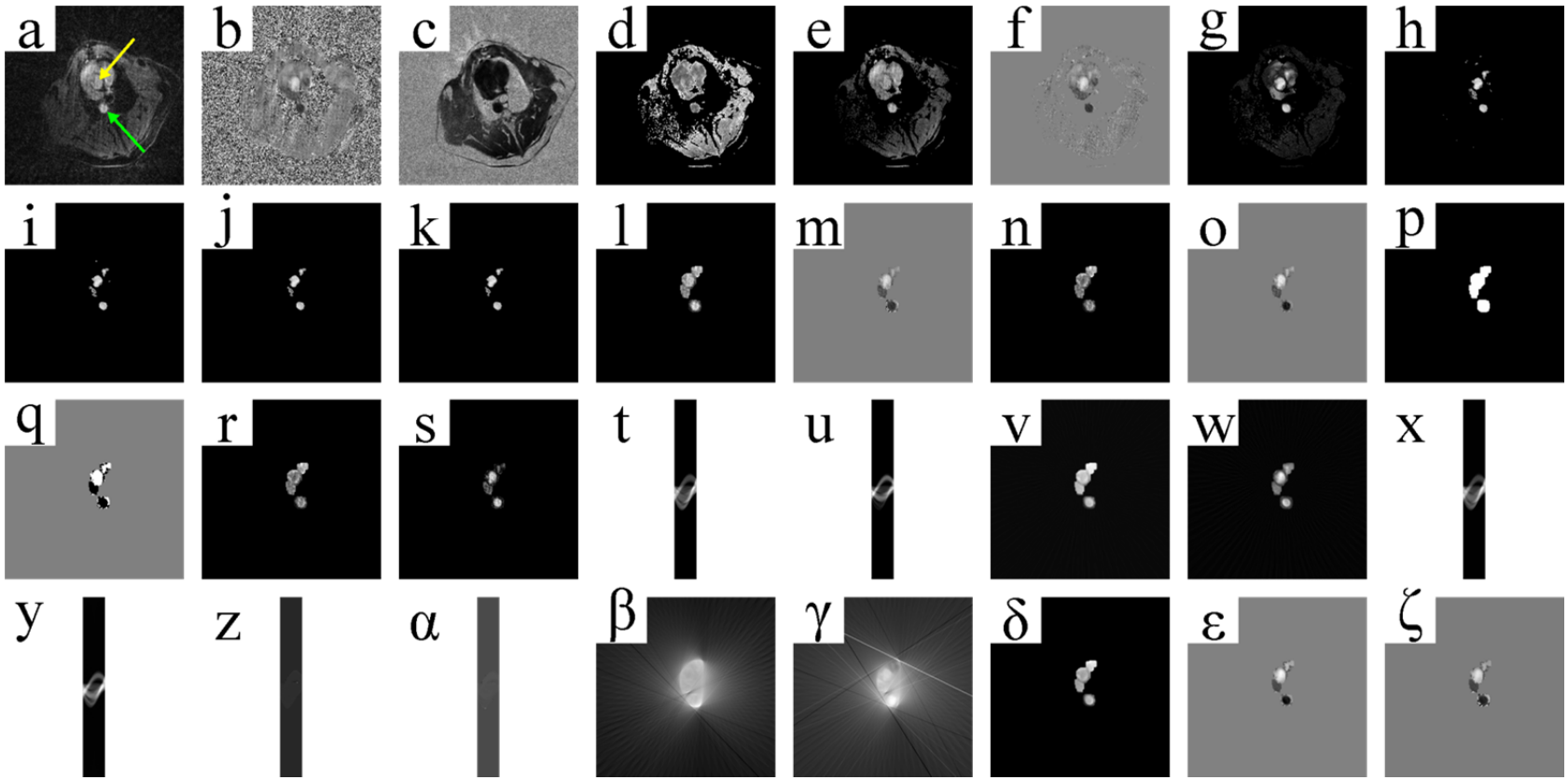

Figure 11.2 Image results from the phase contrast (PC) HYPR (highly constrained backprojection) algorithm from radially undersampled 2D PC data in the thoracic aorta of a pig. Original undersampled magnitude (**a**) and phase (**b**) images are shown, with the yellow arrow identifying the ascending aorta and the green arrow identifying the descending aorta. A variety of sparsification algorithms are initially applied to the reconstructed data to eliminate background noise/signal (**c**-**m**). Images are also shown for each stage of the PC HYPR algorithm (**n**-**ζ**), as discussed in the text.

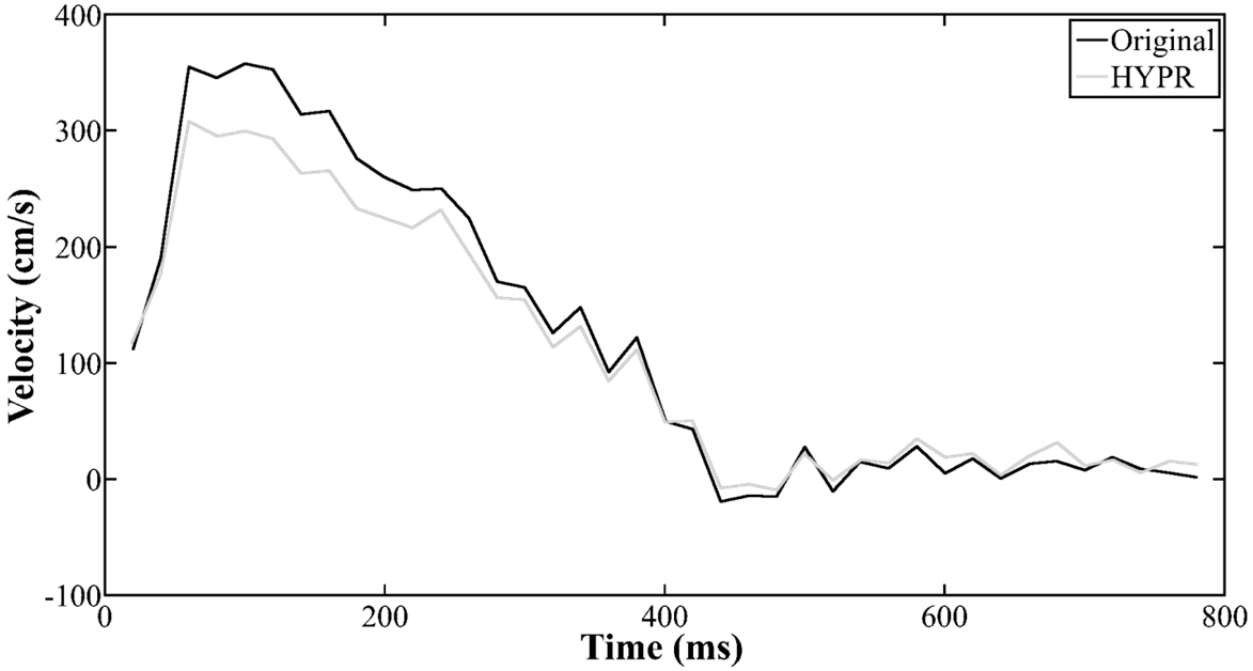

Figure 11.3 Velocity over time in the ascending aorta of a pig as measured from original radially undersampled 2D phase contrast (PC) data acquired with 45 projections (shown in black). Velocity over time was also measured from the same images, as processed and reconstructed with the PC HYPR (highly constrained backprojection) algorithm (shown in grey).

11.2.2 McKinnon-Bates

The McKinnon-Bates algorithm was initially designed for accelerating the acquisition of dynamic images in computed tomography (79). Figure 11.4 shows an algorithm that utilizes the principals of the McKinnon-Bates algorithm and adapts the technique for PC MRI.

Following the acquisition of a series of radially undersampled 2D PC data, all of the original undersampled time frames are reconstructed to provide images with significant streak artifacts (Figure 11.5a,b). These undersampled images are processed with a variety of sparsification algorithms that seek to identify the portions of the image that represent background and noise. The first step in this sparsification process is the formation of a Difference Image (Figure 11.5c), as discussed above in Eq. 11.1. The Difference Image in **Error! Reference**

source not found. is then thresholded such that values greater than 20% of the maximum value in the Difference Image are nulled (Figure 11.5d). The thresholded difference image is also convolved with a 2D rect function to prevent vessel erosion (Figure 11.5e).

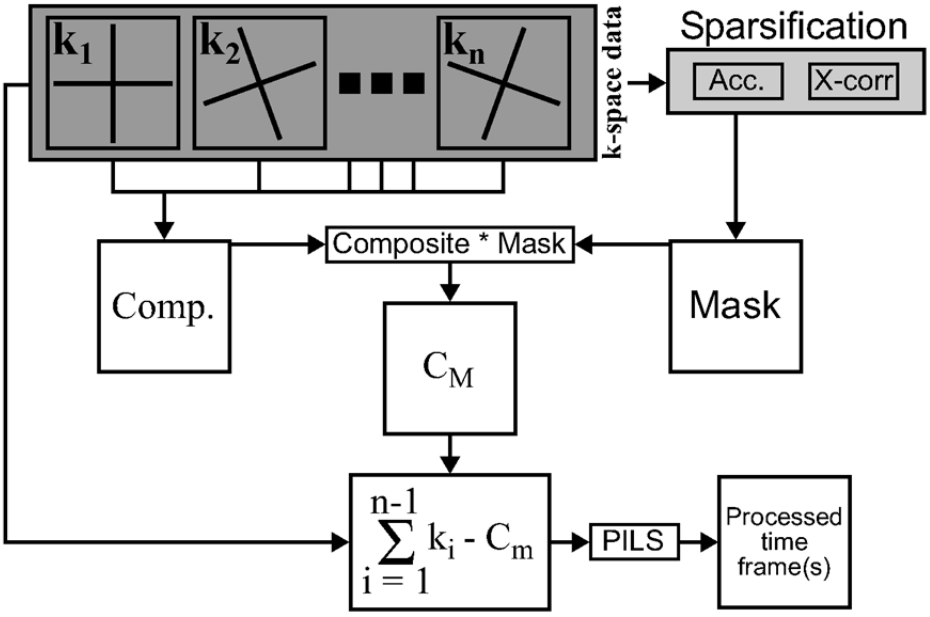

Figure 11.4 McKinnon-Bates algorithm for accelerating data from phase contrast magnetic resonance imaging. Comp = composite, Acc = acceleration, X-corr = cross-correlation, PILS = parallel imaging with localized sensitivities

The convolved and thresholded Difference Image is then multiplied by the original magnitude and phase images to provide initial sparsification of the background noise (Figure 11.5f,g). Subsequently, the sparsified time series of phase images is cross-correlated with a sine wave for each voxel. Ideally, voxels within a vessel will have greater correlation with a temporally varying function than will voxels of random noise. The cross-correlation operation creates a correlation map (Figure 11.5h), which is normalized and subtracted from 1 to provide a probability map that a voxel is representative of background signal/noise (Figure 11.5i). The probability map is then multiplied by the sparsified images in Figure 11.5f,g to complete the sparsification portion of the McKinnon-Bates algorithm (Figure 11.5j,k). Next, all of the

projections are added together and reconstructed to form a composite image (Figure 11.5l), similar to traditional HYPR processing. The composite image provides a relatively artifact-free temporally averaged image.

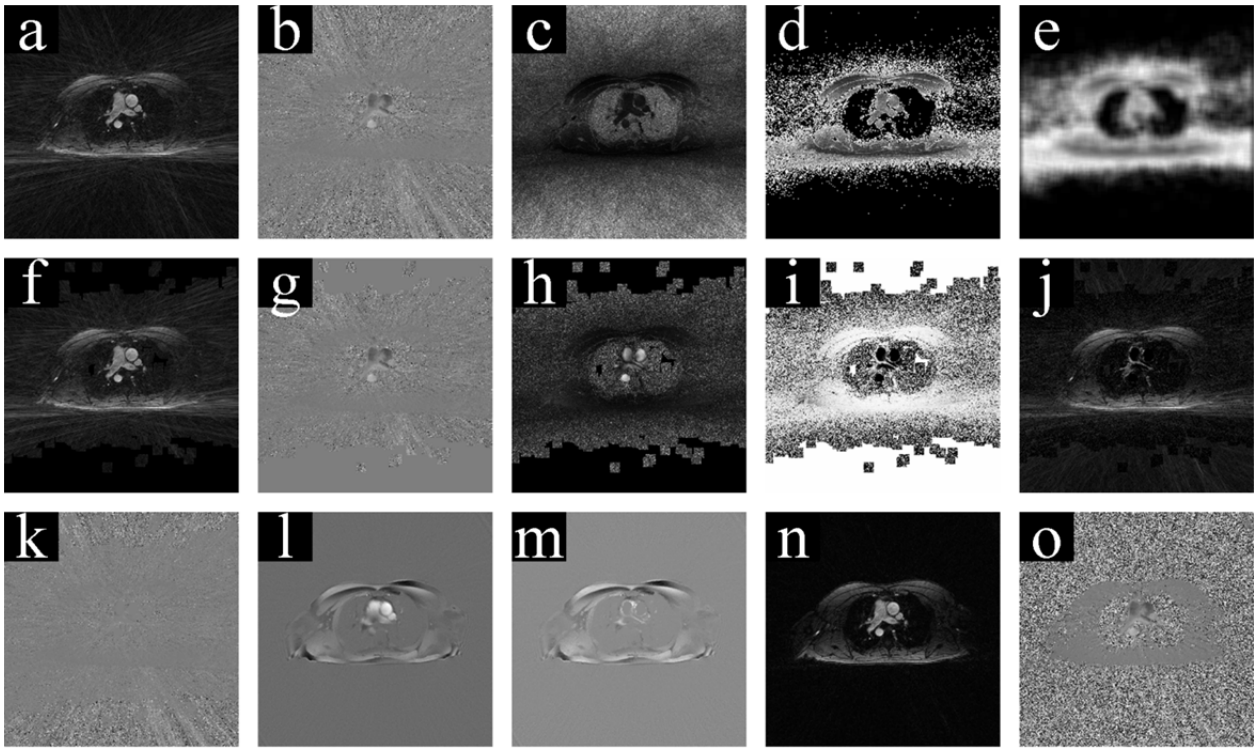

Figure 11.5 Image results from the McKinnon-Bates phase contrast (PC) algorithm from radially undersampled 2D PC data in the thoracic aorta of a healthy human volunteer. Original undersampled magnitude (**a**) and phase (**b**) images are shown. A variety of sparsification algorithms are initially applied to the reconstructed data to eliminate background noise/signal (**c-k**). Images are also shown for each stage of the McKinnon-Bates PC algorithm (**l-o**), as discussed in the text.

The cross-correlation probability mask is multiplied by the composite image (Figure 11.5m) and returned into projection space (C_M). Subsequently, projection data from the composite mask is subtracted from the projection space of each time frame such that the k-space data are representative only of the objects of interest (vessels). This processing is performed for

images of each coil. Images from all coils are combined with PILS (71) to provide the final McKinnon-Bates PC images (Figure 11.5n,o).

Velocity over time curves measured in the ascending aorta from the original and McKinnon-Bates-processed time series reveal similar temporal dynamics and similar velocity values (Figure 11.6).

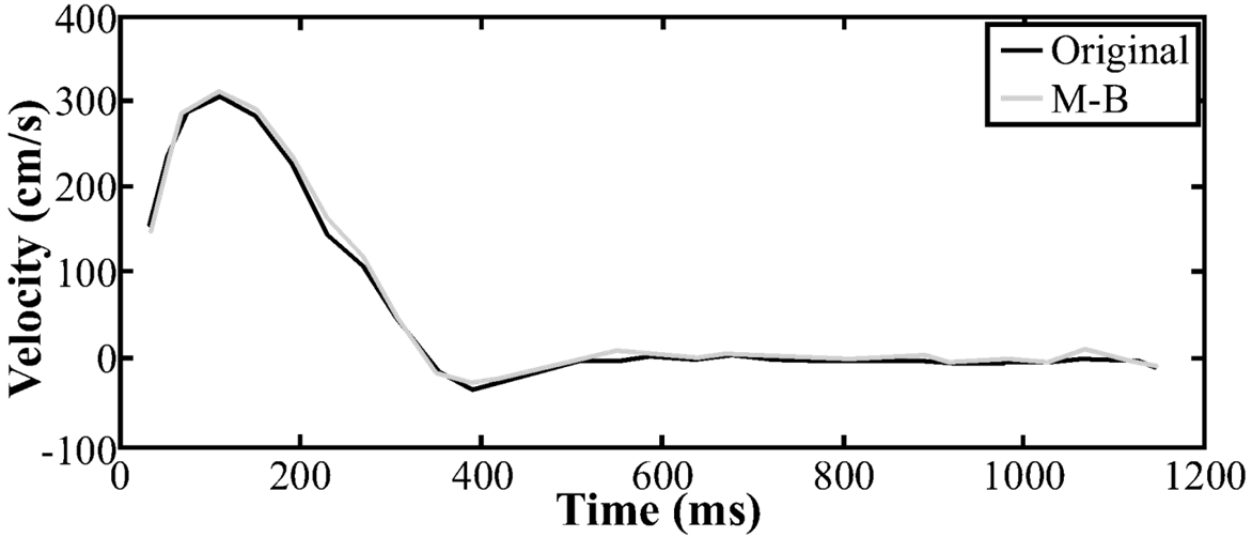

Figure 11.6 Velocity over time in the ascending aorta of a healthy human volunteer as measured from original radially undersampled 2D phase contrast (PC) data acquired with 45 projections (shown in black). Velocity over time was also measured from the same images, as processed and reconstructed with the McKinnon-Bates PC algorithm (shown in grey).

11.3 Discussion

In this study two new algorithms were developed for accelerating the acquisition and/or improving the image quality of radially undersampled 2D phase contrast (PC) images. Additionally, a number of approaches and algorithms for sparsifying 2D PC images were developed. With the PC HYPR algorithm we have provided images with little to no noise or non-vessel background anatomy. With the McKinnon-Bates (M-B) sparsification processing we have reconstructed images with reduced streak artifacts. Despite the low number of projections,

temporal resolution, image quality, and velocity information of reconstructed time frames were preserved. These algorithms may be useful for reducing the scan time needed for the acquisition of 2D PC data or for improving temporal resolution.

As seen in Figure 11.3 and Figure 11.6, velocity measurements from original radially undersampled 2D PC data were well represented by velocity measurements from both the PC HYPR and M-B processed images. However, velocity values from PC HYPR-processed images tended to be less accurate, with a scaling factor that led to noticeably different values during systolic time frames. Due to the large number of steps and transforms inherent in the PC HYPR algorithm, a scaling factor is introduced that is currently unresolved in the algorithm. The M-B algorithm is a much simpler approach that provided nearly identical velocity measurements compared to the original unprocessed data.

Both the PC HYPR and M-B algorithms depend on sparsification. In turn, sparsification depends on the temporal dynamics of the vessels, namely via the Difference Image, which relies on small changes from one phase image to the next, and the cross-correlation algorithm, which identifies high correlation between a sine wave and flow in a vessel's voxel. Therefore, sparsification depends on images being of sufficient quality, despite substantial undersampling. While the images in this study, as acquired with 45 projections per time frame, represent an undersampling factor of 9, similar results in image quality have been obtained with an undersampling factor of 30 (14 projections per time frame). The PC HYPR and M-B algorithms are therefore limited by the inherent limitations in radial undersampling—streak artifacts and the obscurity of vessels. At minimum these algorithms, especially the M-B algorithm, are useful for substantially improving image quality. Further experiments are needed with a flow phantom to

test whether or not the algorithm and the removal of streak artifacts can actually improve velocity and flow measurements compared to measurements obtained directly from undersampled data.

Flow measurements even with highly undersampled radial 2D PC data are still reliable (163). As discussed in **5.1 Undersampling**, sampling in a radial pattern allows for the reconstruction of images with a normal field of view at the expense of streak artifacts. This is in contrast to other accelerated imaging techniques, such as parallel imaging, which omits lines in a rectilinearly sampled k-space, leading to significant aliasing/wraparound artifact (Figure 5.1). Therefore, the PC HYPR and M-B algorithms were not developed to allow for the reconstruction of proper unaliased images, as is needed in parallel imaging, for example. Instead, these algorithms were developed to mitigate artifacts due to acceleration via undersampling and thus provide either cleaner images or allow for greater undersampling.

While the PC HYPR approach had severe limitations, future work is needed and planned for advancing the M-B algorithm. Further improvements in the reconstruction of images may be possibly via the incorporation of k-t SENSE (72). The M-B algorithm, as well as the sparsification techniques, need to be adapted to a 3D radial undersampling acquisition (PC VIPR) (102). Minimal changes would be needed in the sparsification code, given that summing the differences between images and cross-correlation has little regard for dimensionality. Aside from sparsification, minimal changes would be needed to adapt the M-B algorithm for a third dimension. While processing time may be substantial for 3D data sets, the minimal changes needed for the algorithms as well as the potential benefits of the M-B algorithm, warrant such future work as a prudent endeavor.

Chapter 12 Summary and Recommendations

12.1 Summary

Phase contrast magnetic resonance imaging (PC MRI) has the potential to provide valuable information on the atherosclerotic disease state. However, the acquisition of PC data is time-consuming. The use of radial undersampling, as underscored in this work, accelerates PC MRI acquisitions. The contributions of this work can be summarized as follows:

- The design and implementation of experiments to evaluate the accuracy of flow measurements acquired with radially undersampled 2D PC MRI both in flow phantoms and in healthy human volunteers.
- The design and implantation of a tool that allows for the evaluation of pulse wave velocity (PWV) from both 2D and 4D PC MRI data, the evaluation of PWV in twenty healthy human volunteers, and the assessment of 4D- versus 2D-derived PWV measurements.
- The experimental design and assessment of wall shear stress (WSS) derived from 4D PC MRI data in healthy human volunteers and in patients with an ascending aortic aneurysm.
- The experimental design and assessment of the repeatability and internal consistency of 2D and 4D PC MRI flow measurements in the abdominal vasculature of healthy human volunteers and the design and implementation of a tool and algorithm for comparing flow waveforms derived from PC data that utilize retrospective or prospective cardiac gating techniques.

- The design, implementation, and evaluation of WSS and PWV measurements derived from 4D PC MRI data acquired in swine with familial hypercholesterolemia, as well as the design, implementation, and evaluation of an algorithm and tool for assessing PWV from pressure probe measurements in these swine.
- The design, implementation, and demonstration of algorithms for sparsifying PC MRI data, as well as the design, implementation, and assessment of an algorithm for applying the HYPR algorithm to radially undersampled PC MRI data.
- The design, implementation, and demonstration of additional algorithms for sparsifying PC MRI data, as well as a McKinnon-Bates algorithm for accelerating radially undersampled PC MRI data.

12.2 Recommendations

Numerous improvements have been made to the radially undersampled 2D PC pulse sequence since the acquisition was assessed in flow phantoms and in healthy human volunteers. These improvements include reductions of errors from concomitant field gradients and compensation for trajectory errors. While flow measurements were quite accurate despite a great degree of undersampling, the results may be more accurate given the above improvements. Furthermore, a more thorough investigation of the radially undersampled 2D PC sequence should be performed in vivo. Ideally, MRI-compatible flow probes should be placed around the arteries (of various sizes) of a swine model to evaluate probe-derived flow measurements against the radially undersampled 2D PC technique.

A more thorough analysis is needed for the assessment of PWV with radially undersampled 4D PC MRI. The study on PWV in this dissertation used twenty subjects with a

wide age range. It is well known that PWV increases independently with both age and blood pressure. Therefore, a more thorough analysis would include a larger number of healthy subjects, with a group of subjects for every decade of adulthood, from 20 – 80 years of age. Blood pressure should be measured in all subjects. Furthermore, the results from these subjects should be compared to age-matched diseased individuals, identified via a medium- to high-risk Framingham risk score. Studies could also be extended to evaluate PWV in subjects before and after medical therapy, such as a statin. 4D-derived PWV measurements, in the above experiments, should also be compared with 2D-derived PWV measurements, as well as with a Fourier-encoded technique with high temporal resolution. This latter technique can be used for regional PWV assessment in straight anatomical segments, such as the descending aorta (in most subjects). A comparative assessment of regional PWV with the 4D PC MRI acquisition would also be prudent. 4D-derived PWV should also be assessed for both inter- and intra-day repeatability.

Similar to the experiments needed for PWV above, it would be useful to evaluate 4D-derived WSS measurements in groups of healthy humans in each decade of adulthood and compare the results to age-matched diseased subjects, as identified with the Framingham risk score. An assessment of both inter- and intra-day repeatability would also be useful. In terms of technical developments, the WSS tool developed by others at UW only allows for assessments of WSS in the superior-to-inferior direction. The tool should be extended to allow for any orientation. Also, 4D-derived WSS measurements should be compared to a simulation with computational fluid dynamics.

While intra-day repeatability of 4D PC MRI flow measurements was assessed, inter-day repeatability should also be assessed. Furthermore, the repeatability/internal consistency study, as included in this dissertation, only evaluated measurements in the abdominal vasculature. Such analysis is also needed in other vasculature territories.

There is great potential for further work in the study of pigs with familial hypercholesterolemia (FH). The next logical step would be to perform a longitudinal study in which a group of FH swine with injury, and a group of age-matched FH swine without injury, would be evaluated at multiple time points, including a baseline measurement, and 2-, 4-, 6-, and 8-weeks post-injury. Over this time period PWV should increase at each time point in the injured group. Since WSS is a predictive biomarker, it is difficult to predict atherosclerosis development via WSS measurements given that plaques would be artificially created in these animals. The assessment of WSS is more apt in situations where plaques develop naturally as a result of low WSS, which would not occur in an artificial situation as proposed here. However, if plaques development sufficiently such that the vessel radius decreases, WSS should increase over time in the injured animals according to Eq. 4.7. At the end of the study, each animal should be sacrificed so that vessels can be harvested. Ideally, the vessels would be pressure-perfused so that vascular geometry would be maintained. Histology could be used to assess the true degree of atherosclerotic burden. Additionally, it would be ideal to assess the plaque for each time point via MRI-based vessel wall imaging techniques. While the vessel wall imaging techniques could only be corroborated against histology after the final time point, it would be interesting to image the plaque progression over the series of time points.

Finally, more work is needed on the McKinnon-Bates (M-B) algorithm. Initially the algorithm can be improved via the incorporation of k-t SENSE. Furthermore, the M-B algorithm needs to be extended to 4D data, which would require sparsification algorithms for a highly undersampled 3D time series of data. Given the computation power needed for 2D processing of the M-B algorithm, a 4D implementation would require considerable computing power, such that future hardware improvements, or an implementation on a graphics processing unit (GPU), would be required to make the algorithm practical.

Bibliography

1. Wilson PW. Established risk factors and coronary artery disease: the Framingham Study. Am J Hypertens 1994;7:7S-12S.

2. Kumar V, Abbas AK, Aster JC, Fausto N. *Robbins & Cotran Pathologic Basis of Disease*. 8th ed.: Saunders, 2009.

3. Strong JP, Malcom GT, McMahan CA, et al. Prevalence and extent of atherosclerosis in adolescents and young adults: implications for prevention from the Pathobiological Determinants of Atherosclerosis in Youth Study. JAMA 1999;281:727-735.

4. Miller DT, Ridker PM, Libby P, Kwiatkowski DJ. Atherosclerosis: the path from genomics to therapeutics. J Am Coll Cardiol 2007;49:1589-1599.

5. Gaziano JM, Wilson PW. Cardiovascular risk assessment in the 21st century. JAMA 2012;308:816-817.

6. Akosah KO, Schaper A, Cogbill C, Schoenfeld P. Preventing myocardial infarction in the young adult in the first place: how do the National Cholesterol Education Panel III guidelines perform? J Am Coll Cardiol 2003;41:1475-1479.

7. Kannel WB, Dawber TR, Kagan A, Revotskie N, Stokes J, 3rd. Factors of risk in the development of coronary heart disease--six year follow-up experience. The Framingham Study. Ann Intern Med 1961;55:33-50.

8. Kaul P, Douglas PS. Atherosclerosis imaging: prognostically useful or merely more of what we know? Circ Cardiovasc Imaging 2009;2:150-160.

9. Korshunov VA, Berk BC. Strain-dependent vascular remodeling: the "Glagov phenomenon" is genetically determined. Circulation 2004;110:220-226.

10. Glagov S, Weisenberg E, Zarins CK, Stankunavicius R, Kolettis GJ. Compensatory enlargement of human atherosclerotic coronary arteries. N Engl J Med 1987;316:1371-1375.

11. Schmermund A, Erbel R. Unstable coronary plaque and its relation to coronary calcium. Circulation 2001;104:1682-1687.

12. Taylor AJ, Burke AP, O'Malley PG, et al. A comparison of the Framingham risk index, coronary artery calcification, and culprit plaque morphology in sudden cardiac death. Circulation 2000;101:1243-1248.

13. Bild DE, Bluemke DA, Burke GL, et al. Multi-ethnic study of atherosclerosis: objectives and design. Am J Epidemiol 2002;156:871-881.

14. Detrano R, Guerci AD, Carr JJ, et al. Coronary calcium as a predictor of coronary events in four racial or ethnic groups. N Engl J Med 2008;358:1336-1345.

15. Yeboah J, McClelland RL, Polonsky TS, et al. Comparison of novel risk markers for improvement in cardiovascular risk assessment in intermediate-risk individuals. JAMA 2012;308:788-795.

16. Pignoli P, Tremoli E, Poli A, Oreste P, Paoletti R. Intimal plus medial thickness of the arterial wall: a direct measurement with ultrasound imaging. Circulation 1986;74:1399-1406.

17. Stein JH, Korcarz CE, Hurst RT, et al. Use of carotid ultrasound to identify subclinical vascular disease and evaluate cardiovascular disease risk: a consensus statement from the American Society of Echocardiography Carotid Intima-Media Thickness Task Force. Endorsed by the Society for Vascular Medicine. J Am Soc Echocardiogr 2008;21:93-111; quiz 189-190.

18. Den Ruijter HM, Peters SA, Anderson TJ, et al. Common carotid intima-media thickness measurements in cardiovascular risk prediction: a meta-analysis. JAMA 2012;308:796-803.

19. Goldberg AC, Hopkins PN, Toth PP, et al. Familial hypercholesterolemia: screening, diagnosis and management of pediatric and adult patients: clinical guidance from the National Lipid Association Expert Panel on Familial Hypercholesterolemia. J Clin Lipidol 2011;5:133-140.

20. Sibley C, Stone NJ. Familial hypercholesterolemia: a challenge of diagnosis and therapy. Cleve Clin J Med 2006;73:57-64.

21. Rader DJ, Cohen J, Hobbs HH. Monogenic hypercholesterolemia: new insights in pathogenesis and treatment. J Clin Invest 2003;111:1795-1803.

22. Bernstein MA, King KF, Zhou XJ. *Handbook of MRI Pulse Sequences*. Burlington, MA, Elsevier Academic Press, 2004.

23. Moran PR. A flow velocity zeugmatographic interlace for NMR imaging in humans. Magn Reson Imaging 1982;1:197-203.

24. Bryant DJ, Payne JA, Firmin DN, Longmore DB. Measurement of flow with NMR imaging using a gradient pulse and phase difference technique. J Comput Assist Tomogr 1984;8:588-593.

25. Moran PR, Moran RA, Karstaedt N. Verification and evaluation of internal flow and motion. True magnetic resonance imaging by the phase gradient modulation method. Radiology 1985;154:433-441.

26. Korosec FR, Turski PA. Velocity and Volumem Flow Rate Measurements Using Phase Contrast Magnetic Resonance Imaging. International Journal of Neuroradiology 1997;3:293-318.

27. Nayler GL, Firmin DN, Longmore DB. Blood flow imaging by cine magnetic resonance. J Comput Assist Tomogr 1986;10:715-722.

28. Pelc NJ, Herfkens RJ, Shimakawa A, Enzmann DR. Phase contrast cine magnetic resonance imaging. Magn Reson Q 1991;7:229-254.

29. Tang C, Blatter DD, Parker DL. Accuracy of phase-contrast flow measurements in the presence of partial-volume effects. Journal of Magnetic Resonance Imaging 1993;3:377-385.

30. Wolf RL, Ehman RL, Riederer SJ, Rossman PJ. Analysis of systematic and random error in MR volumetric flow measurements. Magn Reson Med 1993;30:82-91.

31. Pelc NJ, Sommer FG, Li KC, Brosnan TJ, Herfkens RJ, Enzmann DR. Quantitative magnetic resonance flow imaging. Magn Reson Q 1994;10:125-147.

32. Hausmann R, Lewin JS, Laub G. Phase-contrast MR angiography with reduced acquisition time: new concepts in sequence design. Journal of Magnetic Resonance Imaging 1991;1:415-422.

33. Pelc NJ, Bernstein MA, Shimakawa A, Glover GH. Encoding strategies for three-direction phase-contrast MR imaging of flow. Journal of Magnetic Resonance Imaging 1991;1:405-413.

34. Johnson KM, Markl M. Improved SNR in phase contrast velocimetry with five-point balanced flow encoding. Magn Reson Med 2010;63:349-355.

35. Malek AM, Alper SL, Izumo S. Hemodynamic shear stress and its role in atherosclerosis. JAMA 1999;282:2035-2042.

36. Gnasso A, Irace C, Carallo C, et al. In vivo association between low wall shear stress and plaque in subjects with asymmetrical carotid atherosclerosis. Stroke 1997;28:993-998.

37. Zarins CK, Giddens DP, Bharadvaj BK, Sottiurai VS, Mabon RF, Glagov S. Carotid bifurcation atherosclerosis. Quantitative correlation of plaque localization with flow velocity profiles and wall shear stress. Circ Res 1983;53:502-514.

38. Caro CG, Fitz-Gerald JM, Schroter RC. Atheroma and arterial wall shear. Observation, correlation and proposal of a shear dependent mass transfer mechanism for atherogenesis. Proc R Soc Lond B Biol Sci 1971;177:109-159.

39. Langille BL, O'Donnell F. Reductions in arterial diameter produced by chronic decreases in blood flow are endothelium-dependent. Science 1986;231:405-407.

40. Butterfield AB, Miller CW, Lumb WV, McLeod FD, Nelson AW, Histand MB. Inverse effect of chronically elevated blood flow on atherogenesis in miniature swine. Atherosclerosis 1977;26:215-224.

41. Ben Driss A, Benessiano J, Poitevin P, Levy BI, Michel JB. Arterial expansive remodeling induced by high flow rates. Am J Physiol 1997;272:H851-858.

42. Mondy JS, Lindner V, Miyashiro JK, Berk BC, Dean RH, Geary RL. Platelet-derived growth factor ligand and receptor expression in response to altered blood flow in vivo. Circ Res 1997;81:320-327.

43. Walpola PL, Gotlieb AI, Langille BL. Monocyte adhesion and changes in endothelial cell number, morphology, and F-actin distribution elicited by low shear stress in vivo. Am J Pathol 1993;142:1392-1400.

44. Walpola PL, Gotlieb AI, Cybulsky MI, Langille BL. Expression of ICAM-1 and VCAM-1 and monocyte adherence in arteries exposed to altered shear stress. Arterioscler Thromb Vasc Biol 1995;15:2-10.

45. Oshinski JN, Ku DN, Mukundan S, Jr., Loth F, Pettigrew RI. Determination of wall shear stress in the aorta with the use of MR phase velocity mapping. Journal of Magnetic Resonance Imaging 1995;5:640-647.

46. Oyre S, Ringgaard S, Kozerke S, et al. Quantitation of circumferential subpixel vessel wall position and wall shear stress by multiple sectored three-dimensional paraboloid modeling of velocity encoded cine MR. Magn Reson Med 1998;40:645-655.

47. Long Q, Xu XY, Ariff B, Thom SA, Hughes AD, Stanton AV. Reconstruction of blood flow patterns in a human carotid bifurcation: a combined CFD and MRI study. Journal of Magnetic Resonance Imaging 2000;11:299-311.

48. Steinman DA, Thomas JB, Ladak HM, Milner JS, Rutt BK, Spence JD. Reconstruction of carotid bifurcation hemodynamics and wall thickness using computational fluid dynamics and MRI. Magn Reson Med 2002;47:149-159.

49. Papathanasopoulou P, Zhao S, Kohler U, et al. MRI measurement of time-resolved wall shear stress vectors in a carotid bifurcation model, and comparison with CFD predictions. Journal of Magnetic Resonance Imaging 2003;17:153-162.

50. Kohler U, Marshall I, Robertson MB, Long Q, Xu XY, Hoskins PR. MRI measurement of wall shear stress vectors in bifurcation models and comparison with CFD predictions. Journal of Magnetic Resonance Imaging 2001;14:563-573.

51. Reference Values for Arterial Stiffness C. Determinants of pulse wave velocity in healthy people and in the presence of cardiovascular risk factors: 'establishing normal and reference values'. Eur Heart J 2010;31:2338-2350.

52. Suever JD, Oshinski J, Rojas-Campos E, et al. Reproducibility of pulse wave velocity measurements with phase contrast magnetic resonance and applanation tonometry. Int J Cardiovasc Imaging 2012;28:1141-1146.

53. Lehmann ED, Parker JR, Hopkins KD, Taylor MG, Gosling RG. Validation and reproducibility of pressure-corrected aortic distensibility measurements using pulse-wave-velocity Doppler ultrasound. J Biomed Eng 1993;15:221-228.

54. Boese JM, Bock M, Schoenberg SO, Schad LR. Estimation of aortic compliance using magnetic resonance pulse wave velocity measurement. Physics in Medicine and Biology 2000;45:1703-1713.

55. Laffon E, Marthan R, Montaudon M, Latrabe V, Laurent F, Ducassou D. Feasibility of aortic pulse pressure and pressure wave velocity MRI measurement in young adults. Journal of Magnetic Resonance Imaging 2005;21:53-58.

56. Mohiaddin RH, Firmin DN, Longmore DB. Age-related changes of human aortic flow wave velocity measured noninvasively by magnetic resonance imaging. J Appl Physiol 1993;74:492-497.

57. Rogers WJ, Hu YL, Coast D, et al. Age-associated changes in regional aortic pulse wave velocity. J Am Coll Cardiol 2001;38:1123-1129.

58. Luo J, Li RX, Konofagou EE. Pulse wave imaging of the human carotid artery: an in vivo feasibility study. IEEE Trans Ultrason Ferroelectr Freq Control 2012;59:174-181.

59. Cheng C, Tempel D, van Haperen R, et al. Atherosclerotic lesion size and vulnerability are determined by patterns of fluid shear stress. Circulation 2006;113:2744-2753.

60. Frydrychowicz A, Stalder AF, Russe MF, et al. Three-dimensional analysis of segmental wall shear stress in the aorta by flow-sensitive four-dimensional-MRI. Journal of Magnetic Resonance Imaging 2009;30:77-84.

61. Ebbers T, Wigstrom L, Bolger AF, Wranne B, Karlsson M. Noninvasive measurement of time-varying three-dimensional relative pressure fields within the human heart. J Biomech Eng 2002;124:288-293.

62. Lum DP, Johnson KM, Paul RK, et al. Transstenotic pressure gradients: measurement in swine--retrospectively ECG-gated 3D phase-contrast MR angiography versus endovascular pressure-sensing guidewires. Radiology 2007;245:751-760.

63. Tyszka JM, Laidlaw DH, Asa JW, Silverman JM. Three-dimensional, time-resolved (4D) relative pressure mapping using magnetic resonance imaging. Journal of Magnetic Resonance Imaging 2000;12:321-329.

64. Yang GZ, Kilner PJ, Wood NB, Underwood SR, Firmin DN. Computation of flow pressure fields from magnetic resonance velocity mapping. Magn Reson Med 1996;36:520-526.

65. Dyverfeldt P, Gardhagen R, Sigfridsson A, Karlsson M, Ebbers T. On MRI turbulence quantification. Magn Reson Imaging 2009;27:913-922.

66. Dyverfeldt P, Sigfridsson A, Kvitting JP, Ebbers T. Quantification of intravoxel velocity standard deviation and turbulence intensity by generalizing phase-contrast MRI. Magn Reson Med 2006;56:850-858.

67. Dyverfeldt P, Kvitting JP, Sigfridsson A, Engvall J, Bolger AF, Ebbers T. Assessment of fluctuating velocities in disturbed cardiovascular blood flow: in vivo feasibility of generalized phase-contrast MRI. Journal of Magnetic Resonance Imaging 2008;28:655-663.

68. Sodickson DK, Manning WJ. Simultaneous acquisition of spatial harmonics (SMASH): fast imaging with radiofrequency coil arrays. Magn Reson Med 1997;38:591-603.

69. Pruessmann KP, Weiger M, Scheidegger MB, Boesiger P. SENSE: sensitivity encoding for fast MRI. Magn Reson Med 1999;42:952-962.

70. Griswold MA, Jakob PM, Heidemann RM, et al. Generalized autocalibrating partially parallel acquisitions (GRAPPA). Magn Reson Med 2002;47:1202-1210.

71. Griswold MA, Jakob PM, Nittka M, Goldfarb JW, Haase A. Partially parallel imaging with localized sensitivities (PILS). Magn Reson Med 2000;44:602-609.

72. Tsao J, Boesiger P, Pruessmann KP. k-t BLAST and k-t SENSE: dynamic MRI with high frame rate exploiting spatiotemporal correlations. Magn Reson Med 2003;50:1031-1042.

73. Kozerke S, Tsao J. Reduced data acquisition methods in cardiac imaging. Top Magn Reson Imaging 2004;15:161-168.

74. Mistretta CA, Wieben O, Velikina J, et al. Highly constrained backprojection for time-resolved MRI. Magn Reson Med 2006;55:30-40.

75. Johnson KM, Velikina J, Wu Y, Kecskemeti S, Wieben O, Mistretta CA. Improved waveform fidelity using local HYPR reconstruction (HYPR LR). Magn Reson Med 2008;59:456-462.

76. O'Halloran RL, Wen Z, Holmes JH, Fain SB. Iterative projection reconstruction of time-resolved images using highly-constrained back-projection (HYPR). Magn Reson Med 2008;59:132-139.

77. Ge L, Kino A, Griswold M, Mistretta C, Carr JC, Li D. Myocardial perfusion MRI with sliding-window conjugate-gradient HYPR. Magn Reson Med 2009;62:835-839.

78. Wang K, Busse RF, Holmes JH, et al. Interleaved variable density sampling with a constrained parallel imaging reconstruction for dynamic contrast-enhanced MR angiography. Magn Reson Med 2011;66:428-436.

79. Mc Kinnon GC, Bates RH. Towards imaging the beating heart usefully with a conventional CT scanner. IEEE Trans Biomed Eng 1981;28:123-127.

80. Firmin DN, Nayler GL, Kilner PJ, Longmore DB. The application of phase shifts in NMR for flow measurement. Magn Reson Med 1990;14:230-241.

81. Rebergen SA, van der Wall EE, Doornbos J, de Roos A. Magnetic resonance measurement of velocity and flow: technique, validation, and cardiovascular applications. Am Heart J 1993;126:1439-1456.

82. Schoenberg SO, Knopp MV, Bock M, et al. Renal artery stenosis: grading of hemodynamic changes with cine phase-contrast MR blood flow measurements. Radiology 1997;203:45-53.

83. Prince MR, Schoenberg SO, Ward JS, Londy FJ, Wakefield TW, Stanley JC. Hemodynamically significant atherosclerotic renal artery stenosis: MR angiographic features. Radiology 1997;205:128-136.

84. McKinnon GC. Interleaved echo planar phase contrast angiography. Magn Reson Med 1994;31:682-685.

85. Wang Y, Rossman PJ, Grimm RC, Riederer SJ, Ehman RL. Navigator-echo-based real-time respiratory gating and triggering for reduction of respiration effects in three-dimensional coronary MR angiography. Radiology 1996;198:55-60.

86. Barger AV, Peters DC, Block WF, et al. Phase-contrast with interleaved undersampled projections. Magn Reson Med 2000;43:503-509.

87. Peters DC, Korosec FR, Grist TM, et al. Undersampled projection reconstruction applied to MR angiography. Magn Reson Med 2000;43:91-101.

88. Vigen KK, Peters DC, Grist TM, Block WF, Mistretta CA. Undersampled projection-reconstruction imaging for time-resolved contrast-enhanced imaging. Magn Reson Med 2000;43:170-176.

89. Bernstein MA, Grgic M, Brosnan TJ, Pelc NJ. Reconstructions of phase contrast, phased array multicoil data. Magn Reson Med 1994;32:330-334.

90. Bland JM, Altman DG. Statistical methods for assessing agreement between two methods of clinical measurement. Lancet 1986;1:307-310.

91. Pruessmann KP, Weiger M, Bornert P, Boesiger P. Advances in sensitivity encoding with arbitrary k-space trajectories. Magn Reson Med 2001;46:638-651.

92. Bock M, Schad LR, Muller E, Lorenz WJ. Pulsewave velocity measurement using a new real-time MR-method. Magn Reson Imaging 1995;13:21-29.

93. Laurent S, Katsahian S, Fassot C, et al. Aortic stiffness is an independent predictor of fatal stroke in essential hypertension. Stroke 2003;34:1203-1206.

94. Salvi P, Magnani E, Valbusa F, et al. Comparative study of methodologies for pulse wave velocity estimation. J Hum Hypertens 2008;22:669-677.

95. Grotenhuis HB, Westenberg JM, Steendijk P, et al. Validation and Reproducibility of Aortic Pulse Wave Velocity as Assessed With Velocity-Encoded MRI. Journal of Magnetic Resonance Imaging 2009;30:521-526.

96. Stevanov M, Baruthio J, Gounot D, Grucker D. In vitro validation of MR measurements of arterial pulse-wave velocity in the presence of reflected waves. Journal of Magnetic Resonance Imaging 2001;14:120-127.

97. Bolster BD, Jr., Atalar E, Hardy CJ, McVeigh ER. Accuracy of arterial pulse-wave velocity measurement using MR. Journal of Magnetic Resonance Imaging 1998;8:878-888.

98. Markl M, Wallis W, Brendecke S, Simon J, Frydrychowicz A, Harloff A. Estimation of global aortic pulse wave velocity by flow-sensitive 4D MRI. Magn Reson Med 2010;63:1575-1582.

99. Hardy CJ, Bolster BD, Jr., McVeigh ER, Iben IE, Zerhouni EA. Pencil excitation with interleaved fourier velocity encoding: NMR measurement of aortic distensibility. Magn Reson Med 1996;35:814-819.

100. Taviani V, Hickson SS, Hardy CJ, et al. Age-related changes of regional pulse wave velocity in the descending aorta using Fourier velocity encoded M-mode. Magn Reson Med 2011;65:261-268.

101. Mochida M, Sakamoto H, Sawada Y, et al. Visceral fat obesity contributes to the tortuosity of the thoracic aorta on chest radiograph in poststroke Japanese patients. Angiology 2006;57:85-91.

102. Gu T, Korosec FR, Block WF, et al. PC VIPR: a high-speed 3D phase-contrast method for flow quantification and high-resolution angiography. AJNR Am J Neuroradiol 2005;26:743-749.

103. Markl M, Chan FP, Alley MT, et al. Time-resolved three-dimensional phase-contrast MRI. Journal of Magnetic Resonance Imaging 2003;17:499-506.

104. Fielden SW, Fornwalt BK, Jerosch-Herold M, Eisner RL, Stillman AE, Oshinski JN. A new method for the determination of aortic pulse wave velocity using cross-correlation on 2D PCMR velocity data. Journal of Magnetic Resonance Imaging 2008;27:1382-1387.

105. Taviani V, Patterson AJ, Graves MJ, et al. Accuracy and repeatability of fourier velocity encoded M-mode and two-dimensional cine phase contrast for pulse wave velocity measurement in the descending aorta. Journal of Magnetic Resonance Imaging 2010;31:1185-1194.

106. Johnson KM, Lum DP, Turski PA, Block WF, Mistretta CA, Wieben O. Improved 3D phase contrast MRI with off-resonance corrected dual echo VIPR. Magn Reson Med 2008;60:1329-1336.

107. Du J, Lu A, Block WF, Thornton FJ, Grist TM, Mistretta CA. Time-resolved undersampled projection reconstruction magnetic resonance imaging of the peripheral vessels using multi-echo acquisition. Magn Reson Med 2005;53:730-734.

108. Liu J, Redmond MJ, Brodsky EK, et al. Generation and visualization of four-dimensional MR angiography data using an undersampled 3-D projection trajectory. IEEE Trans Med Imaging 2006;25:148-157.

109. Bock J, Frydrychowicz A, Stalder AF, et al. 4D phase contrast MRI at 3 T: effect of standard and blood-pool contrast agents on SNR, PC-MRA, and blood flow visualization. Magn Reson Med 2010;63:330-338.

110. Busse R, Fleming I. Pulsatile stretch and shear stress: physical stimuli determining the production of endothelium-derived relaxing factors. J Vasc Res 1998;35:73-84.

111. Koller A, Huang A. Development of nitric oxide and prostaglandin mediation of shear stress-induced arteriolar dilation with aging and hypertension. Hypertension 1999;34:1073-1079.

112. Pohl U, Holtz J, Busse R, Bassenge E. Crucial role of endothelium in the vasodilator response to increased flow in vivo. Hypertension 1986;8:37-44.

113. Davies PF, Tripathi SC. Mechanical stress mechanisms and the cell. An endothelial paradigm. Circ Res 1993;72:239-245.

114. Meng H, Wang Z, Hoi Y, et al. Complex hemodynamics at the apex of an arterial bifurcation induces vascular remodeling resembling cerebral aneurysm initiation. Stroke 2007;38:1924-1931.

115. Boussel L, Rayz V, McCulloch C, et al. Aneurysm growth occurs at region of low wall shear stress: patient-specific correlation of hemodynamics and growth in a longitudinal study. Stroke 2008;39:2997-3002.

116. Friedman MH, Deters OJ, Bargeron CB, Hutchins GM, Mark FF. Shear-dependent thickening of the human arterial intima. Atherosclerosis 1986;60:161-171.

117. Ku DN, Giddens DP, Phillips DJ, Strandness DE, Jr. Hemodynamics of the normal human carotid bifurcation: in vitro and in vivo studies. Ultrasound Med Biol 1985;11:13-26.

118. Pedersen EM, Oyre S, Agerbaek M, et al. Distribution of early atherosclerotic lesions in the human abdominal aorta correlates with wall shear stresses measured in vivo. Eur J Vasc Endovasc Surg 1999;18:328-333.

119. Brands PJ, Hoeks AP, Hofstra L, Reneman RS. A noninvasive method to estimate wall shear rate using ultrasound. Ultrasound Med Biol 1995;21:171-185.

120. Wells DR, Archie JP, Jr., Kleinstreuer C. Effect of carotid artery geometry on the magnitude and distribution of wall shear stress gradients. J Vasc Surg 1996;23:667-678.

121. Oyre S, Pedersen EM, Ringgaard S, Boesiger P, Paaske WP. In vivo wall shear stress measured by magnetic resonance velocity mapping in the normal human abdominal aorta. Eur J Vasc Endovasc Surg 1997;13:263-271.

122. Bogren HG, Buonocore MH. Blood flow measurements in the aorta and major arteries with MR velocity mapping. Journal of Magnetic Resonance Imaging 1994;4:119-130.

123. Bogren HG, Mohiaddin RH, Yang GZ, Kilner PJ, Firmin DN. Magnetic resonance velocity vector mapping of blood flow in thoracic aortic aneurysms and grafts. J Thorac Cardiovasc Surg 1995;110:704-714.

124. Kilner PJ, Yang GZ, Mohiaddin RH, Firmin DN, Longmore DB. Helical and retrograde secondary flow patterns in the aortic arch studied by three-directional magnetic resonance velocity mapping. Circulation 1993;88:2235-2247.

125. Mohiaddin RH, Kilner PJ, Rees S, Longmore DB. Magnetic resonance volume flow and jet velocity mapping in aortic coarctation. J Am Coll Cardiol 1993;22:1515-1521.

126. Bogren HG, Buonocore MH. 4D magnetic resonance velocity mapping of blood flow patterns in the aorta in young vs. elderly normal subjects. Journal of Magnetic Resonance Imaging 1999;10:861-869.

127. Bogren HG, Mohiaddin RH, Kilner PJ, Jimenez-Borreguero LJ, Yang GZ, Firmin DN. Blood flow patterns in the thoracic aorta studied with three-directional MR velocity mapping: the effects of age and coronary artery disease. Journal of Magnetic Resonance Imaging 1997;7:784-793.

128. Frydrychowicz A, Harloff A, Jung B, et al. Time-resolved, 3-dimensional magnetic resonance flow analysis at 3 T: visualization of normal and pathological aortic vascular hemodynamics. J Comput Assist Tomogr 2007;31:9-15.

129. Markl M, Draney MT, Hope MD, et al. Time-resolved 3-dimensional velocity mapping in the thoracic aorta: visualization of 3-directional blood flow patterns in healthy volunteers and patients. J Comput Assist Tomogr 2004;28:459-468.

130. Markl M, Draney MT, Miller DC, et al. Time-resolved three-dimensional magnetic resonance velocity mapping of aortic flow in healthy volunteers and patients after valve-sparing aortic root replacement. J Thorac Cardiovasc Surg 2005;130:456-463.

131. Zhu H, Zhang J, Shih J, et al. Differences in aortic arch geometry, hemodynamics, and plaque patterns between C57BL/6 and 129/SvEv mice. J Biomech Eng 2009;131:121005.

132. Hope TA, Markl M, Wigstrom L, Alley MT, Miller DC, Herfkens RJ. Comparison of flow patterns in ascending aortic aneurysms and volunteers using four-dimensional magnetic resonance velocity mapping. Journal of Magnetic Resonance Imaging 2007;26:1471-1479.

133. Bieging ET, Frydrychowicz A, Wentland A, et al. In vivo three-dimensional MR wall shear stress estimation in ascending aortic dilatation. Journal of Magnetic Resonance Imaging 2011;33:589-597.

134. Bogaert J, Gewillig M, Rademakers F, et al. Transverse arch hypoplasia predisposes to aneurysm formation at the repair site after patch angioplasty for coarctation of the aorta. J Am Coll Cardiol 1995;26:521-527.

135. Morbiducci U, Ponzini R, Rizzo G, et al. In vivo quantification of helical blood flow in human aorta by time-resolved three-dimensional cine phase contrast magnetic resonance imaging. Ann Biomed Eng 2009;37:516-531.

136. Williams S, Petersen M, Bremer PT, et al. Adaptive extraction and quantification of geophysical vortices. IEEE Trans Vis Comput Graph 2011;17:2088-2095.

137. Arad Y, Goodman KJ, Roth M, Newstein D, Guerci AD. Coronary calcification, coronary disease risk factors, C-reactive protein, and atherosclerotic cardiovascular disease events: the St. Francis Heart Study. J Am Coll Cardiol 2005;46:158-165.

138. Vita JA, Treasure CB, Ganz P, Cox DA, Fish RD, Selwyn AP. Control of shear stress in the epicardial coronary arteries of humans: impairment by atherosclerosis. J Am Coll Cardiol 1989;14:1193-1199.

139. Wentzel JJ, Corti R, Fayad ZA, et al. Does shear stress modulate both plaque progression and regression in the thoracic aorta? Human study using serial magnetic resonance imaging. J Am Coll Cardiol 2005;45:846-854.

140. Markl M, Kilner PJ, Ebbers T. Comprehensive 4D velocity mapping of the heart and great vessels by cardiovascular magnetic resonance. J Cardiovasc Magn Reson 2011;13:7.

141. Nett EJ, Johnson KM, Frydrychowicz A, et al. Four-dimensional phase contrast MRI with accelerated dual velocity encoding. Journal of Magnetic Resonance Imaging 2012;35:1462-1471.

142. Carlsson M, Toger J, Kanski M, et al. Quantification and visualization of cardiovascular 4D velocity mapping accelerated with parallel imaging or k-t BLAST: head to head comparison and validation at 1.5 T and 3 T. J Cardiovasc Magn Reson 2011;13:55.

143. Eriksson J, Carlhall CJ, Dyverfeldt P, Engvall J, Bolger AF, Ebbers T. Semi-automatic quantification of 4D left ventricular blood flow. J Cardiovasc Magn Reson 2010;12:9.

144. Uribe S, Beerbaum P, Sorensen TS, Rasmusson A, Razavi R, Schaeffter T. Four-dimensional (4D) flow of the whole heart and great vessels using real-time respiratory self-gating. Magn Reson Med 2009;62:984-992.

145. Hollnagel DI, Summers PE, Kollias SS, Poulikakos D. Laser Doppler velocimetry (LDV) and 3D phase-contrast magnetic resonance angiography (PC-MRA) velocity measurements: validation in an anatomically accurate cerebral artery aneurysm model with steady flow. Journal of Magnetic Resonance Imaging 2007;26:1493-1505.

146. Chang W, Landgraf B, Johnson KM, et al. Velocity measurements in the middle cerebral arteries of healthy volunteers using 3D radial phase-contrast HYPRFlow: comparison with transcranial Doppler sonography and 2D phase-contrast MR imaging. AJNR Am J Neuroradiol 2011;32:54-59.

147. Bley TA, Johnson KM, Francois CJ, et al. Noninvasive assessment of transstenotic pressure gradients in porcine renal artery stenoses by using vastly undersampled phase-contrast MR angiography. Radiology 2011;261:266-273.

148. Francois CJ, Lum DP, Johnson KM, et al. Renal arteries: isotropic, high-spatial-resolution, unenhanced MR angiography with three-dimensional radial phase contrast. Radiology 2011;258:254-260.

149. Markl M, Harloff A, Bley TA, et al. Time-resolved 3D MR velocity mapping at 3T: improved navigator-gated assessment of vascular anatomy and blood flow. Journal of Magnetic Resonance Imaging 2007;25:824-831.

150. Bax L, Bakker CJ, Klein WM, Blanken N, Beutler JJ, Mali WP. Renal blood flow measurements with use of phase-contrast magnetic resonance imaging: normal values and reproducibility. J Vasc Interv Radiol 2005;16:807-814.

151. Stalder AF, Russe MF, Frydrychowicz A, Bock J, Hennig J, Markl M. Quantitative 2D and 3D phase contrast MRI: optimized analysis of blood flow and vessel wall parameters. Magn Reson Med 2008;60:1218-1231.

152. Rodondi N, Auer R, Devine PJ, O'Malley PG, Hayoz D, Cornuz J. The impact of carotid plaque screening on motivation for smoking cessation. Nicotine Tob Res 2008;10:541-546.

153. Wong ND, Detrano RC, Diamond G, et al. Does coronary artery screening by electron beam computed tomography motivate potentially beneficial lifestyle behaviors? Am J Cardiol 1996;78:1220-1223.

154. Harloff A, Nussbaumer A, Bauer S, et al. In vivo assessment of wall shear stress in the atherosclerotic aorta using flow-sensitive 4D MRI. Magn Reson Med 2010;63:1529-1536.

155. Louis CF, Gallant EM, Remple E, Mickelson JR. Malignant hyperthermia and porcine stress syndrome: a tale of two species. Pig News and Information 1990;11:341-344.

156. Lerman J, Oyston JP, Gallagher TM, Miyasaka K, Volgyesi GA, Burrows FA. The minimum alveolar concentration (MAC) and hemodynamic effects of halothane, isoflurane, and sevoflurane in newborn swine. Anesthesiology 1990;73:717-721.

157. Wentland AL, Artz NS, Fain SB, Grist TM, Djamali A, Sadowski EA. MR measures of renal perfusion, oxygen bioavailability and total renal blood flow in a porcine model: noninvasive regional assessment of renal function. Nephrol Dial Transplant 2012;27:128-135.

158. Ahmed AS, Zellerhoff M, Strother CM, et al. C-arm CT measurement of cerebral blood volume: an experimental study in canines. AJNR Am J Neuroradiol 2009;30:917-922.

159. Bley T, Strother CM, Pulfer K, et al. C-arm CT measurement of cerebral blood volume in ischemic stroke: an experimental study in canines. AJNR Am J Neuroradiol 2010;31:536-540.

160. McCormick M, Varghese T, Wang X, Mitchell C, Kliewer MA, Dempsey RJ. Methods for robust in vivo strain estimation in the carotid artery. Physics in Medicine and Biology 2012;57:7329-7353.

161. Kallel F, Ophir J. A least-squares strain estimator for elastography. Ultrason Imaging 1997;19:195-208.

162. Kao TW, Taylor HF. High-sensitivity intrinsic fiber-optic Fabry-Perot pressure sensor. Opt Lett 1996;21:615-617.

163. Wentland AL, Korosec FR, Vigen KK, Wieben O, Fine JP, Grist TM. Cine flow measurements using phase contrast with undersampled projections: in vitro validation and preliminary results in vivo. Journal of Magnetic Resonance Imaging 2006;24:945-951.

164. Baltes C, Kozerke S, Hansen MS, Pruessmann KP, Tsao J, Boesiger P. Accelerating cine phase-contrast flow measurements using k-t BLAST and k-t SENSE. Magn Reson Med 2005;54:1430-1438.

165. Stadlbauer A, van der Riet W, Globits S, Crelier G, Salomonowitz E. Accelerated phase-contrast MR imaging: comparison of k-t BLAST with SENSE and Doppler ultrasound for velocity and flow measurements in the aorta. Journal of Magnetic Resonance Imaging 2009;29:817-824.

166. Marshall I. Feasibility of k-t BLAST technique for measuring "seven-dimensional" fluid flow. Journal of Magnetic Resonance Imaging 2006;23:189-196.

167. Stadlbauer A, van der Riet W, Crelier G, Salomonowitz E. Accelerated time-resolved three-dimensional MR velocity mapping of blood flow patterns in the aorta using SENSE and k-t BLAST. Eur J Radiol 2010;75:e15-21.

168. Westenberg JJ, Roes SD, Ajmone Marsan N, et al. Mitral valve and tricuspid valve blood flow: accurate quantification with 3D velocity-encoded MR imaging with retrospective valve tracking. Radiology 2008;249:792-800.

169. Breuer FA, Kellman P, Griswold MA, Jakob PM. Dynamic autocalibrated parallel imaging using temporal GRAPPA (TGRAPPA). Magn Reson Med 2005;53:981-985.

170. Jung B, Ullmann P, Honal M, Bauer S, Hennig J, Markl M. Parallel MRI with extended and averaged GRAPPA kernels (PEAK-GRAPPA): optimized spatiotemporal dynamic imaging. Journal of Magnetic Resonance Imaging 2008;28:1226-1232.

171. Peng HH, Bauer S, Huang TY, et al. Optimized parallel imaging for dynamic PC-MRI with multidirectional velocity encoding. Magn Reson Med 2010;64:472-480.

172. Thunberg P, Karlsson M, Wigstrom L. Accuracy and reproducibility in phase contrast imaging using SENSE. Magn Reson Med 2003;50:1061-1068.

173. Kwak Y, Nam S, Akcakaya M, et al. Accelerated aortic flow assessment with compressed sensing with and without use of the sparsity of the complex difference image. Magn Reson Med 2012;

174. Hsiao A, Lustig M, Alley MT, Murphy MJ, Vasanawala SS. Evaluation of Valvular Insufficiency and Shunts with Parallel-imaging Compressed-sensing 4D Phase-contrast MR Imaging with Stereoscopic 3D Velocity-fusion Volume-rendered Visualization. Radiology 2012;265:87-95.